ABSTRACT

JU, BYONGSUN. Properties of Zr Silicate and Zr-Si Oxynitride High-k Dielectric Alloys for Advanced Microelectronic Applications; *Chemical and Electrical Characterizations* (Under the direction of Professor Gerald Lucovsky)

As the microelectronic devices are aggressively scaled down to the 1999 International Technology Roadmap, the advanced complementary metal oxide semiconductor (CMOS) is required to increase packing density of ultra-large scale integrated circuits (ULSI). However, SiO_2 or Si oxynitride (SiO_xN_y) films which is a traditional gate oxide materials shows its limitations in direct tunneling current density at the below about 3nm thickness, and moreover, the priority of leakage current is ranked high in device performance and reliability as the portable device prevails. High-k alternative dielectrics can provide the required levels of EOT for device scaling at larger physical thickness, thereby providing a materials pathway for reducing the tunneling current.

Zr silicates and its end members (SiO_2 and ZrO_2) and Zr-Si oxynitride films, $(ZrO_2)_x(Si_3N_4)_y(SiO_2)_z$, have been deposited using a remote plasma-enhanced chemical vapor deposition (RPECVD) system. After deposition of Zr silicate, the films were exposed to He/N_2 plasma to incorporate nitrogen atoms into the surface of films. The amount of incorporated nitrogen atoms was measured by on-line Auger electron spectrometry (AES) as a function of silicate composition and showed its local minimum around the 30% silicate. Characterization by AES and x-ray photoelectron spectroscopy

(XPS) indicated that the nitrogen atoms were substituted for the oxygen atoms' position and made a bond with Si and Zr depending on the silicate composition. The effect of nitrogen atoms on capacitance-voltage (C-V) and leakage-voltage (J-V) were also investigated by fabricating metal-oxide-semiconductor (MOS) capacitors. Results suggested that incorporating nitrogen into silicate decreased the leakage current in SiO_2-rich silicate, whereas the leakage increased in the middle range of silicate.

The pseudo-ternary alloy composition was determined by Rutherford back scattering (RBS) that was calibrated by on-line Auger electron spectroscopy (AES) and showed the composition's thermodynamically stable boundary composition in ternary phase diagrams. Zr-Si oxynitride was a pseudo-ternary alloy and no phase separation was detected by x-ray photoelectron spectroscopy (XPS) analysis up to 1100°C annealing. The leakage current of Zr-Si oxynitride films showed two different temperature dependent activation energies, 0.02 eV for low temperature and 0.3 eV for high temperature. Poole-Frenkel emission was the dominant leakage mechanism.

Zr silicate alloys with no Si_3N_4 phase were chemically separated into the SiO_2 and ZrO_2 phase as annealed above 900°C. While chemical phase separation in Zr silicate films with Si_3N_4 phase (Zr-Si oxynitride) were suppressed as increasing the amount of Si_3N_4 phase due to the narrow bonding network in Si_3N_4 phase. (3.4 bonds/atom for Si_3N_4 network, 2.67 bonds/atom for SiO_2 network)

Properties of Zr Silicate and Zr-Si Oxynitride High-k Dielectric Alloys for Advanced Microelectronic Applications; *Chemical and Electrical Characterizations*

by

BYONGSUN JU

A dissertation submitted to the Graduate Faculty of
North Carolina State University
in partial fulfillment of the
requirements for the Degree of
Doctor of Philosophy

MATERIALS SCIENCE AND ENGINEERING

Raleigh

2005

APPROVED BY:

Dr. Gerald Lucovsky	**Dr. Jon-Paul Maria**
Chair of Advisory Committee	
Dr. Robert Nemanich	**Dr. Carl Osburn**

BIOGRAPHY

Byongsun Ju was born in Daejeon, Korea on January 24, 1969. After graduation from Yousung high school in Daejeon, he entered Yonsei University at Seoul in 1987. He got his bachelor and master degree in Metallurgy and Materials Science in 1994 and 1996, respectively. During his M.S degree, he participated in the fabrication of square polycrystalline Si solar cell in columnar grain using unidirectional solidification. Thereafter, he worked for Samsung Electronics Co., joined the Process Development Team focusing on the plasma etching process for the next generation of BST/Pt capacitor and Tungsten silicide (or/and Tungsten) gate in Giga-grade DRAMs. During that time, he got married to his beautiful wife, Hyunju Noh. He enrolled in the Ph.D program at North Carolina State University in Raleigh, North Carolina in 2001 and began his graduate research work under the direction of Professor Gerald Lucovsky. His daughter, Kayla Jihyun Ju, was born during the course of his research in the Zr silicate and Zr-Si oxynitride stacked layer as gate dielectrics for advanced CMOS technology. He completed the requirements for the Ph.D degree in Materials Science Engineering in the Summer of 2005.

ACKNOWLEDGEMENTS

I would like to extend appreciation for the guidance and encouragement of my advisor, Professor Gerald Lucovsky, throughout this work. I also thank Dr. Carlton Osburn, Dr. Jon-Paul Maria and Dr. Robert Nemanich for their helpful comments and serving on my advisory committee.

I gratefully acknowledge the administrative and support staff of the Microelectronics Laboratory in North Carolina State University; in particular Joan O'Sullivan, Harold Morton, Dr. Ginger Yu and Myrick Peacock. I also acknowledge the colleagues in Dr. Lucovsky group, Bruce Rayner, Yi-mu Lee, Chris Hinkle, Cheol-hwyi Bae, Sangjeong Oh, Sanghyun Lee and Dr. Christiano Krug for their help and friendship. Thanks to E.E. Deas in the Department of Materials Science and Engineering for her kindness and help.

Finally I want to express to my sincere gratitude to my wife, Hyunju Noh, and my daughter, Kayla Jihyun Ju, for their patience and encouragement in the life in Raleigh for my Ph.D program.

TABLE OF CONTENTS

LIST OF FIGURES

LIST OF TABLES

CHAPTER 1. INTRODUCTION

1.1 The Need for High-k Materials

As the microelectronic devices are aggressively scaled down to the 1999 International Technology Roadmap [1], the advanced complementary metal oxide semiconductor (CMOS) is required to increase packing density of ultra-large scale integrated circuits (ULSI). It is essential to have a thinner dielectric as well as smaller channel length and width to maintain the same drive currents needed for circuit operation [2~5]. However, SiO_2 or nitrided SiO_2 films which are the traditional gate oxide materials show no significant limitations in direct tunneling current density below about 1.5nm thickness for high performance/high power devices, and about 2-2.5 nm thickness for mobile device applications [6~8]. Intensive research has focused on high dielectric constant materials as an alternative replacement for SiO_2 in order to extend the equivalent oxide thickness (EOT) below the limits cited above; e.g. to 0.5 nm for high power devices, and 1.0 nm for mobile devices. High-k alternative dielectrics can provide the required levels of EOT for device scaling at larger physical thickness, thereby providing a materials pathway for reducing the tunneling current. The requirements [9~12] for these materials are very severe. They must have a high thermodynamic stability with the silicon substrate. Their diffusion coefficients should be low so that they can withstand high processing temperatures. For gate oxides, they should form high quality interfaces with silicon with few interfacial defects and low roughness. They must have conduction and

valence band offset energies, respectively, for electrons and holes of at lease 1eV, in order to have sufficient low leakage current.

There are several candidates for high-k dielectric materials such as transition metal/rare earth (TM/RE) oxides (ZrO_2, HfO_2, Y_2O_3, La_2O_3), TM/RE silicates [$(ZrO_2)(SiO_2)$], [$(HfO_2)(SiO_2)$] and TM/RE aluminates [$(ZrO_2)(Al_2O_3)$, $(La_2O_3)(Al_2O_3)$] [13~15]. Recently, HfO_2 [16,17], ZrO_2 [13,14,15], and their silicates were identified as attractive candidates since their dielectric constants are sufficiently high to effectively reduce the leakage current. They are also known for being thermodynamically stable in contact with Si. Although TM/RE silicate films have smaller dielectric constants than metal oxides, silicate films are thermally more stable on the Si substrate. In particular, it has been reported that because of the pinning of d state the TM conduction band edge, silicate films have wider band gaps as shown in Figure 1.1 and less leakage current with the same EOT than that of TM/RE oxides films [18,19]. The band gaps for the Zr silicate alloys increase monotonically between its respective elemental oxide, ZrO_2, but the conduction band offset energies with respect to are associated with the transition metal d* state and effectively pinned at the end member oxide values.

However, it was reported [20] that phase separation and crystallization often occurred when Hf and Zr silicates were annealed above 900°C. These problems caused not only the leakage current increase through the grain boundary and roughness of the film surface, but further deterioration of the high-k character. These films crystallize readily, can be difficult to etch [21], can react with the Si top electrode [22,23], and have been shown recently to be susceptible to dopant penetration [24].

1.2 The Need for Nitridation

One of the other important problems that have to be considered when using poly Si gate electrode is dopant penetration. The boron doped p^+ poly Si gate electrode for the PMOS device improves the short channel effects; however, boron diffusion from the poly Si gate electrode into the channel region through the gate dielectrics can degrade PMOS device performance [25~27]. For example, boron diffusion into the channel region results in a large positive flat band voltage shift, increases the sub-threshold slope and electron trapping and decreases low field mobility. In addition, it degrades process control by introducing a spread of threshold voltages. Therefore, for boron doped p^+ poly Si gate electrode applications, it is necessary to have a diffusion barrier in the gate oxide to prevent the boron penetration into the Si substrate and the channel region [28,29].

Nitrogen atoms incorporated into the gate dielectric structure are one of candidates for blocking boron diffusion. Aoyama observed that the diffusion of boron decreased as the nitrogen content in bulk oxynitride gate dielectric films increased [30]. Ellis proposed that the boron atoms diffused substitutionally for Si atoms and that the presence of a Si-N bond impeded substitution for the Si atom. In this model the boron atoms hop from one Si site to another Si site. The presence of a Si-N bond blocked the boron atom hopping process [31]. Fair [32,33] predicted that less than 10 at.% of nitrogen in the oxide has a negligible effect on boron diffusion. Therefore, to prevent the boron diffusion from the p^+ poly Si gate electrode to the Si substrate needs a higher concentration of nitrogen; e.g., at least 15~20 at.% nitrogen is necessary in the bulk of the film, and a lesser amount at the Si/SiO_2 interface. However, light interfacial nitridation

optimizes device performance and reliability. To prevent the boron at the Si/SiO_2 interface, one needs a distribution of nitridation that is different in the bulk and at the interface.

Stated differently, even if boron diffusion into the channel is prevented by heavy nitridation at the Si/SiO_2 interface, boron can accumulate in the bulk oxide, and this accumulated boron in the oxide causes reliability degradation under gate injection. For examples, a low boron doping level in the poly Si gate electrode and a low temperature post implantation activation/drive-in anneal help to prevent severe boron penetration into the Si substrate. However, this is not optimum for device performance and reliability. From the carrier mobility point of view, it is desirable to have a high N concentration near the poly-Si/dielectric interface [34]. In addition, a low activated doping concentration at the poly Si/gate dielectrics results in poly Si depletion effects, causing poor device performance [35,36]

It has recently been shown that the addition of N into the Hf-silicate also inhibits crystallization [37]. It has also been demonstrated that such films exhibit reduced flat band voltage shifts after activation anneals as compared to SiO_2 or SiO_xN_y films of comparable thickness and resultant in long-channel mobility which exceed those of the other high-k gate dielectric candidates [38]. The incorporation of N is also useful in preventing interfacial reaction, improving thermal stability, as well as minimizing dopant diffusion and improving Si surface quality. It is therefore important to suppress boron penetration at the top surface of the oxide since a boron-blocking barrier on top of the oxide will prevent boron diffusion into the bulk oxide and to the Si/SiO_2 interface. The heavy nitridation layer must be kept far from the Si/SiO_2 interface. A heavy nitridation

layer on the top surface of the oxide is not expected to reduce the device performance and reliability [31]. Eventually incorporation nitrogen into top surface of dielectric films is supposed to be the most effective way to screen boron from poly electrode. The advantages [39,40] of using N_2 as a nitrogen source over other gas such as, NH_3 or N_2O, are following. (1) It is a hydrogen-free nitrogen source, so minimizes hydrogen incorporation in the oxynitride films. (2) Nitrogen gas is relatively inexpensive and available in very high purity grades. (3) No possibilities of physical thickness increases due to the formation of SiO_2 layer by oxygen source in N_2O. (4) It can easily be pumped out of the system unlike NH_3 that is plagued with condensation problems that lead to memory effects and subsequent process contamination.

Many processing techniques, such as plasma processing [41,42,43,44], low-pressure chemical vapor deposition [45,46], jet vapor deposition [47], low energy ion implantation [48], and atomic layer deposition [49], have been developed to form ultrathin Si oxynitride films at low temperatures. Boron diffusion in HfO_2 has also been observed. Nitridation of the top layer of HfO_2 can effectively block boron diffusion and bulk N can help prevent phase separation in Hf and Zr silicates [37,50]. N incorporation into high-k metal oxide may also provide a way to control the flat band shifts by modifying the defect structures in the bulk and/or at the interface. In SiO_2, nitrogen at the dielectric/poly-Si gate interface and a small amount of nitrogen (less than 1at.%) close to the substrate/SiO_2 interface is commonly used to block dopant penetration and improve the reliability. The N concentration distribution in high-k dielectrics will also likely be important to achieve optimal electrical performance [51]. Because thermodynamics of the Si-O-N system and the kinetics of nitrogen incorporation are rather complex, the different

methods of SiON preparation will produce SiON films with different N spatial distributions [52~54] and with different electrical properties, especially in the case of plasma nitridation where active nitrogen species are introduced into the oxide. But our previous results [55] revealed that the incorporated nitrogen atoms break the oxygen atom bonding, and/or be substituted for the oxygen atoms and make a bond with Zr atoms as well as Si atoms in the middle range silicates. Zirconium nitride is known as metallic conductor that acts as a leakage source in the middle range of silicate alloy compositions.

1.3 Outline of the Dissertation

This dissertation will demonstrate physical and electrical properties and qualitative understanding of Zr base high-k dielectric films for advanced microelectronic devices. As previously mentioned, the research issues for high-k dielectrics addressed by this research are thermal stability of internal structure and valence band offset energies with Si. Subsequent heat treatments can provides sufficient thermal energy for changes in internal structure, such as chemical phase separation and crystallization, to occur within the dielectric.

Chapter 2 describes a RPECVD chamber for deposition of Zr silicate and Zr-Si oxynitride films and provides a description of all the source materials and the experimental techniques used in the fabrication and evaluations of the materials

Chapter 3 discussed the effects of nitridation on Zr silicate alloys and its end members (SiO_2 and ZrO_2). This is achieved by in-situ plasma nitridation. The concentration of incorporated nitrogen is monitored by on-line Auger electron

spectroscopy (AES). Chemical bonding was studied using x-ray photoelectron spectroscopy (XPS) before and after annealing. Based on the spectroscopy results, the effects of the incorporated nitrogen atoms on the electrical properties of gate dielectric films the silicate compositions were also investigated.

Chapter 4 details Zr-Si oxynitride films, deposited by integration of Zr source gas into N_2/N_2O and silane gas mixture. The concentration of incorporated nitrogen was measured by on-line Auger electron spectroscopy (AES) and chemical bonding was also studied using x-ray photoelectron spectroscopy (XPS) before and after annealing. Based on the spectroscopy results, the effects of the phase separation in dielectric films on the electrical properties of Zr-Si oxynitride gate dielectrics were investigated by C-V and I-V analysis.

Chapter 5 describes Zr-Si oxynitride films that were deposited with significantly increased amounts of Si_3N4. The chemical bonding and the effects of the nitrogen atoms on the chemical phase separation in Zr-Si oxynitride films were studied using Fourier transform infrared (FTIR) spectroscopy and x-ray photoelectron spectroscopy (XPS).

In chapter 6 is a summary that highlights the main accomplishments of this research, and indicates future directions for research in this area.

1.4 REFERENCES

[1] Semiconductor Industry Association, International Technology Roadmap for Semiconductor: 2003 Edition. (http://public.itrs.net)

[2] T.Hori and H.Iwasaki, IEEE Electron Device Lett. **EDL-10**, 195 (1989)

[3] H.Hwang, W.Ting, D.-L. Kwong, and J.Lee, IEEE Electron Device Lett. **EDL-12**, 495 (1991)

[4] Y.Okada, P.J.Tobin, K.G.Reid, R.I.Hegde, B.Maiti, and S.A.Ajuria, Symp. VLSI Tech. Dig. Tech. Papers 105 (1994)

[5] M.Bhat, D.Wristers, J.Yan, L.K.Han, J. Fulford, and D.-L. Kwong, Tech. Dig. Int. Electron Devices Meet. **329** (1994)

[6] D.A. Buchanan, E.P. Gusev, E. Cartier, H. Okorn-Schmidt, K. Rim, M.A. Gribelyuk, A. Mocuta, A. Ajmera, M. Copel, S. Guha, N. Bojarczuk, A. Callegari, C. D Emic, P. Kozlowski, K. Chen, R.J. Fleming, P.C. Jamison, J. Browin, and R. Ardnt, Tech. Dig. Int. Electron Device Meet., p.223 (2000)

[7] D. Park, Y-C. King, Q. Lu, T-J. King, C. Hu, A. Kalnitsky, S-P. Tay, and C-C. Cheng, IEEE Electron Device Letters, **19**, 11, 441 (1998)

[8] Y.Wu, G.Lucovsky and H.Z.Massoud, Proc. IEEE International Reliability Physics Symp., 70 (1998)

[9] P.Zurcher et al., Mater. Res. Soc. Symp. Proc. **541**, 11 (1999)

[10] A.Gril et al. Mater. Res. Soc. Symp. Proc. **541**, 89 (1999)

[11] H.J.Hubbard and D.G.Schlom, J. Mater. Res. **11**, 2757 (1996)

[12] J.Robertson et al, J. Vac. Sci. Technol. B **18**, (2000)

[13] A.S.Kao, J.Appl. Phys. **69**, 3309 (1991)

[14] W.J.Qi, R.Nieh, B.H.Lee, L.Kang, Y.Jeon, K.Onish, T.Ngai, S.Banerjee, and J.C.Lee, IEDM Tech. Dig. 145 (1999)

[15] M.Copel, M.Gribelyuk, and E.Gusev, Appl.Phys.Lett. **76**, 436 (2000)

[16] J.Aarik, A.Aidla, A.A.Kiisler, T.Uustare, and V.Sammelselg, Thin Solid Films **340**, 110 (1999)

[17] B.H.Lee, L.Kang, W.-J.Qi, R.Nieh, Y.Jeon, K.Onish, and J.Lee, IEDM Tech.Dig. 166 (1999)

[18] K. J. Hubbard and D. G. Schlom, J. Mater. Res. **11**, 2757 (1996)

[19] G.Lucovsky, G.B.Rayner,Jr., D.Kang, G.Appel, R.S.Johnson, Y.Zhang, D.E.Sayers, and H.Ade. Appl. Phys. Lett. **79**, 2775 (2001)

[20] G.B.Rayner,Jr., D.Kang, Y.Zhang, and G.Lucovsky, J.Vac.Sci.Technol. B **20**, 1748 (2002)

[21] J.J.Chambers, A.L.P.Rotondaro, M.J.Bevan, M.R.Visokay, and L.Colombo, Electrochem. Soc. Proc. **26**, 359 (2002)

[22] C.H.Lee, H.F.Luan, W.P.Bai, S.J.Lee, T.S.Jeon, Y.Senzaki, D.Roberts, and D.L.Kwong, Int. Electron Devices Meet. 2000, 31 (2000)

[23] T.Ma, S.A.Campbell, R.Smith, N.Hoilien, B.He, W.L.Gladfelter, C.Hobbs, D.Buchanan, C.Taylor, M.Gribelyuk, M.Tiner, M.Coppel, and J.J.Lee, IEEE Trans. Electron Devices **48**, 2348 (2001)

[24] K.Onishi, L.Kang, R.Choi, E.Dhamarajan, S.Gopalan, Y.Jeon, C.S.Kang, B.H.Lee, R.Nieh, and J.C.Lee, Symposium on VLSI Tech. Digest of Tech. Papers, 131 (2001)

[25] K.S. Krisch, L.Manchanda, F.H. Baumann, M.L. Green, D.Brasen, L.C.Feldman and A.Ourmazd, IEDM Tech. Dig., pp.325-328 (1994)

[26] J.Y.C. Sun, C.Wong, Y.Taur and C.H. Hsu, 1989 Symp. VLSI Tech. Dig., 17 (1989)

[27] J.R.Pfiester, F.K.Baker, T.C.Mele, H.H.Tseng, P.J.Tobin, J.D.Hayden, J.W.Miller, C.D.Gunderson and L.C.Parrillo, IEEE Trans. Electron Devices, **ED-37**, pp1842-1851 (1990)

[28] M.L.Green, SRC Topical Res.Conf. On Critical Issues for Gate Dielectric Integration, May 11-12, Raleigh, NC (1994)

[29] G.W.Yoon, A.B.Joshi, J.Kim, and D.L.Kwong, Mat. Res. Soc. Symp. Proc. 303, 291 (1993)

[30] T.Aoyama, K.Suzuki, H.Tashiro, Y.Toda, T.Yamazaki, Y.Arimoto and T.Ito, J.Elecrochem Soc., 140, 3624 (1993), T.Aoyama, K.Suzuki, H.Tashiro, Y.Toda, K.Horiuchi, J.Elecrochem Soc., **145**, 689 (1998)

[31] K.A.Ellis and R.A.Buhrman J.Elecrochem.Soc., 145, 2068, (1998)

[32] H.Z.Massoud,E.H.Poindexter and C.R.Helms,Eds., pp.200-213 The Electrochemical Society, New Jersey, 1996.

[33] R.B.Fair J.Elecrochem. Soc., **144**, 717, (1997)

[34] T.Hori, Gate Dielectrics and MOS ULSI's (Springer, New York, 1997)

[35] P.Habas and S.Selberherr, Solid State Electronics, **33**, 1539, (1990)

[36] C.L.Huang and N.D.Arora, IEEE Trans.Electron Devices, **ED-40** 2330 (1993)

[37] M.R.Visokay, J.J.Chambers, A.L.P.Rotondaro, A.Shanware, and L.Colombo, Appl. Phys. Lett. **80**, 3183 (2002)

[38] A.L.P.Rotondaro, M.R.Visokay, J.J.Chambers, A.Shanware, R.Khamankar, H.Bu, R.T.Laaksonen, L.Tsung, M.Douglas, R.Kuan, M.J.Bevan, T.Grider, J.McPherson, and L.Colombo, Tech. Dig., VLSI Symp. 148 (2002)

[39] S.V.Hattangady, H.Niimi, and G.Lucovsky, J.Vac.Sci.Technol. A **14**, 3017 (1996)

[40] M.L.Laiman, F.L.Terry, J.A.Barns, J.I.Raffel, and R.Aucoin, IEDM Tech. Dig. 562 (1980)

[41] D.Landheer, Y.Tao, D.X.Xu, G.I.Sproule, and D.A.Buchanan, J. Appl. Phys. **78**, 1818 (1995)

[42] S.V.Hattangady, H.Niimi, and G.Lucovsky, Appl. Phys. Lett. **66**, 3945 (1995)

[43] R.Kurafut, T.P.Schneider, W.W.Dostalik, and S.V.Hattangady, J.Vac. Sci. Technol. B **15**, 967 (1997)

[44] H.Kobayashi, T.Mizokuro, Y.Nakato, K.Yoneda, and Y.Todokoro, Appl. Phys. Lett, **71**, 1978 (1997)

[45] F.H.P.M.Habraken and A.E.T.Kuiper, Mater. Sci. Eng., R. **12**, 123 (1994)

[46] W.L.Hill, E.M.Vogel, V.Misra, P.K.McLarty, and J.J.Wortman, IEEE Trans. Electron Devices **43**, 15 (1996)

[47] T.P.Ma, Appl, Surf. Sci. **117/118**, 259 (1997)

[48] J.S.Pan, A.T.S.Wee, C.H.A.Huan, H.S.Tan, and K.L.Tan, Appl. Surf. Sci. **115**, 166 (1997)

[49] H.Goto, K.Shibahara, and S.Yokoyama, Appl. Phys. Lett. **68**, 3257 (1996)

[50] D.Niu, R.W.Ashcraft, C.Hinkle, and G.N.Parsons J.Vac.Sci.Technol, A **22**, 445 (2004)

[51] D.A.Buchnan, IBM J. Res. Dev. **43**, 245 (1999)

[52] M.L.Green, E.P.Gusev, R.Degraeve, E.L.Garfunkel, J.Appl.Phys. **90**, 2057 (2001)

[53] A.Khandelwal, B.C.Smith, H.H.Lamb, J.Appl.Phys. **90**, 3100 (2001)

[54] A.Raveh, J.Brewer, E.A.Irene, J.Vac.Sci.Technol. A **17** (2001)

[55] B.Ju and G.Lucovsky (unpublished)

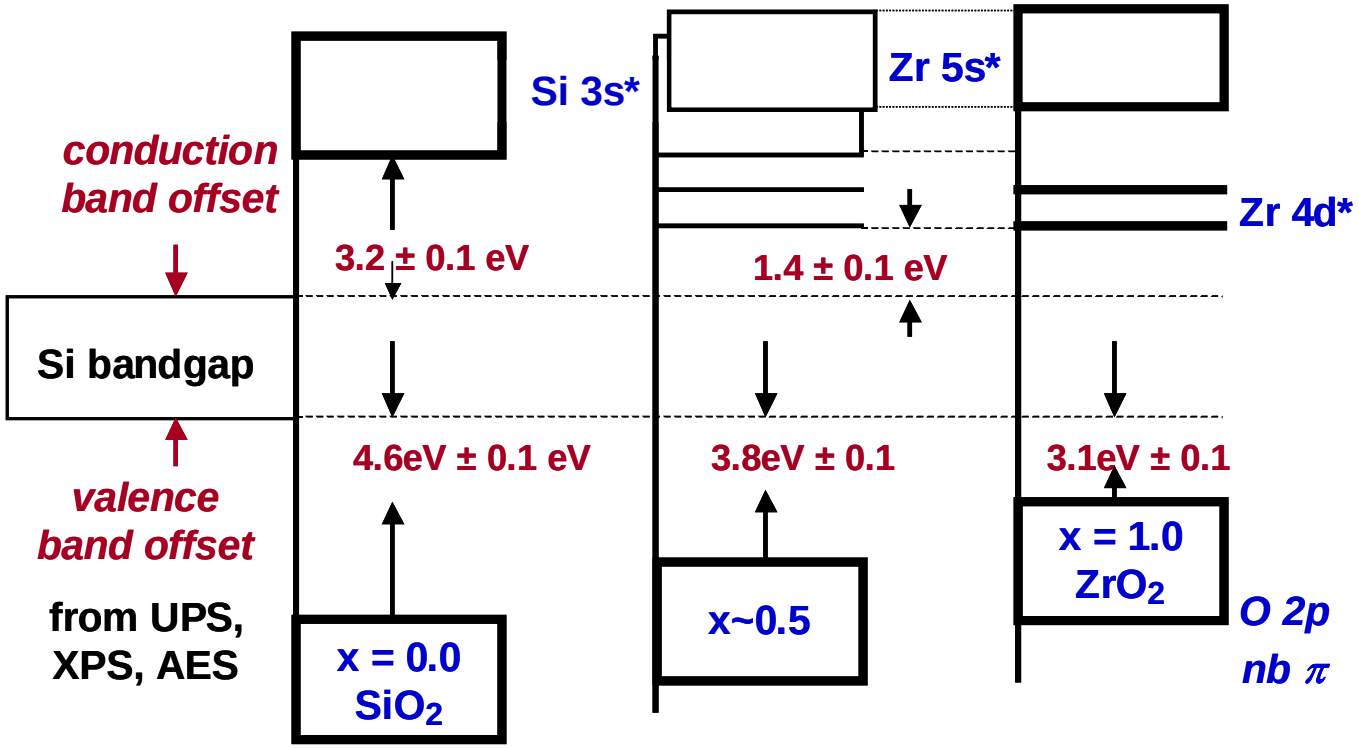

Figure 1.1. Composition dependence of band offset energies for Zr silicate alloys. [19]

CHAPTER 2. FILMS DEPOSITION.

2.1 Zr Silicate and Zr-Si Oxynitride Films Deposition

Remote Plasma Enhanced Chemical Vapor Deposition (RPECVC) system was used to deposit Zr silicate alloys, $(ZrO_2)_x(SiO_2)_{1-x}$, and its end member oxide (SiO_2 and ZrO_2) films, and Zr-Si oxynitride films [1]. This system has been used extensively by our research group and provided device quality gate dielectric for CMOS application. A cross section of the reactor and a detailed schematic of the Zr source gas delivery system [2] are illustrated in Figure 2.1. Plasma is excited in the top reactor and the source gases are diffused to bottom chamber. So the deposition occurs outside the flow region and plasma damage is minimized. The base pressure of the system was approximately 1×10^{-7} Torr. Si oxynitride $[(Si_3N_4)_y(SiO_2)_z]$ and Zr-Si oxynitride $[(ZrO_2)_x(Si_3N_4)_y(SiO_2)_z$, x+y+z=1] films are also deposited on Si (100) substrate kept at 300°C. A 1% nitrous oxide (N_2O-in-N_2) gas is used for a nitrogen source as well as oxygen source since O incorporation is significantly easier in comparison with N incorporation in deposition films. In deposition, Si oxynitride, the total amount of both N_2 and 1% N_2O gas are 200sccm. ZrO_2 and Si_3N_4 composition in Zr-Si oxynitride films were determined by adjusting the bubbler pressure and N_2/N_2O gas ratio, respectively.

Prior to the films deposition, the Si substrates were dipped in a H_2O/HF (100:1) solution just before Zr silicate and Zr-Si oxynitride deposition so the native oxide was removed and provided clean, hydrogen terminated, Si surface. The energy for deposition

comes from the RF power, 30W at 13.56MHz. This allows the substrate to be held at relatively low temperature, 300°C, which temperature is sufficient to desorb organics that may remain on the surface after cleaning and low enough to prevent thermal oxidation of the substrate by ambient oxygen. A mixture of helium and oxygen was subjected to remote plasma excitation, 15W at 13.56MHz and the deposition pressure in the chamber was controlled at 300mTorr. The Si and Zr source gases, 2% SiH_4 in He and Zr(IV) t-butoxide, were injected through two different shower head rings. The silicate composition in the deposited films can be controlled by the SiH_4 flow rate and by the bubbler pressure. Figure 2.2 shows the silicate composition as a function of SiH_4 gas flow rate and bubbler pressure. From the results, SiH_4 gas flow is more effective way to control Zr silicate composition. Prior to the silicate alloy deposition, an a-SiO_2 layer approximately 0.6nm thick was deposited on the Si substrate by RPECVD to provide strain-free layer.

2.2 Zr Metal Organic Bubbler

Zr source was extracted from a liquid in an Schumacher BK 1200 SSZ [3] stainless steel bubbler. The bubbler was immersed in a heat bath filled with silicone oil to maintain constant temperature (30°C). He gas was used as a carrier gas, caused some of liquid molecules to evaporate and be transported to the chamber. The boiling point of the liquid Zr source is 90°C at 760Torr; therefore, the gas line were kept at approximately 100°C and He gas was flowed constantly through the manifold to prevent MO precursor condensation in the lines [4]. Typically, the pressure was varied in the bubbler between

15 and 30Torr, where an increase in bubbler pressure results in a decrease Zr source gas injection so the silicate composition moved to SiO_2 as shown in Figure 2.2.

2.3 AES and RBS

AES was performed with a Physical Electronics 11-010 5kV electron gun control, 10-155 cylindrical mirror analyzer (CMA), 32-150 digital analyzer control, 137 PC interface board assembly, 96A V/f preamplifier, 32-100 electron multiplier power supply, and the software interface program AES_CGA. The auger process requires an energetic electron beam and sample damage is a concern. We use a minimal beam technique, i.e., the current of the beam is kept low and the detector multiplier voltage high. The beam is focused to attain a maximum number of counts [5,6]. In order to provide a repeatable technique and a minimal amount of beam current, the multiplier voltage is kept at a constant value and the filament current is varied to attain an appropriate number of counts. The multiplier value is 4.0 on the 32-100 power supply dial and corresponds to ~1,444 volts. For alignment purposes, the accelerating voltage is set a 2.0keV and the main elastic peak is aligned so its peak falls on 2.0keV and the filament current is adjusted so between 900~1000 kilo counts per second are obtained. This step ensures consistent results from run to run. Once this is accomplished, an AES scan at 3.0keV can be completed.

Zr silicate, pseudo-binary alloy, composition was determined by the ratio of intensity of Zr_{MNN} and O_{KVV} obtained from on-line AES and this figure was calibrated by RBS [7]. In the same way, the ratio of N_{KLL} to O_{KVV} in derivative curve of on-line AES

spectra measured from Zr-Si oxynitride alloy was also used to figure out the Si_3N_4 percentage. Figure 2.3 shows Schematic diagram of RBS technique. RBS spectra are acquired at backscattering angles of 160° and an appropriate grazing angle with the sample perpendicular to the incident ion beam. The different depth resolution and backscattering kinematics afforded by the use of different detection angles improve the accuracy of the analysis both in the thickness and stoichiometric results. The grazing angle detector spectra allow detailed information about changing composition in the surface layers. When the surface film and any polycrystalline Si and SiO_2 layers are thin enough, some channeling occurs in the single crystal Si substrate. This results in a reduction of the backscattering signal from the substrate to a level which does not correspond to 100 atomic percent. When this occurs, a channeling factor, denoted by Xx in the accompanying figures, is included which forces agreement between the theoretical curve and experimental spectra for the substrate signal. The RBS spectra are fit by applying theoretical model and iteratively adjusting elemental concentrations until good agreement is found between the theoretical curves and the respective experimental spectra. The simultaneous fitting of normal and grazing detector from both the RBS geometries assists in generating a theoretical model that is representative of the physical structure of the sample.

2.4 XPS and FTIR Analysis

Off-line XPS measurements of O1s, Zr3d, Si2p and N1s core levels were made off-line using a Riber LAS-3000 spectrometer with non-monochromatic Mg Kα radiation

(1256.6eV) and pass energy of 20eV. The spectral resolution was approximately 1eV. The system base pressure for XPS measurements was approximately 3×10^{-10}Torr. Data were corrected for charging effects using the C1s peak at 284.5eV from adventitious carbon contamination on the film surface.

Fourier Transform Infrared, FTIR, measurements were performed using a Nicolet Magna FTIR 750 spectrometer in the mid-IR (4000~400cm^{-1}) and far-IR (700~50cm^{-1}) range of the electromagnetic spectrum. The spectrometer was continuously purged with N_2 to minimize absorption from IR active components present in the atmosphere, such as H_2O and CO_2. The mid-IR measurements utilized a DTGS detector with a KBr window and a KBr beam splitter, while the far-IR measurements used a DTGS detector with a polyethylene window and a Si substrate beam splitter. The spectrometer utilized a He/Ne laser for optical bench alignment, which was performed prior to all data collection. Alloys were deposited on high resistivity Si (100) substrate to minimize absorption by free charge carriers. The substrates were polished on both sides to minimize multiple internal reflections. The thinner substrates have the advantage of smaller contributions from substrate IR absorption due to oxygen and carbon impurities and 2nd order IR active vibrations. In addition, the thinner substrates were better suited for far IR measurement down to 100cm^{-1} due to interference effects observed in the far IR spectral regime. Double side polished Si wafer was used for IR measurements. Prior to the films deposition, the Si wafers were dipped in a H_2O/HF (100:1) solution to remove the native oxide and to provide a clean, hydrogen terminated, Si surface. Film thickness was deposited thicker than approximately 150nm thick to ensure good IR absorption sensitivity.

2.5 Device Fabrication and Electrical Characterization

MOS capacitors were fabricated to investigate the effects of the films stabilities and alloy compositions on electrical properties. The capacitance-voltage was measured by a HP 4284A LCR meter at 1MHz and the current-voltage measurements were performed by a HP 4140B voltage source with a picoammeter. Approximately 4000Å thick of field oxide isolation were made on Si(100) substrate with carrier density of $>5\times10^{18}cm^{-3}$ (0.02~0.05 Ωcm). The use of heavily doped Si wafers reduces spreading resistance and thereby minimizes parasite series resistance, and accompanying voltage drops in the bulk Si. The active area was $1\times10^{-4}cm^2$.

Prior the films deposition, Remote Plasma Assisted Oxide (RPAO, SiO_x, $x<2$) was grown about 6Å on the top of silicon substrate as a buffer layer by exposing He/O_2 plasma. Direct substitution of plasma deposited nitrides for oxides without an interfacial oxide layer has been shown to degrade field effect transistor (FET) device currents in n-channel devices by about a factor of 2, and in p-channel devices by more that a factor of 10 [8,9], thereby nullifying any gains from the increased capacitance. It has been reported that ALCVD ZrO2, when directly deposited on Si without a native oxide layer, shows thickness non-uniformity and a rough interface [10,11]. Figure 2.4a shows the AES spectra obtained from wafer cleaned 1% HF solution and exposed to He/O_2 plasma. We can see carbon contamination did not removed in HF dipping, while C_{KLL} peak was disappeared and thin oxide layer was grown as exposing He/O_2 plasma. This thin oxide thickness as a function of exposing time was also shown in Figure 2.4b. Figure 2.5

displays the leakage current density distributions for NMOS capacitor of SiO_2 and 55% Zr silicate dielectric without and without RPAO. By depositing interfacial oxide layer, leakage current density distribution remarkably enhanced as shown in Figure 2.5. The samples were annealed in an Ar atmosphere using an AG Associates minipulse RTA. Forming gas annealing was performed at 400°C for 30min. in N_2/H_2 gas mixture and followed by ~300nm thick of Al evaporation and defined as a gate electrode. High frequency (1MHz) capacitance-voltage (CV) and current density-voltage (JV) were measured to investigate the leakage mechanisms.

2.6 REFERENCES

[1] T.Yasuda, Y.Ma, S.Habermehl, and G.Lucovsky, J. Vac. Sci. Tech. B **10**, 1884 (1992)

[2] D.M.Wolfe, K.Flock, R.Therrien, R.Johnson, B.Rayner, L.Gunther, N.Brown, B.Claflin, and G.Lucovsky, Mat. Res. Soc. Symp. Proc. 567, 343 (1999)

[3] http://www.schumacher.com.

[4] S.D.Hersee and J.M.Ballingall, J. Vac. Sci. Technol. A **8**, 800 (1990)

[5] L.E.Davis, N.C.MacDonald, P.W.Palnberg, G.E.Raich, and R.I.Weber, Handbook of Auger Electron Spctrocopy 2nd. De. (Physical Electornics Industries, Inc.) Eden Pairie, MN (1976)

[6] Y.Ma, T.Yasuda, and G.Lucovsky, J. Vac. Sci. Technol. B **11**, 1533 (1993)

[7] G.B.Rayner, Jr., D.Kang, Y.Zhang, and G.Lucovsky, J. Vac. Sci. Technol. B **20**, 1748 (2002)

[8] G.Lucovsky, Y.Wu, H.Niimi, V.Misra, and J.C.Phillips, Appl. Phys, Lett. **74**, 2005 (1999)

[9] V.Misra, Z.Wang, Y.Wu, H.Niimi, G.Lucovsky, J.J.Wortman, and J.R.Hauser, J. Vac. Sci. Technol. B **17**, 1836 (1999)

[10] C.M.Perkins, B.B.Triplett, P.C.McIntyre, K.C.Saraswat, S.Haukka, and M.Tuominen, Appl. Phys. Lett. **78**, 2357 (2001)

[11] M.Copel, M.A.Gribelyuk, and E.Gusev, Appl. Phys. Lett. **76**, 436 (2000.

[12] http://www.eaglabs.com/appsnotes.htm.

[13] http://www.cea.com/services/services.htm.

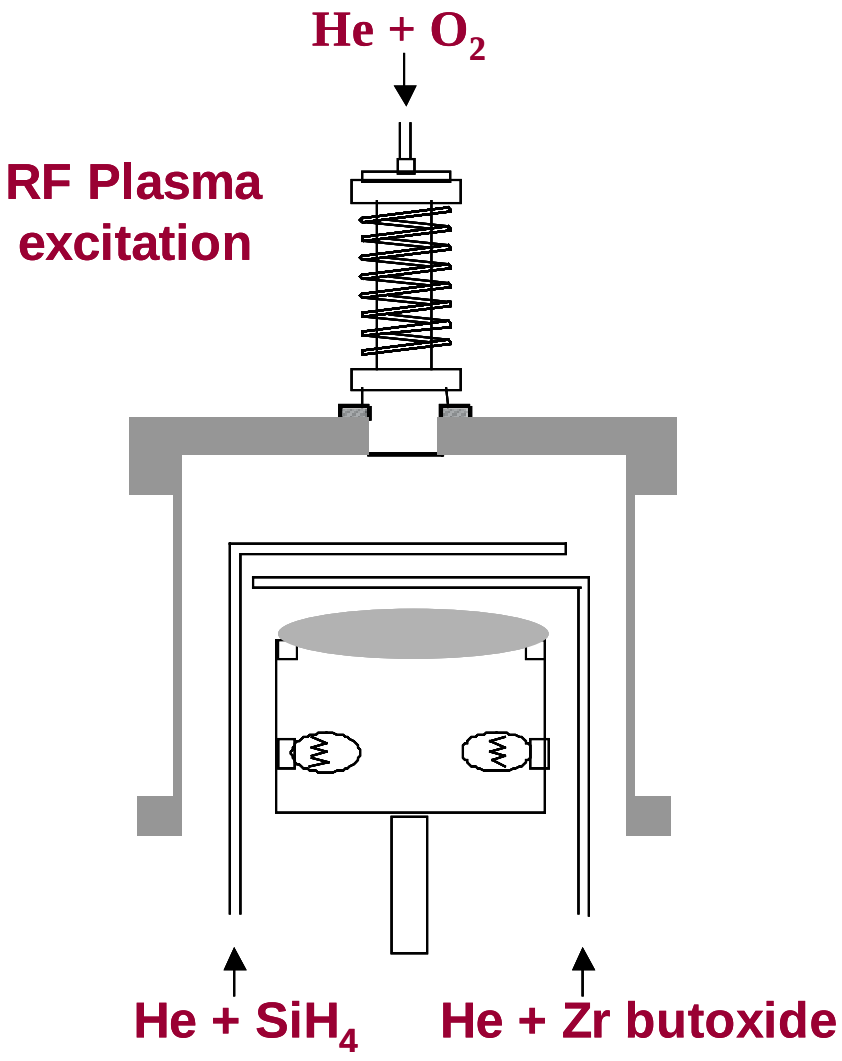

Figure 2.1. Schematic diagram of Remote Plasma Enhanced Chemical Vapor Ddeposition (RPECVD) chamber for depositions.

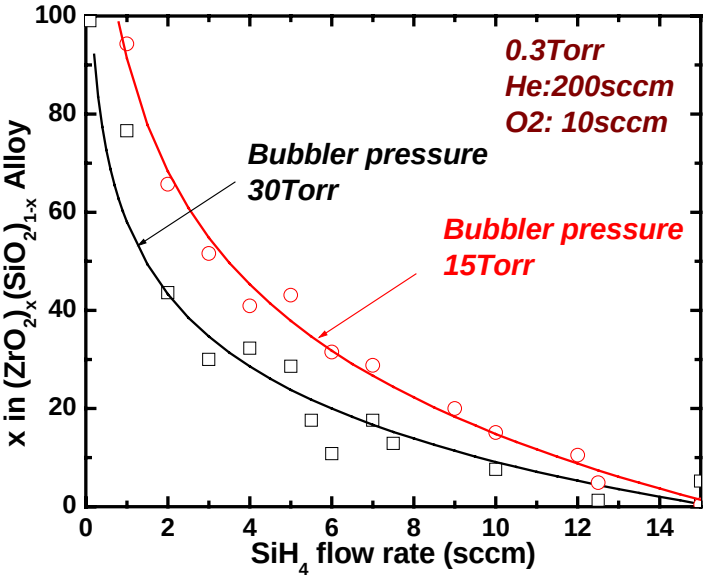

Figure 2.2. Composition of the RPECVD Zr silicate films, $(ZrO_2)_x(SiO_2)_{1-x}$, as a function of SiH_4 gas flow rate.

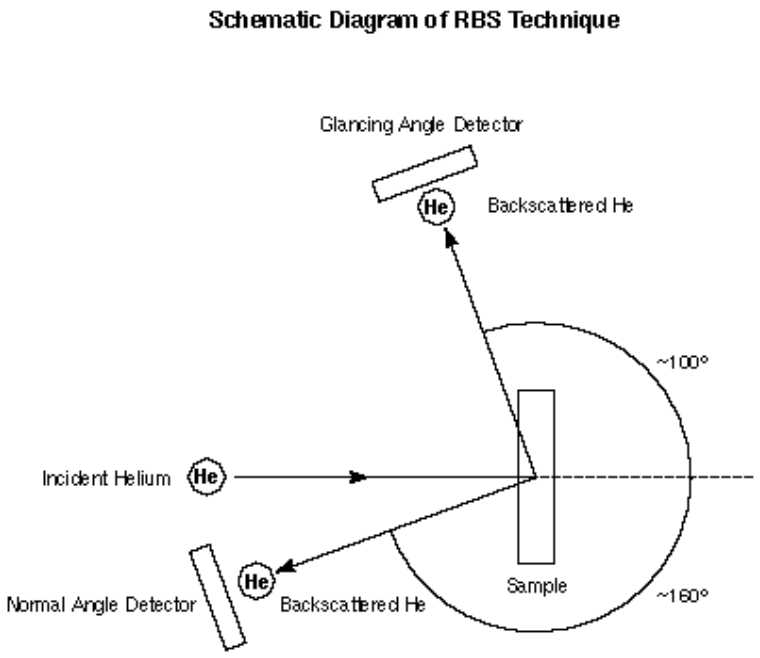

Figure 2.3. Schematic Diagram of RBS Technique [12].

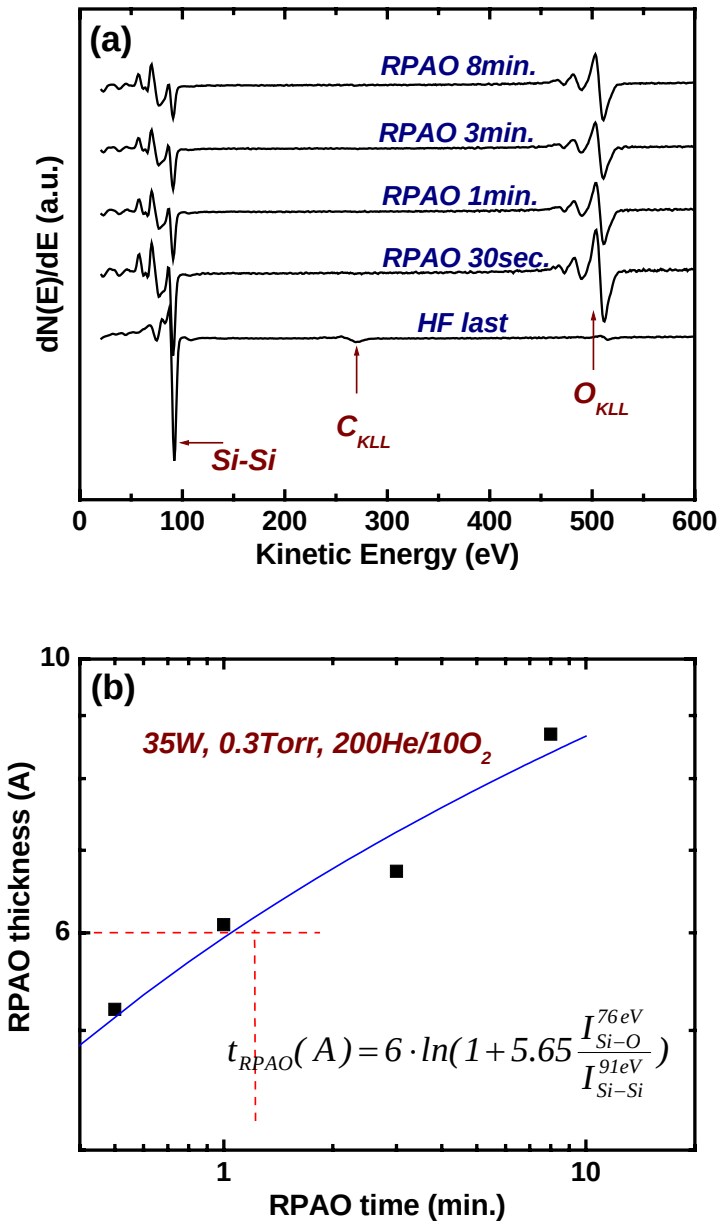

Figure 2.4. (a) The online AES derivative spectra from Si surface after 1wt.% of HF dip and after He/O_2 plasma oxidation (b) RPAO thickness as a function of He/O_2 plasma exposure time.

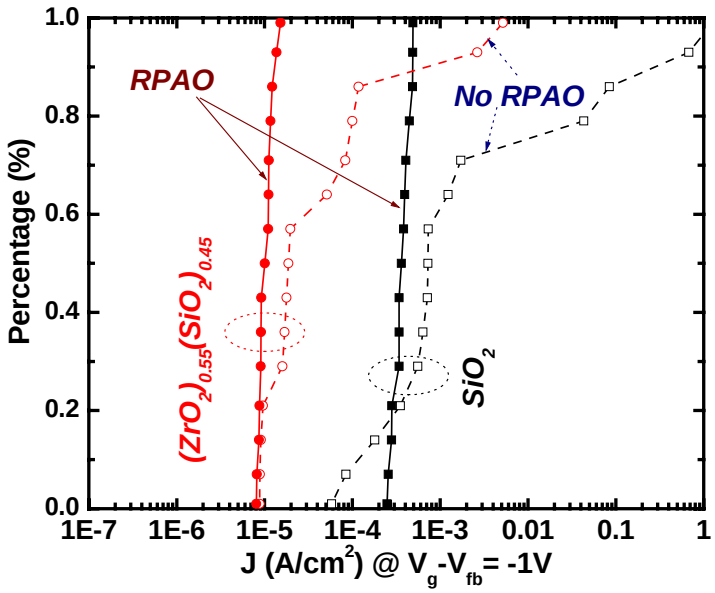

Figure 2.5. Leakage current density distribution at V_g-V_{fb}=-1V with and without RPAO in SiO_2 and $(ZrO_2)_{0.55}(SiO_2)_{0.45}$ silicate for NMOS capacitor.

Table 2.1 Analytical techniques and their limits and resolution. [13]

Analytical Technique	Detection Limits	Depth Resolution
AES	0.1~1 at%	2~6nm
Micro-FTIR	0.1~100ppm	-
RBS	Z<20 1~10 at% 20<Z<70 0.01~1 at% 70<Z 0.001~0.01 at%	2~20nm
XPS	0.01~1 at%	1~10nm
RAMAN	<0.1 wt%	1~2μm
SIMS	1e12~1e16 at/cc	5~30nm

CHAPTER 3. Dielectric Properties of ZrO_2 and Zr Silicate Alloys and Effect of N_2 Atoms Incorporated by Remote Plasma-Assisted Nitridation (RPAN)

ABSTRACT

In this investigation, Zr silicates and its end members (SiO_2 and ZrO_2) were deposited using a remote plasma-enhanced chemical vapor deposition (RPECVD) system and exposed to He/N_2 plasma to incorporate nitrogen atoms into the surface of films. The amount of incorporated nitrogen atoms was measured by on-line Auger electron spectrometry (AES) as a function of silicate composition and showed its local minimum around the 30% silicate. Characterization by AES and x-ray photoelectron spectroscopy (XPS) indicated that the nitrogen atoms were substituted for the oxygen atoms' position and made a bond with Si and Zr depending on the silicate composition. The effect of nitrogen atoms on capacitance-voltage (C-V) and leakage-voltage (J-V) were also investigated by fabricating metal-oxide-semiconductor (MOS) capacitors. Results suggested that incorporating nitrogen into silicate decreased the leakage current in SiO_2-rich silicate, whereas the leakage increased in the middle range of silicate.

3.1 INTRODUCTION

Aggressive scaling down of microelectronic devices for advanced complementary metal-oxide semiconductors (CMOS) is required to increase packing density of ultralarge-scale integrated circuits (ULSI). It is essential to have a thinner dielectric as well as smaller channel length and width to maintain the same drive currents needed for circuit operation [1~4]. However, SiO_2 or Si oxynitride (SiO_xN_y) films, which are a traditional gate-oxide materials, show their limitations in direct tunneling current density at below about 3nm thickness, and moreover, the priority of leakage current is ranked high in device performance and reliability as the portable device prevails [5~7]. So intensive research has been focused on high dielectric constant materials as an alternative replacement for SiO_2 by keeping the same equivalent-oxide thickness (EOT). There are several candidates for high-k dielectric materials such as Transition/Rare metal (TM/RE) oxides (ZrO_2, HfO_2, Y_2O_3, La_2O_3), TM/RE silicates [$(ZrO_2)(SiO_2)$], [$(HfO_2)(SiO_2)$], and TM/RE aluminates [$(ZrO_2)(Al_2O_3)$, $(La_2O_3)(Al_2O_3)$] [8~10]. Although silicates films have a less dielectric constant than oxide, silicates are thermally more stable on a Si substrate. In particular, it has been reported that because of the pinning of the d state of transit metal (conduction band edge), silicate films show less leakage current with the same EOT as that of TM/RE oxides films [11,12].

One of the other important problems that must be considered when using a poly-Si gate electrode is dopant penetration. The boron doped p^+ poly Si gate electrode for the p-channel metal-oxide silicon (PMOS) device improves the short channel effects. However, boron diffusion from the poly-Si gate electrode into the channel region through

the gate dielectrics can degrade PMOS device performance [13~15]. For example, boron diffusion into the channel region results in a large positive flat-band voltage shift, increases the sub-threshold slope and electron trapping, and decreases low-field mobility. In addition, boron diffusion degrades the process control by introducing a spread of threshold voltages. Therefore, for boron doped p^+ poly Si gate electrode applications, it is necessary to have a diffusion barrier in the gate oxide to prevent boron penetration into the Si substrate and the channel region [16~18]. Nitrogen atoms incorporated into the gate dielectric structure are one candidate for blocking boron diffusion. Aoyama studied that the diffusion coefficients of boron decreased as the nitrogen amount in the bulk oxynitride films increased [19]. Ellis proposed that the boron atoms diffused substitutionally for the Si atoms and the presence of a Si-N bond impeded substitution for the Si atom. The boron atoms hop from one Si site to the other Si site. The presence of Si-N bond blocked the boron atom hopping process [20]. Fair [21,22] predicted that a less than 10 at.% of nitrogen in the oxide has a negligible effect on boron diffusion. Therefore, to prevent the boron diffusion from the p^+ poly Si gate electrode to the Si substrate needs a higher concentration of nitrogen; e.g., at least 15~20 at.% of nitrogen at the Si/SiO_2 interface.

However, light interfacial nitridation optimizes device performance and reliability. To prevent boron diffusion at the Si/SiO_2 interface, heavy nitridation is required, because interfacial nitridation degrades many aspects of device performance and reliability. Additionally, even if boron diffusion is prevented by heavy nitridation at the Si/SiO_2 interface, boron can accumulate in the bulk oxide. This accumulated boron in the oxide causes reliability degradation under gate injection. A low boron-doping level in the poly-

Si gate electrode and a low temperature post implantation activation/drive-in anneal helps prevent severe boron penetration into the Si substrate. However, the low activated doping concentration at the poly Si/gate dielectrics results in poly Si depletion effects, causing poor device performance [23,24]. Therefore it is important to suppress boron penetration at the top surface of the oxide, because a boron-blocking barrier on top of the oxide will prevent boron diffusion into the bulk oxide and to the Si/SiO_2 interface. The heavy nitridation layer can be far from the Si/SiO_2 interface. A heavy nitridation layer on the top surface of the oxide is not expected to reduce the device performance and reliability [20]. Eventually incorporation nitrogen into top surface of dielectric films is supposed to be the most effective way to screen boron from poly electrode. The advantages [25,26] of using N_2 as a nitrogen source over other gas such as, NH_3 or N_2O, are following. 1) It is a hydrogen-free nitrogen source, so minimizes hydrogen incorporation in the oxynitride films. 2) Nitrogen gas is relatively inexpensive and available in very high purity grades. 3) No possibilities of physical thickness increases due to the formation of SiO_2 layer by oxygen source in N_2O. 4) It can easily be pumped out of the system unlike NH_3 that is plagued with condensation problems that lead to memory effects and subsequent process contamination.

In this study, we report that Zr silicate alloys and their end members (SiO_2 and ZrO_2) were deposited using remote plasma-enhanced chemical vapor deposition (RPECVD) system and the surfaces of those films were nitrided by in-situ plasma nitridation of N_2/He gas mixture. We then measured the concentration of incorporated nitrogen by on-line Auger electron spectroscopy (AES). Chemical bonding also was studied using x-ray photoelectron spectroscopy (XPS) before and after annealing. Based

on the spectroscopy result, the effects of the incorporated nitrogen atoms on the electrical properties of gate dielectric films depending on the silicate compositions were also investigated.

3.2 EXPERIMENTAL PROCEDURES

3.2.1 Films depositions.

Zr silicate alloys, $(ZrO_2)_x(SiO_2)_{1-x}$, and their end member oxide (SiO_2 and ZrO_2) films were deposited on Si(100) substrates kept at 300°C in a RPECVD process described in detail elsewhere [27,28]. The Si substrates were dipped in a H_2O/HF (100:1) solution just before Zr silicate deposition so that the native oxide was removed and provided clean, hydrogen terminated, Si surface. A mixture of helium and oxygen was subjected to remote plasma excitation, 15W at 13.56MHz and the deposition pressure in the chamber was controlled at 300mtorr. The Si and Zr source gases, 2% SiH_4 in He and Zr(IV) t-butoxide, were injected through two different shower head rings. The silicate composition in the deposited films was controlled by the SiH_4 flow rate and by the bubbler pressure. The pseudo-binary alloy composition was determined by the ratio of intensity of Zr_{MNN} and O_{KVV} obtained from on-line AES and this number was calibrated by Rutherford Back Scattering (RBS). Prior to the silicate alloy deposition, an a-SiO_2 layer approximately 0.6nm thick was deposited on the Si substrate by RPECVD to provide a strain-free layer.

3.2.2 N_2/He plasma nitridation.

For the surface nitridation, silicate film was exposed to a He/N_2 mixture plasma for 30 min. at the same chamber. The process pressure was 30mtorr. Our previous studies [29] revealed that the location of incorporated nitrogen be controlled by the process pressure, which control the balance between neutral and charged nitrogen species injected into the process chamber. The active species for the interface nitridation are nitrogen atoms, whereas the active species for the top surface nitridation process in which the plasma afterglow penetrates into the deposition chamber are nitrogen ions. So it is obvious that nitrogen ions are considered active species, thereby nitrogen atoms pile up at top surface since the pressure is below 100mtorr. The amount of the incorporated nitrogen atomic percentage was measure by on-line AES using a 3keV electron beam and calculated from Eqn. (3.1)

$$[N]_{by\ AES} = \frac{I_N / S_N}{\sum_i (I_i / S_i)} \tag{3.1}$$

where I_i is the intensity in the AES spectrum defined as the peak-to-peak amplitude, and S_i is the sensitivity factor of respective species.

3.2.3 XPS analysis

XPS measurements of O 1s, Zr 3d, Si 2p, and N 1s core levels were made off-line using a Riber LAS-3000 spectrometer with non-monochromatic Mg Kα radiation (1256.6eV) and pass energy of 20eV. The spectral resolution was approximately 1eV. The system base pressure for XPS measurements was approximately 3×10^{-10}torr. Data

were corrected for charging effects using the C1s peak at 284.5eV from adventitious carbon contamination on the film surface.

3.2.4 Device Fabrication and Electrical Characterization

N-channel metal-oxide semiconductor (NMOS) capacitors were fabricated to investigate the effect of nitrogen incorporated at the silicate surface on electrical properties. Field-oxide isolation approximately 400nm thick was made on a p-type Si(100) substrate with carrier density of $>5\times10^{18}cm^{-3}$ (0.02~0.05 Ωcm). The active area was $1\times10^{-4}cm^2$. After the silicate deposition, half of the silicate film was screened by scrap of Si wafer and then the film was exposed to He/N_2 plasma, so that nitrogen atoms were incorporated into only half area of the silicate. Except the surface nitridation, all of MOS capacitors are flowed identical processes that the effects of incorporated nitrogen atoms on the electrical properties were investigated. The samples were annealed at 800°C, which is below temperature for the phase separation and crystallization temperature, in an Ar atmosphere for 1 min. using an AG Associates minipulse RTA. Forming gas annealing was performed at 400°C for 30 min. in a N_2/H_2 gas mixture and followed by evaporation of ~300nm thick of Al and electrode area was defined as a gate electrode. High-frequency capacitance-voltage (CV) and current-density-voltage (JV) were measured, and then compared to the effect of the incorporated nitrogen atoms.

3.3 RESULTS AND DISCUSSION

3.3.1 Incorporation of Nitrogen on Top Surface of Zr Silicate

Figure 3.1(a) shows the evolution of the on-line AES derivative spectra, dN(E)/dE, from varying composition of $(ZrO_2)_x(SiO_2)_{1-x}$ alloys and the differential's end member after surface nitridation for 30 min. at 300°C. No evidence of carbon (C_{KVV}) is shown in the detection limit of this AES system. The amount of incorporated nitrogen atoms by nitridation for 30 min. as a function of the silicate compositions was shown in Figure 3.1(b). The amount of incorporated nitrogen atoms was calculated from equation (3.1) and, depending on the silicate composition, showed different features. Generally, the incorporated nitrogen amount decreased linearly as the silicate composition moved from SiO_2 to ZrO_2. But no linear relationship between the nitrogen atom and silicate composition percentage is shown in the SiO_2-rich silicate ($x<0.3$). Our previous IR results [30] revealed that C–H and O–H bonds were present in the as deposited alloys, and that O–H in the form of H_2O is present in SiO_2-rich alloys ($x<0.3$) and the concentration of H_2O was observed decreasing with increasing ZrO_2 percentage in silicate. The decrease in the amount of H_2O is consistent with the increase in the average number of Zr–O bonds with increasing alloy composition, where donor-acceptor pair bonds are replaced with ionic Zr–O bonds. Following heat treatment at 600°C for 60s, no evidence of C–H bonding is indicated. However, even after annealing at 900°C for 60 sec. water is still detected in SiO_2-rich alloys. Therefore the non-linear character of the incorporated nitrogen atoms in the SiO_2-rich silicate is interpreted by the presence of H_2O bonding.

To understand the bonding behavior of incorporated nitrogen atoms in a silicate, all of the content elements of silicate before and after plasma nitridation were plotted in Figure 3.2(a) and Figure 3.2(b). The elemental concentrations in atomic percent for Zr, Si, O, and N atoms in the silicate as a function of silicate composition were derived using the Eq. (3.1). Using plasma nitridation, we can see two types of elements' characteristics. First, the amount of Si atoms remained the same, even after incorporating nitrogen atoms in all of the silicate composition, while the amount of Zr atoms was decreased approximately 5% in the middle range of the silicate (x = 0.3~0.8) after nitridation. But by using plasma nitridation, the atomic percentage of oxygen atoms decreased remarkably after plasma nitridation through all of silicates. And this decrement is well related to the amount of incorporated nitrogen. So the sum of nitrogen and oxygen atomic percentages after plasma nitridation was almost the same value of oxygen percents before nitridation. These results suggest that the incorporated nitrogen atoms break the oxygen atom bonding and (or) are substituted for the oxygen atom site [31]. And these substituted nitrogen atoms showed two different characteristic for the SiO_2-rich silicate ($x<0.3$, no reaction with Zr atoms) and the middle range of the silicate (x = 0.3~0.8, the decrease of amount of Zr atoms). This boundary is in good agreement with the non-linear character of the incorporated nitrogen amount in the SiO_2-rich silicate as shown in Figure 3.1(b).

Figure 3.3(a) shows the incorporated nitrogen concentration of SiO_2, 50% silicate and ZrO_2 films as a function of plasma nitridation time. The incorporated nitrogen concentration increased quickly with time and tended to saturate at approximate 30 min. exposure to He/N_2 plasma. This incorporated nitrogen concentration also shows above

tendency with silicate and its end members. The saturation behavior implies that the nitrogen is incorporated into several molecular layers on the top surface films and that this thin nitrided layer prevents the further nitridation of the Si surface, so that the process is self-limiting [25]. The incorporated nitrogen amount sharply decreased as the pressure increased as shown in Figure 3.3(b). The major nitrogen species in plasma at low pressure are charged ions, while the dominant nitrogen species at high pressure are neutral atoms. The charged ions in low pressure are piled up at the silicate surface within the AES skin depth that the incorporated nitrogen amounts detected by AES are larger at low pressure than higher pressure.

3.3.2 XPS Binding Energies with Alloy Composition

Figure 3.4 show the XPS binding energies of Si 2p, Zr 3d, and O 1s core levels of as-deposited films as a function of silicate composition. The spectra shown in Figure 3.4 are for films before nitridation and after nitridation. The SiO_2 rich silicate films are approximately 10nm thick, whereas thickness of the middle range of silicate is 5nm. So the peak for the Si substrate (~98eV) can be seen in the 56% silicate films. Figure 3.5 shows the evolution of differential AES spectra and XPS core-level Si 2p spectra by depending on the thickness of 60% Zr silicate. No composition changes were detected by increasing the film thickness from AES analysis in Figure 3.5(a). Two Si 2p peaks were detected for the thin film (deposition time 8min.), one is assigned for silicate at 101.5eV and another peak is assigned for Si substrate at 98eV. And the intensities are comparable for both peaks. But as the films thickness increased, the intensity for Si 2p peak at 101.5eV was maintained, whereas the the intensity for Si substrate was decreased as

shown in Figure 3.5(b). The binding energies of silicate elements decrease linearly with increasing alloy composition. The binding energy decrease can be explained by the charge transfer-theory [32~34]. It was reported [30] that the core-level chemical shifts can be related to a change in alloy composition as shown in Eqn. (3.2)

$$\Delta E_B(A) = k_A \Delta\delta_A + \Delta\Phi_A = k_A a_A \Delta x + \Delta\Phi_A \qquad (3.2)$$

where $\Delta E_B(A)$ is chemical shifts and $\Delta\Phi A$ is coulomb and/or final state effects. Because of a linear-compositional dependence in XPS binding energies, changes represented by $\Delta\Phi_A$ do not contribute significantly to chemical shifts. The linear relationship between the core-level binding and silicate-alloy composition is maintained after plasma nitridation. But the binding energies of Si 2p, Zr 3d and O 1s shift to lower energies after surface nitridation in the SiO_2-rich silicate. The binding energy shows the same trend after annealing. As previously mentioned, incorporated nitrogen atoms broke the oxygen-atom bonding and made a bonding of Si-N.

The Pauling electronegativity of N atom (3.04) is smaller than that of O (3.44) atoms, this means that the valence electron of N atoms will move farther from nuclei by surrounded O atoms [35]. As a result, the core electrons will be attracted more tightly by the protons in the nuclei, which makes the increase of BE for core electrons. The shift (decrease) of O1s binding energy is due to substitution of the second neighbor oxygen atom. According to the incorporated nitrogen atomic percentage measured by AES, even though the amount of incorporated nitrogen atoms in middle range of silicates is larger, no chemical shifts are detected in the core level of Si 2p and O 1s, but the binding energy

of Zr 3d decreases. Based on the XPS binding-energy analysis shown in Figure 3.2, it is interpreted that the incorporated nitrogen atoms are substituted oxygen atoms that are almost connected with Si atoms in SiO_2-rich silicates, whereas the incorporated nitrogen atoms make a bond with Zr atoms as well as Si atoms in the middle-range silicates.

The core level of N1s binding energy supports the fact that incorporated nitrogen atoms make a bonding with Zr as well as Si atoms in ~50% silicate alloy. Figure 3.6 shows the XPS core level of N1s of RPECVD plasma-nitrided Zr silicate films as-deposited and after annealing at 800°C in an Ar ambient. According to the N1s binding energy, there are several N1s peaks in silicate films, depending on their composition. First in the SiO_2 film, the N bonding at the binding energy 398.4 eV can be assigned to Si-O-N bonding. It is well known [30] that an oxygen atom has a two-fold coordinated network in a SiO_2-rich silicate (or SiO_2 films). Most of the oxygen atom's bonding is to the silicon atom and a small amount of the oxygen atoms' bonding is to Zr atoms. Therefore, nitrogen atoms substituted into oxygen atoms position relate mainly to the Si atom. As the concentration of ZrO_2 increases and network disruption becomes more prevalent, all oxygen atoms are three-fold coordinated to one Si atom of silicate and to two Zr^{4+} ions [30]. So the incorporated nitrogen atoms are bonded to both Si atoms (Si-O-N) and Zr atoms (N-Zr) in the middle range of the silicate (56%) as shown in Figure 3.6(a). In the ZrO_2-rich regime (or ZrO_2), most of the oxygen atoms are four-fold coordinated to Zr^{4+}. There is no nitrogen bonding with Si or Zr, but only donor-acceptor pair bonds (dative bonding, which can be shown only in a plasma-nitride film that one of the oxygen atoms can be thought of as attaching to the nitrogen via a co-ordinate bond

using the lone pair on the nitrogen atom) between non-bonding pairs of oxygen atoms and excited nitrogen atoms in ZrO_2 films [36].

This nitrogen bonding shows opposite characteristics after annealing. Figure 3.6(b) displays the XPS core level of N1s spectra of same silicate films after being annealed at 800°C for 60 sec. in Ar ambient. No change of nitrogen-binding energy (Si-O-N) was detected in SiO_2 films, while Si-O-N bonding remained even after annealing. However, the Zr-N peak disappeared in SiO_2-rich silicate films. In contrast, only Zr-N bonding is shown in the middle range of silicate films after annealing at 800°C for 60 sec. But all of the incorporated nitrogen atoms (dative bonding) disappeared in the ZrO_2 films. Therefore, no nitridation effect was expected in ZrO_2 films. Zirconium nitride (ZrN) is known as a metallic conductor, so ZrN is considered as a leakage source in a gate dielectric. [37,38]

Figure 3.7 shows the XPS core level binding energies of Si 2p, Zr 3d and O 1s of Zr silicate films (~5 nm thickness) with x=0.16, 0.32, 0.56%, and its end members annealed at various temperatures. Previously, our group showed [12,28] that silicate alloys (of ~20 nm thickness, chemically separated into c-ZrO_2 and SiO_2 (or a SiO_2-rich alloys) at 900°C annealing) for alloy compositions ranging from 50% to 60% silicate. It was well known that XPS is the most sensitive tool for detecting chemical phase separation [28,30]. Two peaks forming the distinct doublet (peaks from ZrO_2 and SiO_2 phases, respectively) were observed in the XPS O1s spectrum due to the chemical phase separation. But no evidence of phase separation was detected by XPS O1s in thinner silicate film (~5 nm thickness) of 56% ZrO_2 after annealing at 900°C in an Ar ambient. And the XPS binding energy of the O1s core levels showed no chemical shift in films of

SiO_2-rich silicates (x<0.5) after annealing at 900°C. No peak change was found up to 800°C in 100% ZrO_2 silicate, but the SiO_2-rich phase appears without changing the ZrO_2 peak when annealed at 900°C. This indicates that Si atoms break (diffuse) through remote plasma-assisted oxide (RPAO) layers and make a Si-O bonding. (No evidence of Zr-Si bonding associated with the silicide is observed.) Although no chemical shift and phase separation are detected up to 900°C RTA in the XPS O1s spectrum of the silicate composition, the peak positions of Zr and Si in the 56% silicate are shifted to higher energy after 900°C annealing but not moved in 12% and 24% silicates alloy, even after annealing at 900°C RTA. This means that the silicates of the middle range and ZrO_2 changed their compositions to a more SiO_2-rich alloy due to instability of the interface between the Si substrate and the silicate alloy.

3.3.3 The Nitridation Effect on Electrical Characterization

Figure 3.8 shows high-frequency (1 MHz) C-V measurements of 10%, 56% silicate, and ZrO_2 gate dielectric NMOS devices with and without plasma nitridation. In order to examine the effect of plasma nitridation, the capacitance was normalized to the accumulate capacitance of each composition before nitridation. The capacitances of all the compositions of silicate were increased by plasma nitridation. The equivalent oxide thickness (EOT) of 10%, 56% silicate, and ZrO_2 before plasma nitridation was 3.1, 2.7, and 1.9 nm, respectively. Each EOT was decreased to 2.8, 2.4, and 1.8 nm after plasma nitridation. Since the dielectric constant of SiO_xN_y is higher than that of SiO_2, these decreases in EOT reduction are attributed to the top surface layer being converted into silicon oxynitride by incorporated nitrogen.

But the flat-band voltage for both films (before and after plasma nitridation) did not shift in SiO_2-rich and ZrO_2-rich silicate, whereas V_{fb} moved approximately 100mV to a negative direction, indicative of a positive fixed charge, after nitridation in the middle range of silicate as shown in Figure 3.9. ΔV_{fb} is the difference between V_{fb} with nitridation and V_{fb} without nitridation films. No V_{fb} shift in SiO_2-rich and ZrO_2 films means that the incorporated nitrogen atoms remained at the top surface of the gate dielectric and are not considered to diffuse to the dielectric bulk or Si substrate interface. One of the purposes of top surface nitridation is to prevent boron diffusion from the boron-doped p^+ poly Si gate electrode [13~15]. As previously mentioned, the amount of incorporated nitrogen atoms showed their local maximum in the middle range of the silicate and the incorporated nitrogen atom makes a bond with Zr, as well as Si, in those silicates. So these results suggest that the incorporated nitrogen atoms act as a positive charge by bonding with Zr and that this is the cause of the V_{fb} shift to the negative direction.

Figure 3.10 displays leakage-current density (A/cm^2)-electric field (MV/cm) plots for a capacitor fabricated on a p-type substrate (NMOS) and an Al gate electrode with and without nitridation over various silicate composition dielectrics. An electric field was obtained from Eqn. (3.3), V_{fb} was compensated and here $T_{ox,eq}$ is the equivalent oxide thickness (EOT).

$$E_{ox} = \frac{V_{ox}}{T_{ox,eq}} = \frac{V_g - V_{fb}}{T_{ox,eq}} \tag{3.3}$$

From these J-V results we can see that incorporated nitrogen displays remarkably different behavior for electrical properties, depending on the silicate composition. First, the leakage-current density decreased at the SiO_2-rich silicate (x<30%) with plasma nitridation, as shown in Figure 3.10(a). A gradual increase in the current was observed at low voltage in films both with and without nitridation while a rapidly increased current and breakdown were observed at high voltage without nitridation. Nitrided (with nitridation) silicate film had a lower leakage current density compared to silicate film without nitridation, even though the equivalent oxide thickness of plasma-nitrided silicate is thinner (lower EOT), is attributed to incorporated nitrogen atoms that substituted oxygen atoms and eventually made the dielectric constant increase for SiO_xN_y films. And the lower current density can also be explained by the lower trap concentration at the nitrided silicate. The same results are shown at the C-V plot (Figure 3.8) and the analysis of the XPS core level of N1s. The incorporated nitrogen bonding of SiO_2-rich films changes to more stable Si-O-N bonding after 800°C annealing. Second, the leakage-current density in the range of the middle silicate (~50%) was higher at all gate voltages. As shown in Figure 3.8(b), an accumulation capacitance was increased after plasma nitridation in the middle range of silicate. It is known that the oxygen atoms in the middle range of silicate are three-fold coordinated to one Si atom of silicate and two Zr^{4+} ions. So incorporated nitrogen atoms are connected with Si atoms, as well as Zr atoms. It is also confirmed by the XPS analysis that both the Si-N and the Zr-N bonds are formed in as-deposited film and eventually only the Zr-N bond remains after annealing. Therefore, it is concluded that the increase of leakage current of nitrided films in the middle range of silicate is due to the presence of the ZrN bonding. The ZrN bonding is known as a

metallic conductor and is supposed to act as a leakage source in silicate films. Finally, there is no difference in the leakage-current density between ZrO_2 films with and without nitridation. It is expected from the XPS analysis that most of the incorporated nitrogen atoms made dative bondings in ZrO_2 film and that these bondings were disappeared by subsequent annealing. Therefore, no nitridation effect is expected in ZrO_2 films.

3.3.4 The Effect of Annealing Temperature on Nitrogen Bonding

Figure 3.11 shows the evolution of the incorporated nitrogen amount by annealing temperature. The amounts were measured by AES analysis after nitridation and annealing at 700, 800 and 900°C, respectively. The incorporated nitrogen by silicate composition was same trend as nitridation. The amounts of nitrogen decreased sharply in the middle range of silicate with increasing annealing temperature but saturated in the SiO_2-rich silicate. Eventually, nitrogen atoms incorporated in SiO_2 films resisted relatively their bonding to silicon atom against subsequent heat budget, whereas zirconium nitride lost their bonding by annealing.

3.4 CONCLUSION

The results presented in this article have demonstrated that nitrogen atoms were incorporated in a Zr silicate and its end member by exposing He/N_2 plasma in a RPECVD system. The amount of incorporated nitrogen atoms decreased linearly as the silicate composition went from SiO_2 to ZrO_2, but the amount showed its local minimum in SiO_2-rich silicate ($x<0.3$). This non-linear character of the incorporated nitrogen atoms

is interpreted by the presence of H_2O bonding in SiO_2 rich silicate. And AES spectra suggested that the incorporated nitrogen atoms were substituted for the oxygen atom. Since the oxygen atoms in a silicate have a two-fold coordinated network in a SiO_2-rich silicate, these incorporated nitrogen atoms made a bonding with Si atoms. Therefore, the XPS core level of the Si binding energy decreased after nitridation. As the concentration of ZrO_2 increased, the oxygen atoms were three-fold coordinated to one Si atom of silicate and two Zr^{4+} ions. Therefore, incorporated nitrogen atoms made a bonding with both Si and Zr atoms and the nitrogen atoms, eventually showed their local maximum in the middle range of the silicate, as found by AES analysis. This is also supported by the XPS bonding analysis.

The stability of the nitrogen bonding showed a different character in annealing. Only Si-N bonding (or Si-O-N) remained after annealing at 800°C in a SiO_2-rich silicate. In contrast, Si-N bonding disappeared after annealing, whereas Zr-N bonding remained and became a major bonding in the middle range of the silicate. The nitrogen atom incorporated into ZrO_2 became a dative bonding due to activation by plasma, and eventually disappeared after annealing. (No nitrogen atoms were detected by XPS analysis.) This finding is in good agreement with the nitrogen amount obtained from AES analysis. Overall, we obtained different electrical characteristics depending on the silicate composition. The EOT of all the range of silicates decreased after incorporating nitrogen into the silicates' surfaces. And both in SiO_2-rich and ZrO_2 films, there was no V_{fb} shift. However, there was a shift to the negative direction in the middle of the silicate. This shift is attributed to the local maximum of incorporated nitrogen atoms. This finding is also supported by the leakage-current-density vs. gate voltage analysis. The leakage

current decreased due to the incorporation of nitrogen into the SiO_2 silicate, whereas the increase in the middle-range silicate was due to the remaining ZrN bonding, which is considered a leakage source in the gate dielectric. As was expected from XPS analysis in ZrO_2 films, no change of leakage-current-density was detected. Therefore, incorporating nitrogen into silicate decreased the leakage current in the SiO_2-rich silicate, whereas the leakage current increased in the middle range of the silicate.

3.5 REFERENCES

[1] T. Hori and H. Iwasaki, IEEE Electron Device Lett. **10**, 195 (1989)

[2] H. Hwang, W. Ting, D.-L. Kwong, and J.Lee, IEEE Electron Device Lett. **12**, 495 (1991)

[3] Y. Okada, P. J. Tobin, K. G. Reid, R. I. Hegde, B. Maiti, and S. A. Ajuria, Symp. VLSI Tech. Dig. Tech. Papers **105,** (1994)

[4] M. Bhat, L. K. Han, D. Wristers, J. Yan, D. L. Kwong and J. Fulford, Appl. Phys. Lett. **66**, 1225 (1995)

[5] D.A. Buchanan, E.P. Gusev, E. Cartier, H. Okorn-Schmidt, K. Rim, M.A. Gribelyuk, A. Mocuta, A. Ajmera, M. Copel, S. Guha, N. Bojarczuk, A. Callegari, C. D. Emic, P. Kozlowski, K. Chen, R.J. Fleming, P.C. Jamison, J. Browin, and R. Ardnt, Tech. Dig. Int. Electron Device Meet., p.223 (2000)

[6] D. Park, Y-C. King, Q. Lu, T-J. King, C. Hu, A. Kalnitsky, S-P. Tay, and C-C. Cheng, IEEE Electron Device Letters, Vol. 19, No. 11, 441 (1998)

[7] Y. Wu, G. Lucovsky and H.Z.Massoud, Proc. IEEE International Reliability Physics Symp., 70 (1998)

[8] A. S. Kao, J. Appl. Phys. **69**, 3309 (1991)

[9] W.-J. Qi, R. Nieh, B.H. Lee, L. Kang, Y. Jeon, K. Onishi, T. Nagi, S. Banerjee, and J.C. Lee, Tech. Dig. Int. Electron Device Meet., 63 (1999)

[10] M. Copel, M. Gribelyuk, and E. Gusev, Appl. Phys. Lett. **76**, 436 (2000)

[11] K. J. Hubbard and D. G. Schlom, J. Mater. Res. **11**, 2757 (1996)

[12] G. Lucovsky, G. B. Rayner, Jr., D. Kang, G. Appel, R. S. Johnson, Y. Zhang, D. E. Sayers, and H. Ade. Appl. Phys. Lett. **79**, 2775 (2001)

[13] K. S. Krisch, L. Manchanda, F. H. Baumann, M. L. Green, D. Brasen, L. C. Feldman and A. Ourmazd, IEDM Tech. Dig., 325 (1994)

[14] J. Y. C. Sun, C. Wong, Y. Taur and C. H. Hsu, 1989 Symp. VLSI Tech. Dig., **17** (1989)

[15] J. R. Pfiester, F. K. Baker, T. C. Mele, H. H. Tseng, P. J. Tobin, J. D. Hayden, J. W. Miller, C. D. Gunderson and L. C. Parrillo, IEEE Trans. Electron Devices, **37**, 1842 (1990)

[16] M. L. Green, SRC Topical Res.Conf. On Critical Issues for Gate Dielectric Integration, May 11-12, Raleigh, NC (1994)

[17] E. C. Car and R. A. Buhrman, Appl. Phys. Lett. **63**, 54 (1993)

[18] G. W. Yoon, A. B. Joshi, J. Kim, and D. L. Kwong, Mat. Res. Soc. Symp. Proc. **303**, 291 (1993)

[19] T. Aoyama, K. Suzuki, H. Tashiro, Y. Toda, T. Yamazaki, Y. Arimoto and T. Ito, J. Elecrochem Soc., **140**, 3624 (1993), T. Aoyama, K. Suzuki, H. Tashiro, Y. Toda, K. Horiuchi, J. Elecrochem Soc., **145**, 689 (1998)

[20] K. A. Ellis and R. A. Buhrman J. Elecrochem.Soc., **145**, 2068 (1998)

[21] H. Z. Massoud, E. H. Poindexter and C. R. Helms,Eds., 200 The Electrochemical Society, New Jersey, (1996)

[22] R. B. Fair J. Elecrochem. Soc., **144**, 708 (1997)

[23] P. Habas and S. Selberherr, Solid State Electronics, **33**, 1539 (1990)

[24] C. L. Huang and N. D. Arora, IEEE Trans.Electron Devices, **40**, 2330 (1993)

[25] S. V. Hattangady, H. Niimi, and G. Lucovsky, J. Vac. Sci. Technol. A **14**, 3017 (1996)

[26] M. L. Laiman, F. L. Terry, J. A. Barns, J. I. Raffel, and R. Aucoin, IEDM Tech. Dig. **562** (1980)

[27] G. Lucovsky, IBM J. Res. Dev. **43**, 301 (1999)

[28] G. B. Rayner, Jr,. D. Kang, Y. Zhang, and G. Lucovsky, J. Vac. Sci. Technol. B **20**, 1748 (2002)

[29] H. Niimi and G. Lucovsky, J. Vac. Sci. Technol, B **17**, 2610 (1999)

[30] G. B. Rayner, Jr,. D. Kang, and G. Lucovsky, J. Vac. Sci. Technol. B **21**, 1783 (2003)

[31] Y. Uraoka, H. Yano, T. Hatayama and T. Fuyuki, Jpn. J. Appl. Phys. **41**, 3637 (2002)

[32] K. Siegbahn, et. al., in ESCA Applied to Free Molecules (North-Holland Publishing Co., Amsterdam), (1969)

[33] D. Briggs and M. P. Seah, in Practical Surface Analysis (Wiley, Chichester), pg.420, (1990)

[34] M. J. Guittet, J. P. Crocombette, M. Gautier-Soyer, Phys. Rev. B **63**, 125117 (2001)

[35] Y.S.Lai and J.S.Chen, y, J. Vac. Sci. Technol. A **21**, 772 (2003)

[36] G.V.Soares, K.P.Bastos, R.P.Pezzi, L.Miotti, and C.Driemeier, I.J.R.Baumvol, C.Hinkle and G.Lucovsky, Appl. Phys. Lett. **84**, 4992 (2004)

[37] R.Nieh, C.S.Kang, H.J.Cho, K.Onishi, R.Choi, S.Krishnan, J.H.Han, Y.H.Kim, M.S.Akbar and J.Lee, IEEE Trans. Electron Device, **50**, 333 (2003)

[38] I.Milosev, H.H. Strehblow, B.Navinsek and P.Panjan, Surface Science Spectra, **5**, 152 (1998)

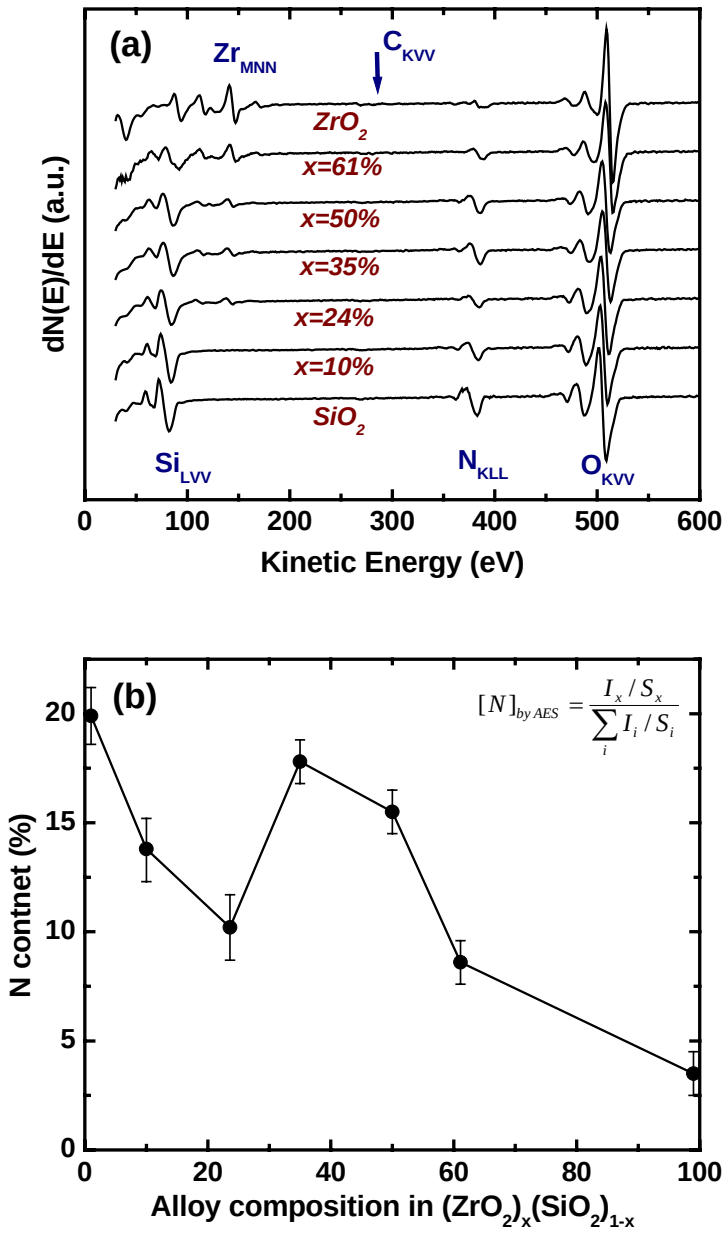

Figure 3.1. (a) Differential AES spectra from various composition of $(ZrO_2)(SiO_2)$ alloys after surface nitridation and (b) The amount of incorporated nitrogen as a function of silicate composition.

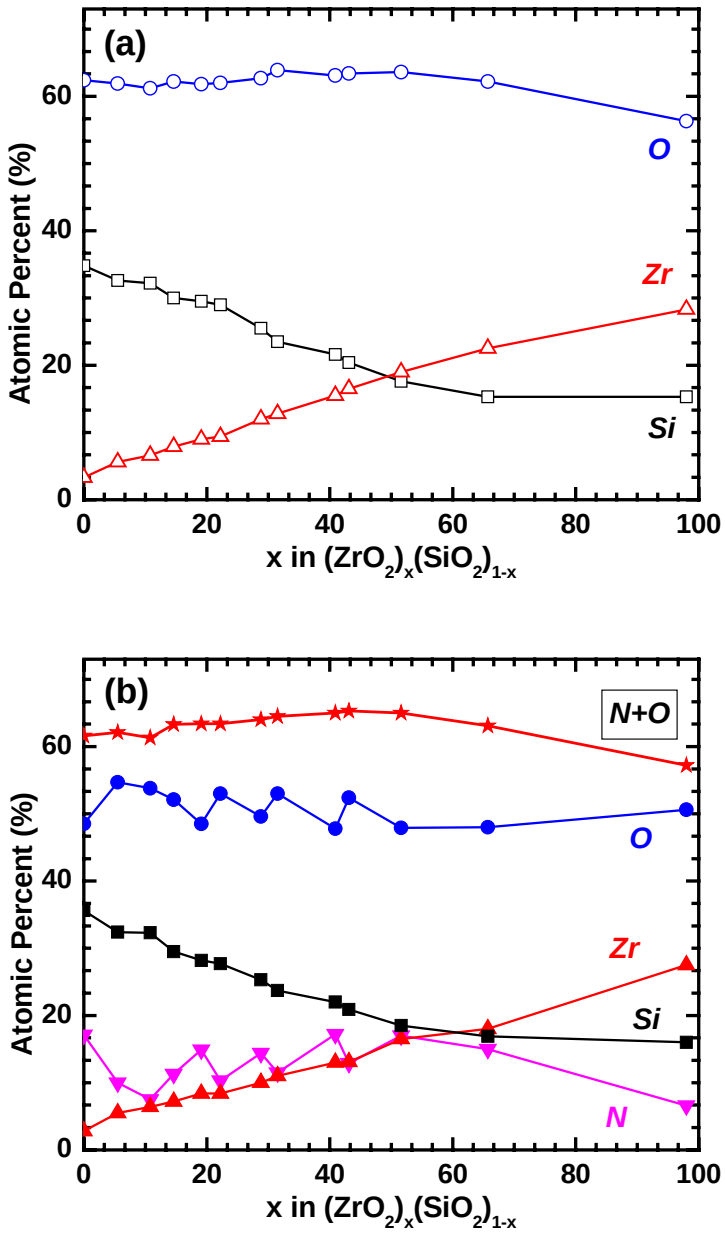

Figure 3.2. Comparison of the elemental concentrations in Zr silicates (a) before and (b) after nitridation.

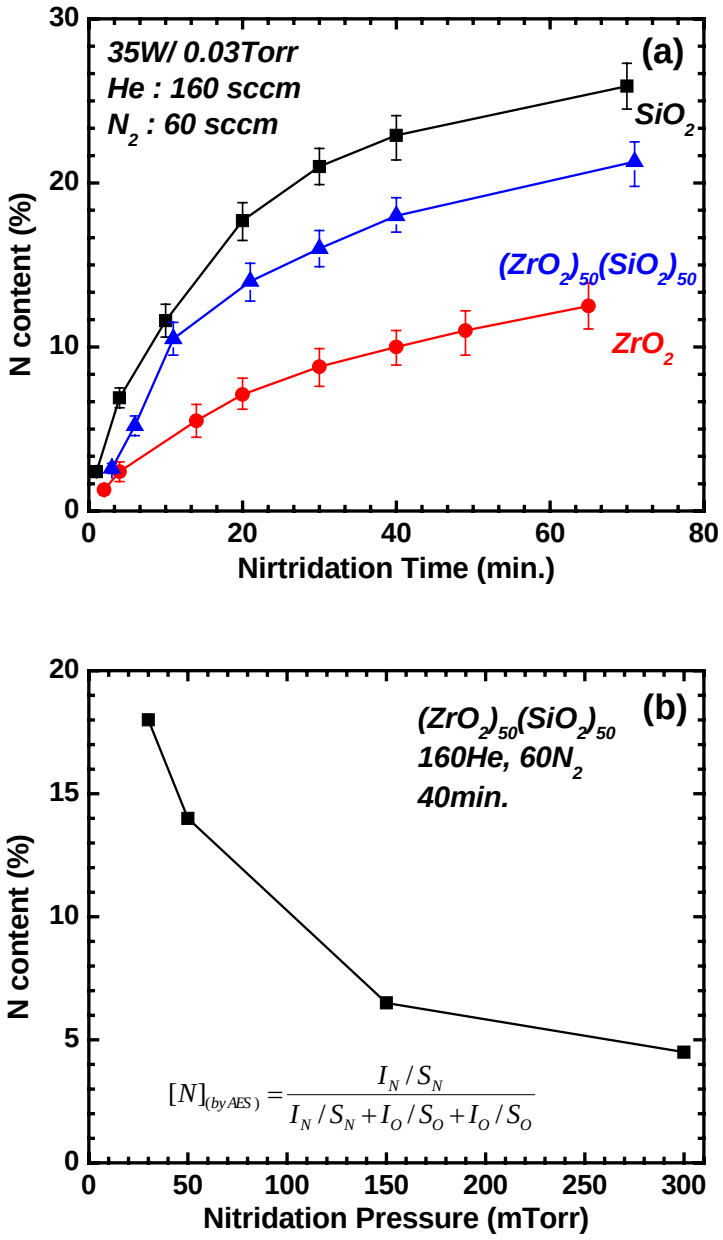

Figure 3.3. (a) The amount of incorporated nitrogen atom in SiO_2, 50% silicate and ZrO_2 films as a function of He/N_2 plasma exposure time and (b) the amount of incorporated nitrogen atoms as a function of plasma nitridation pressure.

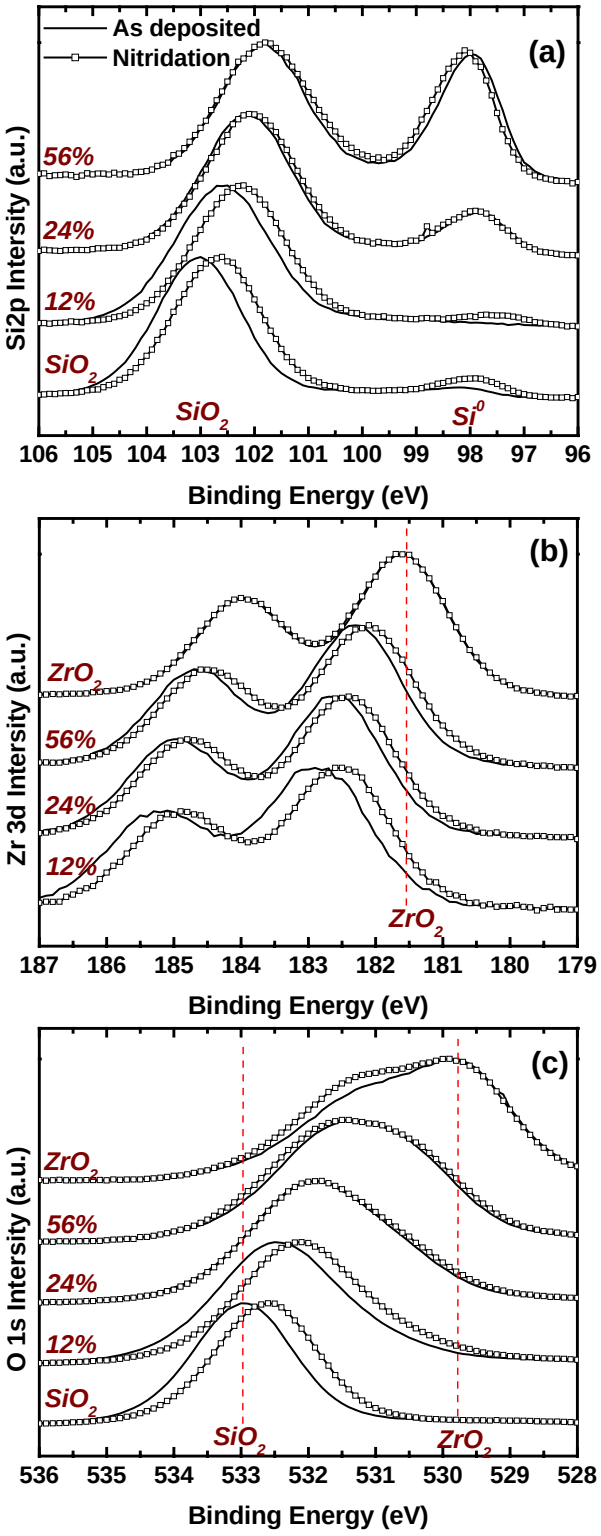

Figure 3.4. XPS core-level (a) Si 2p, (b) Zr 3d, and (c) O 1s spectra of as-deposited Zr silicate films before and after nitridation as a function of silicate composition.

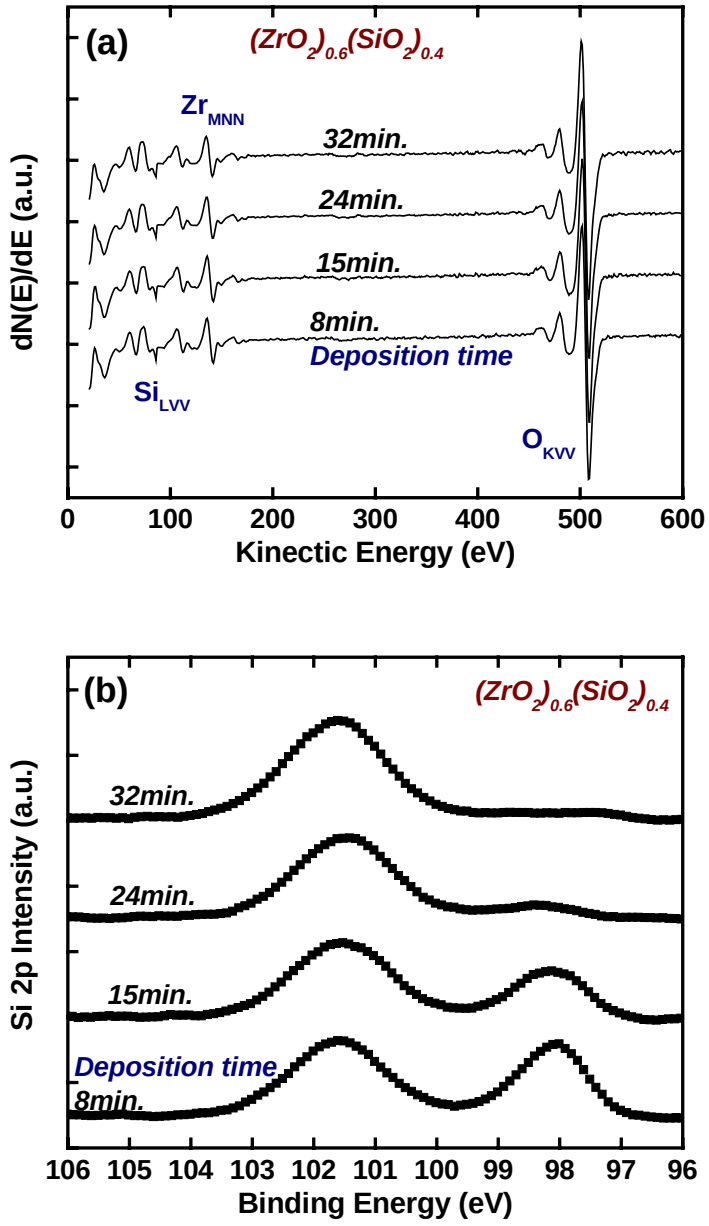

Figure 3.5. (a) Differential AES spectra and (b) XPS core-level Si 2p spectra of as-deposited $(ZrO_2)_{0.6}(SiO_2)_{0.4}$ films by depending on the film thickness.

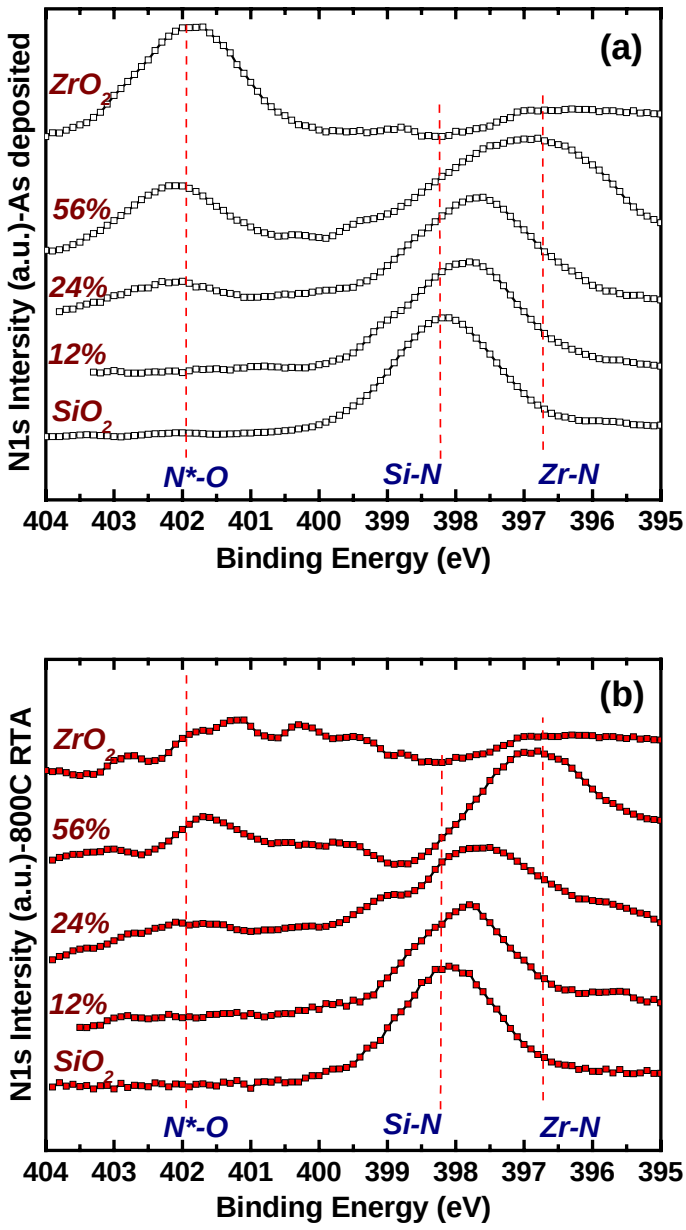

Figure 3.6. XPS core-level N1s spectra as a function of silicate composition after nitridation. (a) As-deposited films and (b) after 800°C RTA

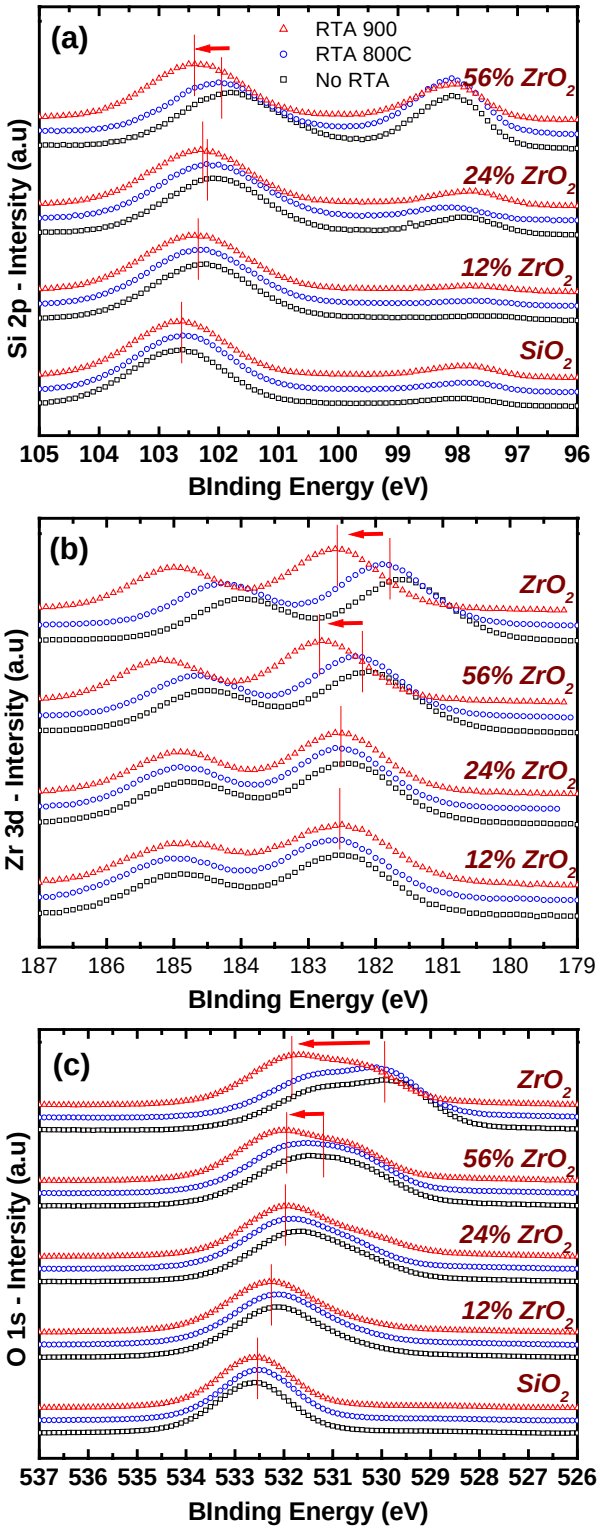

Figure 3.7. XPS core-level (a) Si 2p, (b) Zr 3d, and (c) O 1s spectra of as-deposited Zr silicate films by varying annealing temperature.

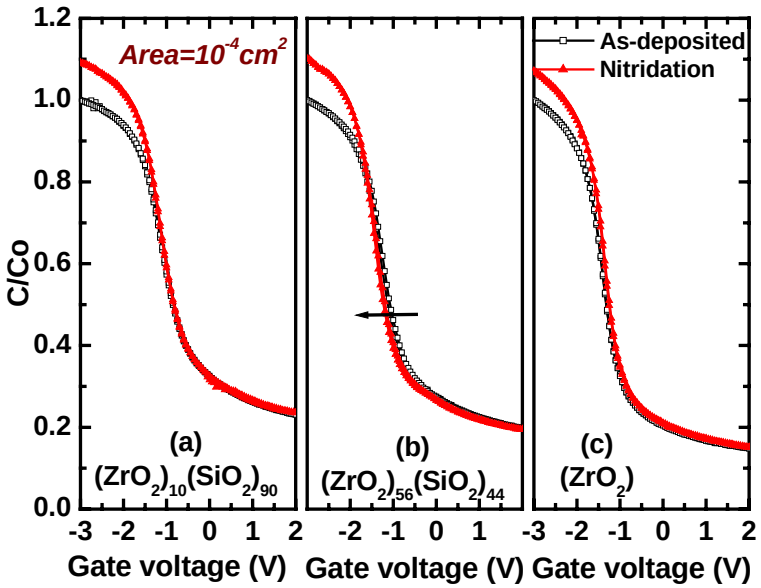

Figure 3.8. C-V characteristics of Al/Zr-silicate/Si substrate structure NMOS capacitor with and without plasma nitridation (a) 10%, (b) 56% silicate, and (c) ZrO_2 films.

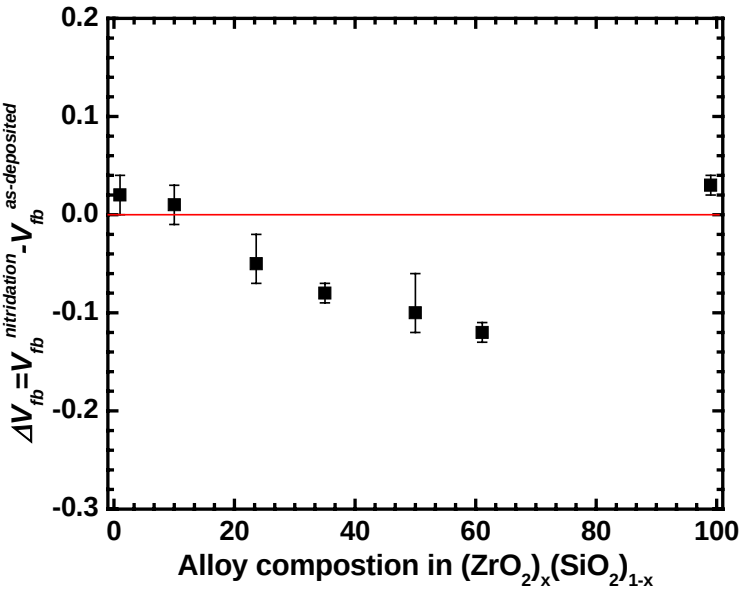

Figure 3.9. Flat-band voltage shifts (ΔV_{fb}) after nitridation as a function of silicate composition. $\Delta V_{fb} = V_{fb}$ *(with nitridation)* $- V_{fb}$ *(without nitridation).*

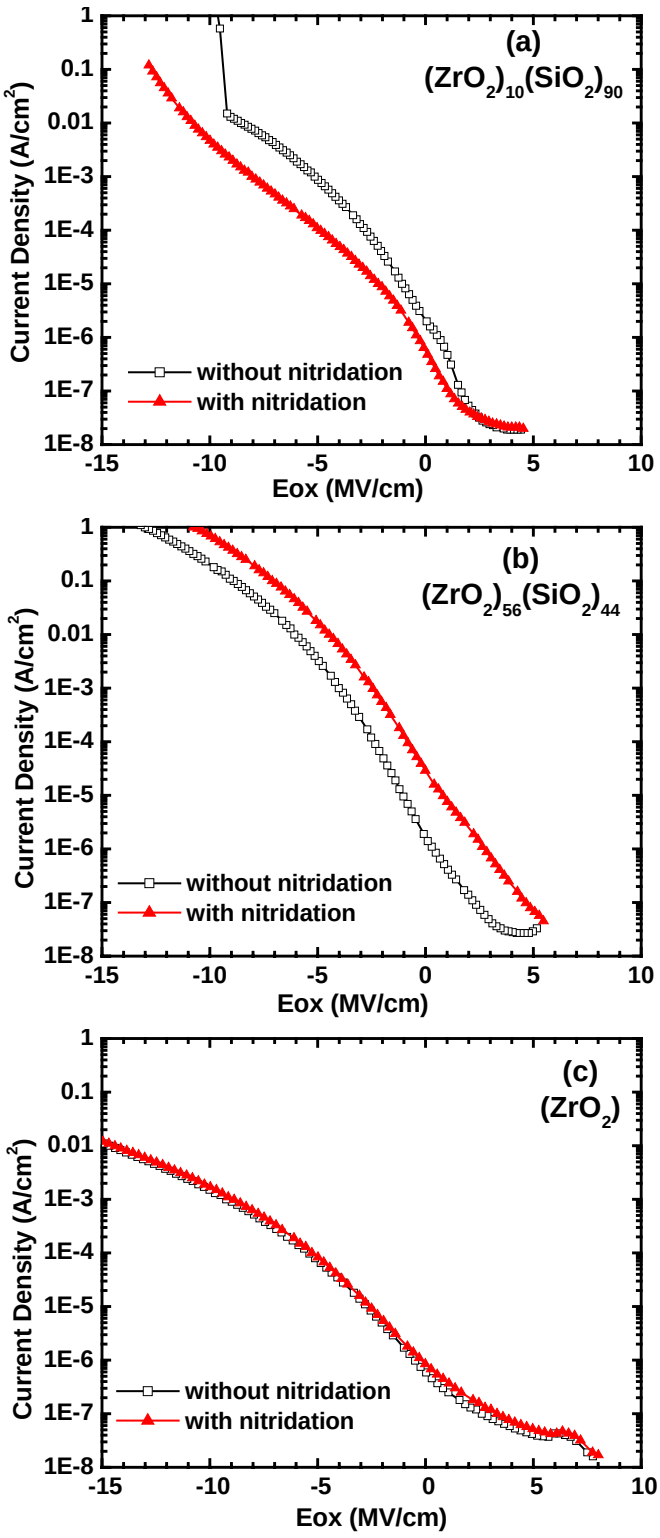

Figure 3.10. J-V characteristics of Al/Zr-silicate/Si substrate structure NMOS capacitor with and without plasma nitridation. (a) 10% silicate, (b) 56% silicate, and (c) ZrO_2.

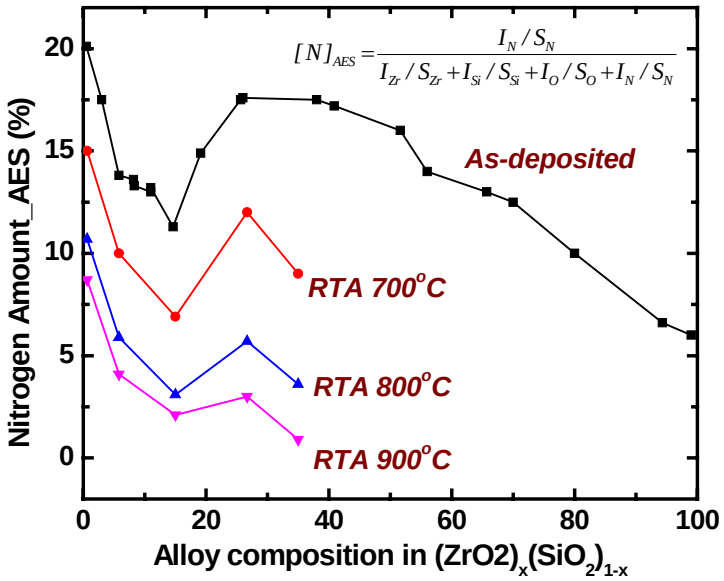

Figure 3.11. The evolution of the incorporated nitrogen atoms as a function of subsequent annealing temperature.

CHAPTER 4. A New Approach to the Synthesis of Zr Oxynitride Alloys: *Chemical and Electrical Characterizations.*

ABSTRACT

In this article, we report that Zr-Si oxynitride films, $(ZrO_2)_x(Si_3N_4)_y(SiO_2)_z$, x+y+z=1, have been deposited using a remote plasma-enhanced chemical vapor deposition (RPECVD) system by putting a Zr source into N_2/N_2O gas mixtures. The films composition was determined by Rutherford back scattering (RBS) that was calibrated by on-line Auger electron spectroscopy (AES) and showed the composition's thermodynamically stable boundary composition in ternary phase diagrams. Zr-Si oxynitride was a pseudo-ternary alloy and no phase separation was detected by x-ray photoelectron spectroscopy (XPS) analysis up to 1100°C annealing. The effect of phase separation on the capacitance-voltage was investigated by fabricating a metal-oxide-semiconductor (MOS) capacitor. The leakage current of Zr-Si oxynitride films showed two different temperature dependent activation energies, 0.02 eV for low temperature and 0.3 eV for high temperature. Poole-Frenkel emission was the dominant leakage mechanism.

4.1 INTRODUCTION

As microelectronic devices are shrunk below 100nm to achieve higher integration, complementary metal-oxide-semiconductor (CMOS) require thinner dielectric films, <2 nm, to maintain the same current levels required for circuit operation [1,2]. However, the conventional gate dielectric films, such as SiO_2 and SiO_xN_y, show their limitations in direct tunneling current density at thickness below 3 nm. Moreover, the priority of leakage current is ranked high in device performance and reliability as portable devices prevail [3,4]. Thus, high-dielectric-constant materials have been widely studied as a candidate to replace the gate dielectric. The requirements [5~8] for these materials are very severe. For example, these materials must have high thermodynamic stability with silicon. Their diffusion coefficients should be low so that these materials can withstand high processing temperatures. For gate oxides, these materials should form high-quality interfaces with silicon with few interfacial defects and low roughness. And these materials are required to have barriers for electrons and holes of at least 1 eV, in order to have sufficiently low leakage current. Recently, HfO_2 [9,10], ZrO_2 [11~13], and their silicates have become attractive candidates because their suitable dielectric constants can effectively reduce the leakage current. Furthermore, these candidates are known for being thermodynamically stable in contact with Si. However, it was reported [14] that phase separation and crystallization often occurred when Hf and Zr silicates were annealed above 900°C. These problems caused a leakage-current increase through the grain boundary, as well as roughness of the film surface created by crystallization. These films

crystallize readily, can be difficult to etch, [15] can react with the Si top electrode, [16,17] and have been shown recently to be susceptible to dopant penetration [18].

One of the other important problems that must be considered when using a poly-Si gate electrode is dopant penetration. The boron-doped p^+ poly Si gate electrode for the p-channel metal-oxide silicon (PMOS) device improves the short-channel effects. However, boron diffusion from the poly Si gate electrode into the channel region through the gate dielectrics can degrade PMOS device performance [19~21]. Therefore, for boron doped p^+ poly-Si gate electrode applications, it is necessary to have a diffusion barrier in the gate oxide to prevent boron penetration into the Si substrate and the channel region. Nitrogen atoms incorporated into the gate dielectric structure are among the candidates for blocking boron diffusion. Nitridation of the top layer of HfO_2 can effectively block boron diffusion [22] and bulk N can help prevent phase separation in Hf and Zr silicate [23,24]. N incorporation into high-k metal oxides may also provide a way to control the flat band shifts by modifying the defect structures in the bulk and at the interface. Because thermodynamics of the Si-O-N system and the kinetics of nitrogen incorporation are rather complex, the different methods of SiON preparation could produce SiON films with different N spatial distributions [25~27] and with different electrical properties, especially in the case of plasma nitridation where active nitrogen species are introduced into the oxide. But our previous results [28] revealed that the incorporated nitrogen atoms break the oxygen atom bonding and (or) can be substituted for the oxygen atom site and make a bond with Zr atoms, as well as Si atoms in the middle-range silicates. So zirconium nitride is known as a metallic conductor that acts as a leakage source in the middle range of silicates. [29,30]

In this article, we report that Zr-Si oxynitride films were deposited by putting a Zr source into an N_2/N_2O gas mixture. Next, the concentration of incorporated nitrogen was measured by on-line Auger electron spectroscopy (AES). Using x-ray photoelectron spectroscopy (XPS) before and after annealing, chemical bonding was also studied. From the spectroscopy results, the effects of the phase separation in dielectric films on the characterization of electrical properties of Zr-Si oxynitride were investigated by capacitance-voltage (C-V) and leakage-voltage (I-V) analysis.

4.2 EXPERIMENTAL PROCEDURES

4.2.1 Si oxynitride and Zr-Si Oxynitride films Deposition and Composition

Using the remote plasma-enhanced chemical vapor deposition (RPEDVD) system, Si oxynitride $[(Si_3N_4)_y(SiO_2)_z]$ and Zr-Si oxynitride $[(ZrO_2)_x(Si_3N_4)_y(SiO_2)_z$, $x + y + z = 1]$ films were deposited on a Si (100) substrate kept at 300°C. The Si and Zr source gases, 2% SiH_4 in He and Zr(IV) t-butoxide, were injected through two different shower-head rings in chamber. The Zr source was contained in a bubbler assembly held at 30°C in a silicone-oil bath. Helium was used as a carrier gas. A 1% nitrous-oxide (N_2O-in-N_2) gas was used for a nitrogen source as well as the oxygen source, since O incorporation is significantly easier in comparison with N incorporation in deposition films. In deposition, Si oxynitride, the total amount of both N_2 and 1% N_2O gas were 200sccm. Therefore, the ZrO_2 and Si_3N_4 composition in Zr-Si oxynitride films was determined by adjusting the bubbler pressure and N_2/N_2O gas ratio, respectively.

Prior to the films' deposition, the Si substrates were dipped in a H_2O/HF (100:1) solution to remove the native oxide and to provide a clean, hydrogen-terminated, Si surface. A mixture of helium and N_2O/N_2 was subjected to remote plasma excitation, (30W at 13.56MHz) and the deposition pressure in the chamber was controlled at 300mtorr. The Zr-Si oxynitride alloy composition was determined by calculating the ZrO_2 and Si_3N_4 percentage, which was obtained from the ratio of intensity of Zr_{MNN} to O_{KVV} and the ratio of N_{KLL} to O_{KVV} measured by an on-line AES. Both peak-height ratios obtained from the derivative curve of AES were also calibrated with Rutherford backscattering (RBS) spectrometry. Figure 4.1 displays these relations between AES peaks ratio and the alloy compositions calculated from RBS.

4.2.2 XPS analysis

Off-line XPS measurements of Si2p, Zr3d, O1s, and N1s core levels were made using a Riber LAS-3000 spectrometer with non-monochromatic Mg Kα radiation (1253.6 eV) and pass energy of 20 eV. The spectral resolution was approximately 1 eV. The system base pressure for XPS measurements was approximately 3×10^{-10}torr. Data were corrected for charging effects using the C1s peak at 284.5 eV for adventitious carbon contamination on the film surface. The repeatability of measuring peak spectral positions was found to be <0.2 eV.

4.2.3 Device Fabrication and Electrical Characterization

Metal-oxide-semiconductor (MOS) capacitors were fabricated to investigate the effects of the films' stabilities and alloy compositions on these films' electrical properties.

The capacitance-voltage was measured by a HP 4284A LCR meter at 1MHz and the current-voltage measurements were performed by a HP 4140B voltage source with a picoammeter. Field-oxide isolation approximately 400 nm thick was made on a Si(100) substrate with carrier density of $>5\times10^{18}cm^{-3}$ (0.02~0.05 Ωcm). The active area was $1\times10^{-4}cm^{2}$. Prior to the films' deposition, remote plasma assisted oxide (RPAO) (SiO_x, $x<2$) of roughly 0.6nm was grown as a buffer layer on top of the silicon silicate. Our previous results [31~33] revealed that this RPAO layer removed carbon contamination from the Si surface and created a device quality Si-SiO_2 interface. The samples were annealed from 900°C to 1100°C (which is the temperature of phase separation and crystallization in a Zr silicate) in an Ar atmosphere for 1min. using an AG Associates minipulse RTA. Forming gas annealing was performed at 400°C for 30min. in a N_2/H_2 gas mixture and followed by Al evaporation ~300 nm thick and defined as a gate electrode. High frequency (1MHz) capacitance-voltage (C-V) and current-density-voltage (J-V) were measured from the room temperature to 200°C to investigate the leakage mechanisms.

4.3 Si OXYNITRIDE, (Si_3N_4)(SiO_2)

4.3.1 Film Deposition.

Figure 4.2(a) shows the evolution of the on-line AES derivative spectra with varying composition of Si oxynitride. The composition could be controlled by the ratio N_2 to N_2O (N_2O-in-N_2) and the relation between gas ration and composition is shown in

Figure 4.2b. A close examination of the spectra revealed a shift in the peak positions of all three features implying a change in the bonding environment around each atom with changing composition. The Si oxynitride composition can be fitted as Eq. 4.1

$$y = 7.5382 \cdot e^{0.013 \cdot x} \quad \text{(Eq. 4.1)}$$

where y is Si_3N_4 percentage in Si oxynitride and x is N_2 gas ratio in N_2/N_2O gas mixture.

Figure 4.3 show the XPS binding energies of Si2p, O1s and N1s core level of as deposited films as a function of Si oxynitride composition and their chemical shift by annealing temperature. The electronegativity of nitrogen (3.04) is smaller than that of oxygen (3.44), so that the binding energy of Si, O and N atom chemically shifts to lower value. The shift (decrease) of O1s binding energy is attributed to the replacement the second neighbor oxygen atoms as the composition goes to Si_3N_4. The binding energies of all elements increased when annealed at 800°C, 900°C and 1000°C as shown in Figure 4.3. The binding energies increment of almost Si oxynitride is approximately 0.5eV, but no binding energy change in its end members, Si_3N_4 and SiO_2, after annealing. The refractive index of Si oxynitride films is observed to slightly decrease following annealing [34]. This is interpreted that Si oxynitride film is slightly oxidation and the as deposited films are meta-stable configurations.

Figure 4.4a and 4.4b display the flat-band voltage vs. EOT as a function of various compositions Si oxynitride and the calculated flat-band voltage at EOT of 3nm and 8nm, respectively. The flat-band voltage of the intermediated oxynitride films became increasingly more negative with respect to the SiO_2 films until 60% of Si

oxynitride. Those results indicated more positive charge existed in the Si oxynitride than in the SiO_2 films and these trends were remarkably clear in the thicker films (8nm). By using the Poisson's equation, fixed charge in the dielectric films was calculated from Eqn. 4.2 and its value was displayed in Figure 4.4b.

$$V_{FB} = \varphi_{ms} - \frac{Q_f}{C_{ox}} = \varphi_{ms} - \left(\frac{qQ_f}{K_{ox}\varepsilon_o}\right)T_{ox} \Rightarrow \ slope = \left(\frac{qQ_f}{K_{ox}\varepsilon_o}\right) \tag{4.2}$$

Fixed charges obtained from Eq. 4.2 in SiO_2 and Si_3N_4 were $8\times10^{11}cm^{-2}$ and $2.3\times10^{12}cm^{-2}$, respectively. Fixed charge of the intermediated oxynitride films also show the same trends like flat band voltage. (i.e. increased remarkably and stayed up to 60% Si oxynitride with respect to the SiO_2, while sharply increased between the 60% Si oxynitride films and the end-member Si_3N_4 composition)

Leakage current densities of several Si oxynitride compositions were displayed in Figure 4.5(a). It was reported [46?]that the increase in physical thickness, as well as the decreases in mass and effective barrier height, predict a minimum value in the current density near the middle of the alloy composition range, bowing of the curves, instead at the nitride end of the alloy. But leakage current densities of Si oxynitride at electric field of 8MV/cm deposited by RPECVD system showed same value up to approximately 60% but rapidly increase in Si_3N_4 side of oxynitride as shown in Figure 4.5(b). The difference between those results is attributed to the films thickness (EOT) and flat band voltage shift (fixed charge). The flat band voltage shifted to negative value in the intermediated oxynitride alloys and more negative value in the end-member Si_3N_4 films as shown in

Figure 4.4(b). So fixed charge showed the same trends by oxynitride composition like flat band voltage. (The amount of fixed charge increase sharply in the end-member Si_3N_4 films.) Therefore, leakage current density of Si_3N_4 films showed larger than that of the middle range of oxynitride alloys in spite of physically thick films in Si_3N_4 alloy. On the other hand, fixed charge and flat band voltage shift of SiO_2 films are small compared to the oxynitride alloy. And the thickness of SiO_2 films was approximately 5nm that leakage current was low enough to compare to oxynitride alloy. So the current density of SiO_2 films is the same value with the middle range of oxynitride alloys as shown in Figure 4.5(b).

4.4 Zr-Si OXYNITRIDE, $(ZrO_2)(Si_3N_4)(SiO_2)$

4.4.1 Zr-Si Oxynitride composition

Figure 4.6 shows the atomic percent concentration ternary diagram of the three respective elements in as-deposited alloys of $(Si_3N_4)(SiO_2)$ and $(ZrO_2)(Si_3N_4)(SiO_2)$ deposited by a remote plasma-enhanced chemical vapor deposition (RPECVD) system. The atomic percentage of the element was obtained from Si_{LVV}, O_{KVV}, and N_{KLL} measured by on-line AES spectra shown in Figure 4.1. It was reported [34] that all of composition of silicon oxynitride films deposited using a N_2/N_2O gas mixture fell approximately on the joint-line between the end members of $(Si_3N_4)(SiO_2)$ alloy as displayed in Figure 4.6. Therefore, the silicon oxynitride alloy composition can then be expressed as a pseudo-binary alloy: $(Si_3N_4)_x(SiO_2)_{1-x}$. The term “pseudo binary” means that alloys are one phase material and their local atomic structures are the same as those

of end members. Therefore, no Si-Si and O-N bonds are detected in a pseudo binary alloy. Like the silicon oxynitride alloy, the Zr-Si oxynitride alloy, $(ZrO_2)(Si_3N_4)(SiO_2)$, shows its own joint-line (or plane) and these alloys' compositions are projected on the Si, O, and N atomic composition diagram, as shown in Figure 4.6, where the perpendicular axis of the atomic ternary diagram is the atomic percentage of Zr. The atomic percentage of all elements in Zr-Si oxynitride alloys also falls on the new joint-line, with one side overlapped with the pseudo binary joint-line at the Si_3N_4 compound. Based on these results, Zr-Si oxynitride alloys can also be designated as a pseudo-ternary alloy. In other words, no Zr-N, Zr-Si, or Si-Si bonds existed in those alloys. These finding is also confirmed by XPS bonding analysis.

Zr source atoms were added into the N_2/N_2O gas mixture for deposition of the silicon oxynitride, and thereby Zr-Si oxynitride was synthesized. Figure 4.7 shows the element's atomic percentage of silicon oxynitride and Zr-Si oxynitride. First, 15%, 25%, 53%, and 66% concentrations of Si oxynitride were deposited at a N_2/N_2O gas ratio at 50/150, 100/100, 150/50, and 180/20 sccm, respectively. Si oxynitride's element compositions were located on the silicon oxynitride joint-line as shown in Figure 4.6. But when the Zr source was added while depositing on silicon oxynitride films and thereby Zr-Si oxynitride films, its element atomic percentage deviated from the joint-line of the silicon oxynitride and merged onto the joint-plane of Zr-Si oxynitride. Moreover, the element percentage of Zr-Si oxynitride moved along the joint-plane when the amount of Zr source was increased, as shown in Figure 4.7(a). The atomic percentage of Zr-Si oxynitride films also can be converted into a ternary alloy diagram; its corners are SiO_2, Si_3N_4, and ZrO_2, as shown in Figure 4.7(b). The composition of ternary alloy films was

determined by calibrating both the peak ratio of Zr_{MNN} to O_{KVV} and the peak ratio of N_{KLL} to O_{KVV} obtained from on-line AES with composition calculated by Rutherford back scattering (RBS). Ternary alloy composition by increasing the ZrO_2 amount showed characteristic behavior between the SiO_2-rich alloy and the Si_3N_4-rich alloy. In SiO_2-rich alloys, adding the Zr source to ternary alloy compositions relatively sustained the amount of Si_3N_4 by adding Zr source and thereafter abruptly decreased Si_3N_4. Thereafter, increasing the amount of ZrO_2 compound abruptly decreased the Si_3N_4 ratio.

However, in Si_3N_4-rich alloy, the ratio of Si_3N_4 to SiO_2 was maintained up to approximately 25% ZrO_2 and then the Si_3N_4 ratio decreased, as shown in the SiO_2-rich region. From these ternary alloy composition behaviors, Zr-Si oxynitride film composition deposited in RPECVD system showed its boundary, as shown in Figure 4.8. As demonstrated in Figure 4.7(b), ZrO_2 percentage in Zr-Si oxynitride cannot exceed more than approximately 60%; i.e. "*forbidden composition*". Another forbidden composition also appeared in the SiO_2 corner. These results are in good agreement with or almost the same trend as the nitrogen percent shown in plasma nitridation of $(ZrO_2)_x(SiO_2)_{1-x}$ alloy. It is revealed at Chapter 3 that the incorporated nitrogen in Zr silicate alloys showed its local minimum at the SiO_2-rich silicate ($x<0.3$) and local maximum at 50% silicate due to exposure in He/N_2 plasma. In addition, no nitrogen atoms were detected in ZrO_2 films after plasma nitridation. The average O atom coordination increased from twofold in SiO_2 to threefold in 50% silicate, and thereafter to fourfold in ZrO_2. It is thought that the Si atom in the forbidden composition near the SiO_2 alloy made a relative stable bond with the oxygen atom, so that the nitrogen atom cannot find the Si atom with which to bond. The other forbidden composition in the ZrO_2-rich

alloy also showed the same trends, such as the silicon atom shortage. Based on the bonding model, the SiO_2-rich alloy is composed of a modified α-SiO_2 crn with terminal $Si\text{-}O^{1-}$ bonds and Zr^{4+} ions, while ZrO_2-rich alloy is formed of ionic oxide made up of O^{2-}, $Si\text{-}O_4^{4-}$, and Zr^{4+} ions. So nitrogen atom easily made a bond with a silicon atom in the middle range of the silicate, compared to the bonding in the forbidden composition.

4.4.2 XPS Binding Energies with Alloy Composition

Figure 4.9 show the XPS binding energy of the Si2p and Zr3d core level of Zr-Si oxynitride with $(ZrO_2)_{0.5}(SiO_2)_{0.5}$ silicate alloy as a function of Si_3N_4 amounts of 33%, 47%, and 58%. The spectra represent as-deposited films annealed at 1000°C and 1100°C in an Ar ambient for 1 min. The films were deposited about 15 nm, which is enough thickness to detect chemical phase separation into ZrO_2 and SiO_2 phases. As mentioned previously, Zr-Si oxynitride films are pseudo-ternary alloy, which mean that a nitrogen atom made a bond with only silicon and oxygen atoms. (no Zr-N bond). So as the amount of Si_3N_4 increased, the binding energy of Si2p and Zr3d decreased. Since the Pauling electronegativity of N atom (3.04) is smaller than that of O (3.44) atoms, the valence electron of each atom will move farther from the nuclei by increasing the amount of nitrogen atoms, which decreases the binding energy for the core electron. However, the binding energy of Si2p and Zr3d increased slightly when the Zr-Si oxynitride films were annealed as shown in Figure 4.9. This incremental increase is attributed to relaxation of the bonding network in films. Our group's previous infrared (IR) spectrum results [14] revealed that a 50% Zr silicate bonding network was disrupted completely when all oxygen atoms had a three-fold coordination, where one bonding is connected to one Si

atom (SiO^{+4}) and two bondings are to Zr^{4+} ions. And it is also well known that ~50% Zr silicate alloy separated into SiO_2- and ZrO_2-rich phases and crystallized when annealed above 900°C. XPS analysis is the most useful tool for detecting the phase separation by measuring the O1s binding energy.

4.4.3 Thermal Stability of Zr-Si Oxynitride alloy

Figure 4.10 displays core level spectra of O1s and its derivative spectra for as-deposited and annealed at 1000°C and 1100°C. The binding energy peak position is at ~531.9eV, which is between SiO_2 (532.7eV) and ZrO_2 (530.1eV), and there is no evidence of a chemical phase separation in the Zr-Si oxynitride alloy by annealing. In addition, there was no chemical shift during the annealing up to 1100°C. These results indicate that Zr-Si oxynitride alloy is thermally stable during subsequent annealing. The phase separation or crystallization in gate-dielectric films causes the increase of leakage current and degradation of reliability of the insulator because of the grain boundary formation and surface roughness. Because suppressing chemical phase separation and archiving thermal stability with silicon is a necessary consideration in gate-dielectric films' properties, Zr-Si oxynitride is considered as an alternative for a conventional SiO_2 dielectric. Moreover, nitridation of the dielectric films can effectively prevent boron diffusion and improve the reliability when using polycrystalline silicon (p^+ Si) as the gate electrode. Nitrogen incorporation into high-k dielectric films may also provide a way to control the flat band shifts by modifying the defect structures in the bulk and at the interface [23,35,36]. Plasma nitridation is one way to incorporate nitrogen, but our previous results [28] with XPS analysis revealed that nitrogen atoms incorporated by

plasma nitridation replaced existing oxygen atoms and thereby made a bond with the Zr atom, as well as with Si atoms in the middle range (~50%) of the Zr silicate. Since zirconium nitride (ZrN) is known as a metallic conductor [29,30] that is supposed to act as a leakage source in a gate dielectric, the middle range of Zr silicates (~50%) with nitridation showed higher leakage current density than that of the same composition silicate without nitridation. And because incorporated nitrogen using plasma nitridation was structurally unstable, the amount of nitrogen diffused out annealing. In contrast to the plasma nitridation, nitrogen atoms in Zr-Si oxynitride films show no bonding with Zr atoms as shown in Figure 4.11(a), and the relative amounts of nitrogen calculated from the XPS area are maintained even after annealing as shown in Figure 4.11(b). The binding energies of Zr-Si oxynitride measured by XPS are listed in Table 1.

4.4.4 Effect of Phase Separation on MOS Capacitance

Based on the Zr-Si oxynitride films' thermal stability characteristics, the effects of phase separation on the electrical properties were investigated by fabricating the MOS capacitor for both Zr silicate and Zr-Si oxynitride dielectric films with an Al electrode. Figure 4.12 shows the C-V characteristics of various compositions of Zr silicate and equivalent-oxide thickness (EOT) change as a function of annealing from 700°C to 1000°C in Ar ambient for 1 min. In order to compare the electrical properties, the capacitances were normalized to the 700°C accumulation region. The accumulation capacitance decreased as the annealing temperature increased in all compositions as shown in Figure 4.12(a). These increases are attributed to the formation of the SiO_2 layer between the dielectric and silicon substrate with increasing annealing temperatures. ZrO_2

and Al_2O_3 films are a poor diffusion barrier against oxygen atoms and have the catalytic effect [37~39] that encourage the growth of the interfacial oxide layers. So the growth of the interfacial oxide layer is due to the oxidation of the substrate oxide by the diffusion of oxidizing species from the ambient throuth the dielectric films. Silmilar results were observed in CeO_2 and Y_2O_3 [40,41] films deposited on Si substrates. In addition, silicon atoms that diffused from the substrate to the films caused deterioration of the k value of the gate dielectric by changing the composition. It was reported [42] that the as-deposited films are hydrogenated suboxides and are chemically random-ordered alloys with statistically determined bonding of Si and O atoms by infrared (IR) analysis. But that article did not investigate the interface character by annealing. As previously mentioned, the middle range of Zr silicate alloys separated into SiO_2-rich and ZrO_2-rich alloy when annealed at 900°C, so this separation of the composition silicate caused a remarkable increment of EOT, as shown in Figure 4.12(b). It is possible to assume that the silicate lost its character as a high-k dielectric due to a mixture of SiO_2-rich and ZrO_2-rich alloys. This increment was retarded when annealed at 1000°C because the created SiO_2 blocked the further diffusion of the silicon atoms. In addition to the remarkable EOT increment due to the phase separation, the flat band also shifted to negative because of the phase separation. Figure 4.13 displays the C-V curves of the Zr-Si oxynitride films and the EOT change as a function of the amount of Si_3N_4 in the Zr-Si oxynitride. As mentioned above, the EOT of ~50% silicate increased abruptly at 900°C annealing, whereas there was no significant increment of EOT throughout the annealing temperature in Zr-Si oxynitride and no flat-band voltage shifts. And the increment was reduced as the amount of Si_3N_4 was increased as shown in Figure 4.13(b). The formation of the SiO_2 interfacial layer

resulted in the slight increment in the Zr-Si oxynitride. This indicated that no chemical phase separation occurred in Zr-Si oxynitride films.

4.4.5 Leakage Current Mechanism of Zr-Si Oxynitride

Figure 4.14(a) shows the C-V dependence on the measuring temperature for the Zr-Si oxynitride and their EOT and hysteresis in Figure 4.14b. The EOT maintained its value, ~2.6 nm, up to 175°C and slightly increased to 3 nm at 200°C. The hysteresis also sustained 30mV and abruptly increased after 150°C. In addition, flat-band voltage shifted to a more positive direction as the measuring temperature increased to 200°C (not shown here). The flat-band voltage shifts to a positive direction can be caused by the charge compensation in the dielectric as the measuring temperature increased.

Over the same measuring temperature range, the J-V dependence is displayed in Figure 4.15(a). No significant changes in leakage current were observed up to 75°C, and thereafter the leakage current increased remarkably from the measuring temperature at 100°C. Under substrate injection, the current relatively depends on temperature for low electric field, and the current is much less dependent on temperature. Electrons are tunneling through the SiO_x interfacial layer and arrive at Zr-Si oxynitride films where defects occupy energy levels near the conduction band edge of the films. Consequently, defects take part in the conduction mechanism. On the other hand, under gate injection, the current depends weakly on temperature, over most of the gate voltage range [43]. So, as shown in Figure 4.15(b), the leakage current shows two different activation energies depending on the measuring temperature. It is reported [44,45] that the temperature dependence of the leakage current through dielectric films depending on both the carrier

excitation (such as trap release) and transport mechanisms and that both of these have temperature dependence. Also, the activation energy for bulk mobility is smaller than that for trap release. The activation energies calculated from temperature dependence are related to the conduction band offset between silicon substrate and dielectric films. The leakage current is independent of the measuring temperature at relatively low temperature (up to 75°C), whereas the leakage current depends strongly on the temperature as shown in Figure 4.15(b). The activation energy was 0.03eV at the low measuring temperature, i.e., electrons cannot be trapped by the trapping centers. On the other hand, the activation energy was higher (0.3eV) at the high measuring temperature. In this case, the Poole-Frenkel mechanism becomes the dominant leakage current mechanism, and the electrons flowing through the structure is strongly dependent on temperature [47]. Consequently, the strong temperature dependence of the current can be attributed to the P-F mechanism in the Zr-Si oxynitride films.

In order to examine the leakage current mechanism, J/E^2 vs.1/E for Fowler-Nordheim (F-N) and J/E vs. $E^{1/2}$ for Poole-Frenkel (P-F) tunneling were plotted as shown in Figure 4.16. The F-N curves show a relatively linear relation at low temperature but a deviation from the linearity (F-N tunneling mechanism) apparently increases as the measuring temperature increases. However, the P-F emission shows remarkable linearities throughout the entire measuring temperature. This confirms that Poole-Frenkel emission is the dominant leakage mechanism in Zr-Si oxynitride films.

4.4 CONCLUSION

The experimental results show Zr-Si oxynitride films were deposited using the N_2/N_2O gas mixture in a RPECVD system. Like the silicon oxynitride films, the composition of the Zr-Si oxynitride alloy fell onto its own joint-line (or plane), with one side overlapped with the pseudo binary joint-line at the Si_3N_4 compound. So the Zr-Si oxynitride films can be considered pseudo-ternary alloys with no Zr-N, Zr-Si, and Si-Si, bonds. Because the atomic percentage of films can be converted into a ternary alloy diagram that can be calibrated with RBS, there are forbidden composition in ZrO_2 rich alloy and SiO_2 rich alloy. These forbidden composition are in good agreement with the nitrogen amount incorporated by plasma nitridation of $(ZrO_2)_x(SiO_2)_{1-x}$ alloy.

The stability of the Zr-Si oxynitride alloy was investigated by XPS analysis. Zr-Si oxynitride film is stable up to 1100°C annealing and no chemical phase separations or crystallization was detected by analysis of the core level binding energy of the oxygen atom. In contrast to the plasma nitridation, nitrogen atoms in Zr-Si oxynitride films show no bonding with Zr atoms (zirconium nitride bonding) and the relative amounts of nitrogen calculated from the XPS area are maintained even after annealing.

The analysis of the C-V data indicates that the EOT increases linearly in SiO_2-rich and ZrO_2-rich silicate by increasing annealing temperature up to 1100°C, those increments result from the formation of the SiO_2 layer between the dielectric and the silicon substrate. Whereas the EOT of the middle range of silicate increased remarkably when annealed at 900°C, this result is attributed to the phase separation, as well as the formation interface. However, Zr-Si oxynitride films show no dramatic EOT increase from annealing and the increment is reduced as the Si_3N_4 amount increases. The leakage current of Zr-Si oxynitride film shows two different activation energies depending on the

measuring temperature, such as 0.03eV at low temperature and 0.30eV at high temperature. In addition, Poole-Frenkel emission is the dominant leakage mechanism in Zr-Si oxynitride films.

4.5 REFERENCES

[1] T.Hori and H.Iwasaki, IEEE Electron Device Lett. **10,** 195 (1989).

[2] M. Bhat, L. K. Han, D. Wristers, J. Yan, D. L. Kwong and J. Fulford, Appl. Phys. Lett. **66**, 1225 (1995)

[3] D.A. Buchanan, E.P. Gusev, E. Cartier, H. Okorn-Schmidt, K. Rim, M.A. Gribelyuk, A. Mocuta, A. Ajmera, M. Copel, S. Guha, N. Bojarczuk, A. Callegari, C. D. Emic, P. Kozlowski, K. Chen, R.J. Fleming, P.C. Jamison, J. Browin, and R. Ardnt, Tech. Dig. Int. Electron Device Meet., 223 (2000)

[4] C.Hu, IEDM, 319 (1996)

[5] P.Zurcher et al., Mater. Res. Soc. Symp. Proc. **541**, 11 (1999)

[6] A.Gril et al., Mater. Res. Soc. Symp. Proc. **541**, 89 (1999)

[7] H.J.Hubbard and D.G.Schlom, J. Mater. Res. **11**, 2757 (1996)

[8] J.Robertson et al, J.Vac.Sci.Technol. B **18**, (2000)

[9] J.Aarik, A.Aidla, A.A.Kiisler, T.Uustare, and V.Sammelselg, Thin Solid Films **340**, 110 (1999)

[10] B.H.Lee, L.Kang, W.-J.Qi, R.Nieh, Y.Jeon, K.Onish, and J.Lee, IEDM Tech.Dig. **166,** (1999)

[11] A.S.Kao, J.Appl.Phys. **69**, 3309 (1991)

[12] W.J.Qi, R.Nieh, B.H.Lee, L.Kang, Y.Jeon, K.Onish, T.Ngai, S.Banergee, and J.C.Lee, IEDM Tech.Dig. **145,** (1999)

[13] M.Copell, M.Gribelyuk, and E.Gusev, Appl.Phys.Lett. **76**, 436 (2000)

[14] G.B.Rayner,Jr., D.Kang, Y.Zhang, and G.Lucovsky, J.Vac.Sci.Technol. B **20**, 1748 (2002)

[15] J.J.Chambers, A.L.P.Rotondaro, M.J.Bevan, M.R.Visokay, and L.Colombo, Electrochem. Soc. Proc. **26**, 359 (2002)

[16] C.H.Lee, H.F.Luan, W.P.Bai, S.J.Lee, T.S.Jeon, Y.Senzaki, D.Roberts, and D.L.Kwong, Int. Electron Devices Meet. **2000**, 31 (2000)

[17] T.Ma, S.A.Campbell, R.Smith, N.Hoilien, B.He, W.L.Gladfelter, C.Hobbs, D.Buchanan, C.Taylor, M.Gribelyuk, M.Tiner, M.Coppel, and J.J.Lee, IEEE Trans. Electron Devices **48**, 2348 (2001)

[18] K.Onishi, L.Kang, R.Choi, E.Dhamarajan, S.Gopalan, Y.Jeon, C.S.Kang, B.H.Lee, R.Nieh, and J.C.Lee, Symposium on VLSI Tech. Digest of Tech. Papers, 131 (2001)

[19] K.S.Krisch, L.Manchanda, F.H.Baumann, M.L.Green, D.Brasen, L.C.Feldman and A.Ourmazd, IEDM Tech. Dig., 325 (1994)

[20J.Y.C.Sun, C.Wong, Y.Taur and C.H.Hsu, 1989 Symp. VLSI. VLSI Tech.Dig., 17 (1989)

[21] J.R.Pfiester, F.K.Baker, T.C.Mele, H.H.Tseng, P.J.Tobin, J.D.Hayden, J.W.Miller, C.D.Gunderson and L.C.Parrillo, IEEE Trans.Electron Devices, **37**, 1842 (1990)

[22] H.J.Cho, C.S.Kang, K.Onishi, S.Gopalan, R.Nieh, R.Choi, S.Krishnan, and J.C.Lee, IEEE Electron Device Lett. **23**, 249 (2002)

[23] M.R.Visokay, J.J.Chambers, A.L.P.Rotondaro, A.Shanware, and L.Colombo, Appl. Phys. Lett. **80**, 3183 (2002)

[24] D.Niu, R.W.Ashcraft, C.Hinkle, and G.N.Parsons J.Vac.Sci.Technol, A **22**, 445 (2004)

[25] M.L.Green, E.P.Gusev, R.Degraeve, E.L.Garfunkel, J.Appl.Phys., **90**, 2057 (2001)

[26] A.Khandelwal, B.C.Smith, H.H.Lamb, J.Appl.Phys., **90** (6), 3100 (2001)

[27] A.Raveh, J.Brewer, E.A.Irene, J.Vac.Sci.Technol., A **17** (2001)

[28] B.Ju and G.Lucovsky (unpublished)

[29] R.Nieh, C.S.Kang, H.J.Cho, K.Onishi, R.Choi, S.Krishnan, J.H.Han, Y.H.Kim, M.S.Akbar and J.Lee, IEEE Trans. Electron Device, **50**, 333 (2003)

[30] I.Milosev, H.H. Strehblow, B.Navinsek and P.Panjan, Surface Science Spectra, **5**, 152 (1998)

[31] H.Niimi and G.Lucovsky, J.Vac.Sci.Technol, B **17**, 2610 (1999)

[32] T.Yasuda, Y.Ma, S.Habermehl and G.Lucovsky, Appl. Phys. Lett., **60**,434 (1992)

[33] M.L.Green, SRC Topical Res.Conf. On Critical Issues for Gate Dielectric Integration, Raleigh, 1994.

[34] S.V.Hattangady, H.Niimi, and G.Lucovsky, J.Vac.Sci.Technol. A **14**, 3017 (1996)

[35] D.G.Park, H.J.Cho, I.S.Yeo, J.S.Roh, and J.M.Hwang, Appl. Phys. Lett, **77**, 2207 (2000)

[36] R.Sharma, D.Naedele, and E.Schweda, Chem.Mater. **13**, 4014 (2001)

[37] W.J.Qi, R.Nieh, B.H.Lee, L.Kang, Y.Jeon, and J.C.Lee, Appl. Phys. Lett. **77**, 3269 (2000)

[38] H.Watanabe, Appl.Phys.Lett. **78**, 3803 (2001)

[39] S.Jeon, H.Yang, H.S.Chang, D.G.Park, and H,Hwang, J. Vac. Sci. Techonol. B **20** (3) (2002)

[40] G.B.Alers, R.M.Fleming, Y.H.Wong, B.Dennis, A.Pinzuk, G.Redinbo, R.Urdahl, E.Ong, and Z.Hasan, Appl. Phys. Lett. **72**, 1308 (1998)

[41] S.K.Kang, D.H.Ko, E.H.Kim, M.H.Cho, and C.N.Whang, Thin Solid Films **353**, 8 (1999)

[42] G.Lucovsky, A.Banerjee, B.Hinds, B.Claflin, K.Koh, and H.Yang, J. Vac. Sci.Technol. B **15**, 112 (1997)

[43] Xu Z, Houssa M, De Gendt S and Heyns M M 2002 Appl. Phys. Lett. **80** (1975)

[44] W.C.Johnson, "Study of Electronic Transport and Breakdown in Thin Insulating Films," Tech. Rep.No.7, Princeton University, (1979)

[45] K.J.Hubbard and D.G.Schlom, J.Mater.Res. **11**, 2757 (1996)

[46] Sze S M 1981 Physics of Semiconductor Devices (New York: Wiley)

[47] De Salve B, Ghibaudo G, Pananakakis G, Guillaumot G and Reimbold G, J. Appl. Phys., **86**, 2751 (1999)

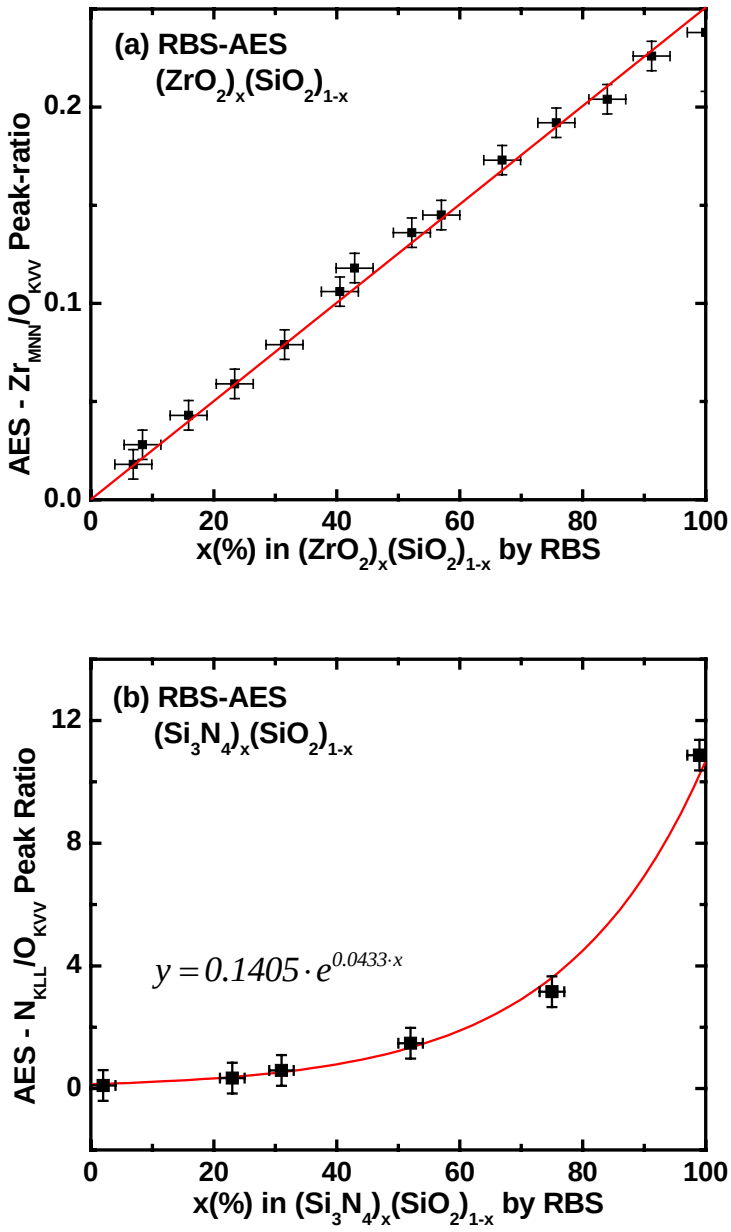

Figure 4.1. Relation between AES peaks ratio and alloy composition calculated from RBS studies. (a) The ratio Zr_{MNN}/O_{KVV} vs. alloy compositions from RBS [14] and (b) the ratio N_{KLL}/O_{KVV} vs. alloy compositions from RBS.

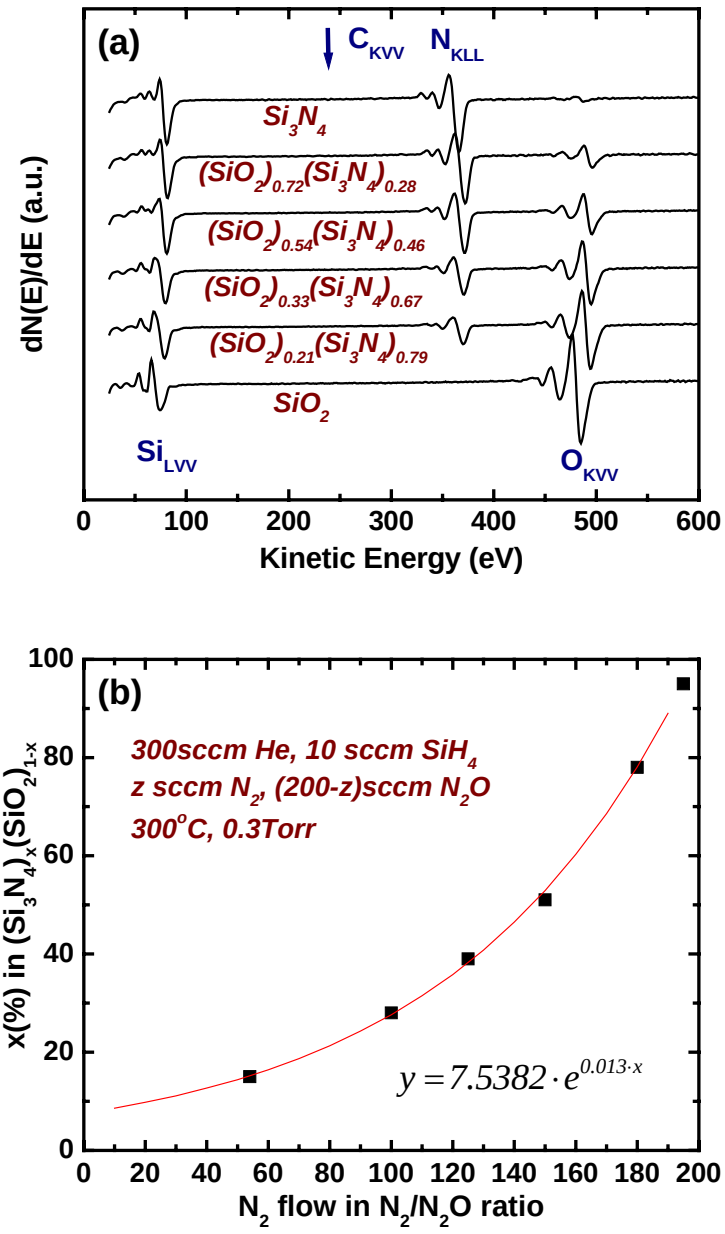

Figure 4.2. (a) The on-line AES derivative spectra from RPECVD SiO_xN_y films using N_2/N_2O gas mixture and (b) composition of SiO_xN_y films as a function of N_2 flow rate in N_2/N_2O gas mixture.

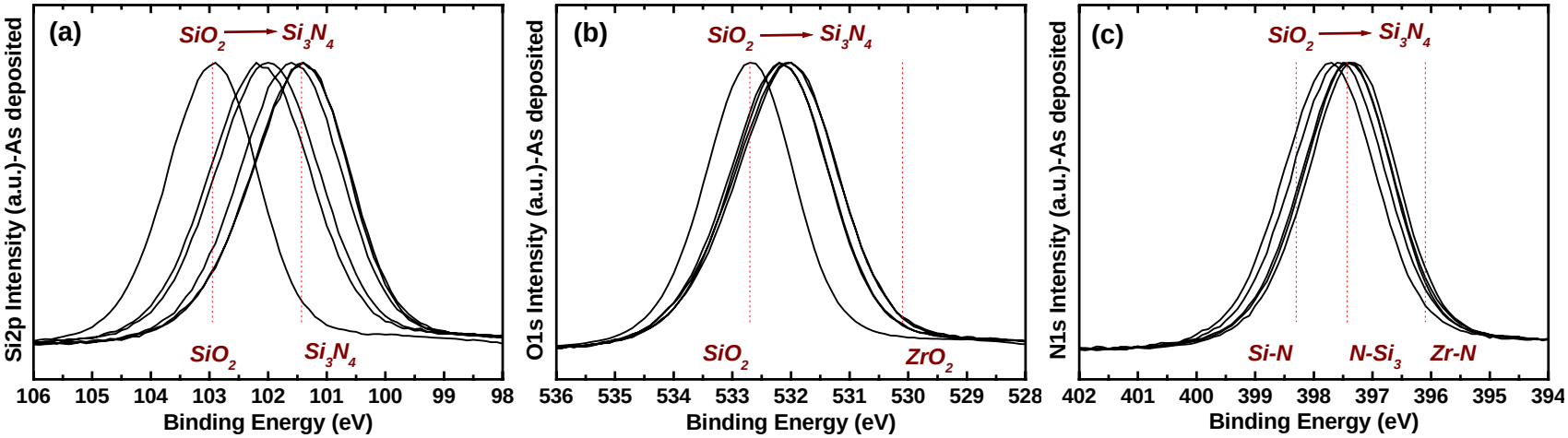

Figure 4.3. XPS core-level (a) Si2p, (b) O1s and (c) N1s spectra of as-deposited silicon oxynitride films as a function of composition.

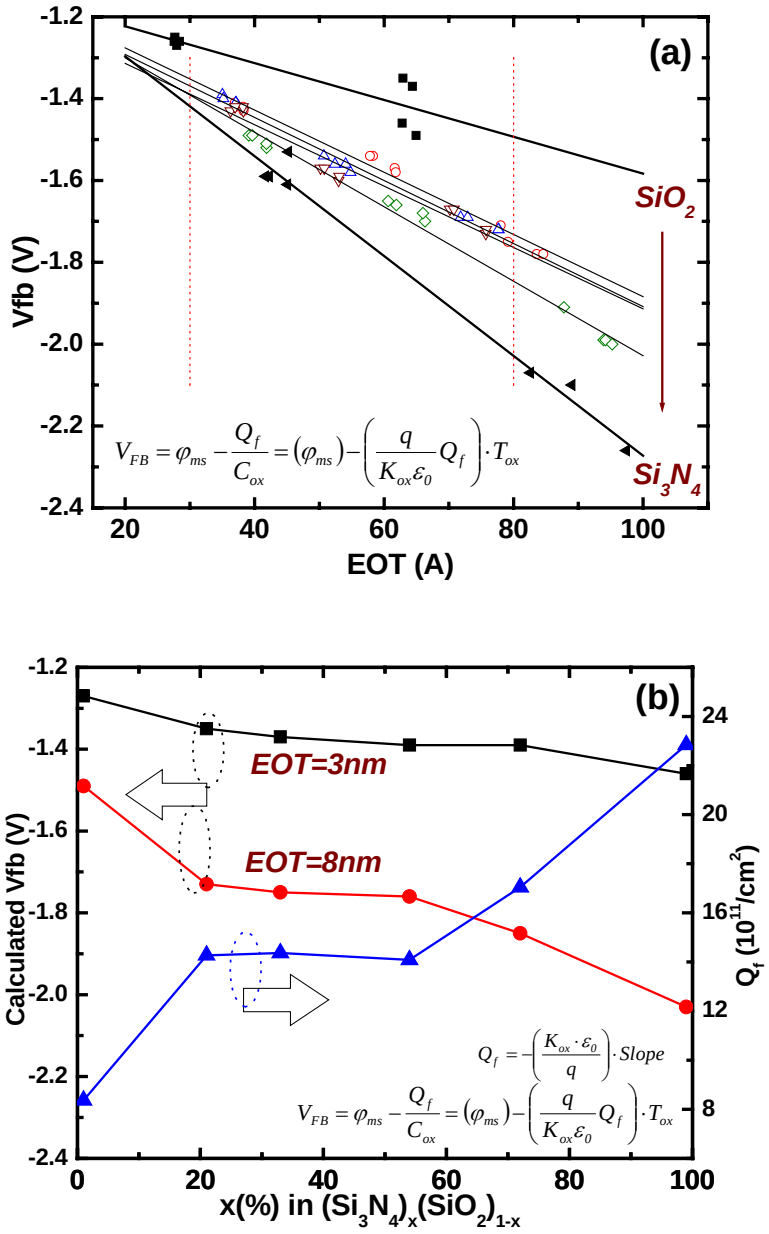

Figure 4.4. (a) Flat band voltage shift as a function of EOT of silicon oxynitride and (b) calculated flat band voltage at EOT 3nm and 8nm as a function of silicon oxynitride composition.

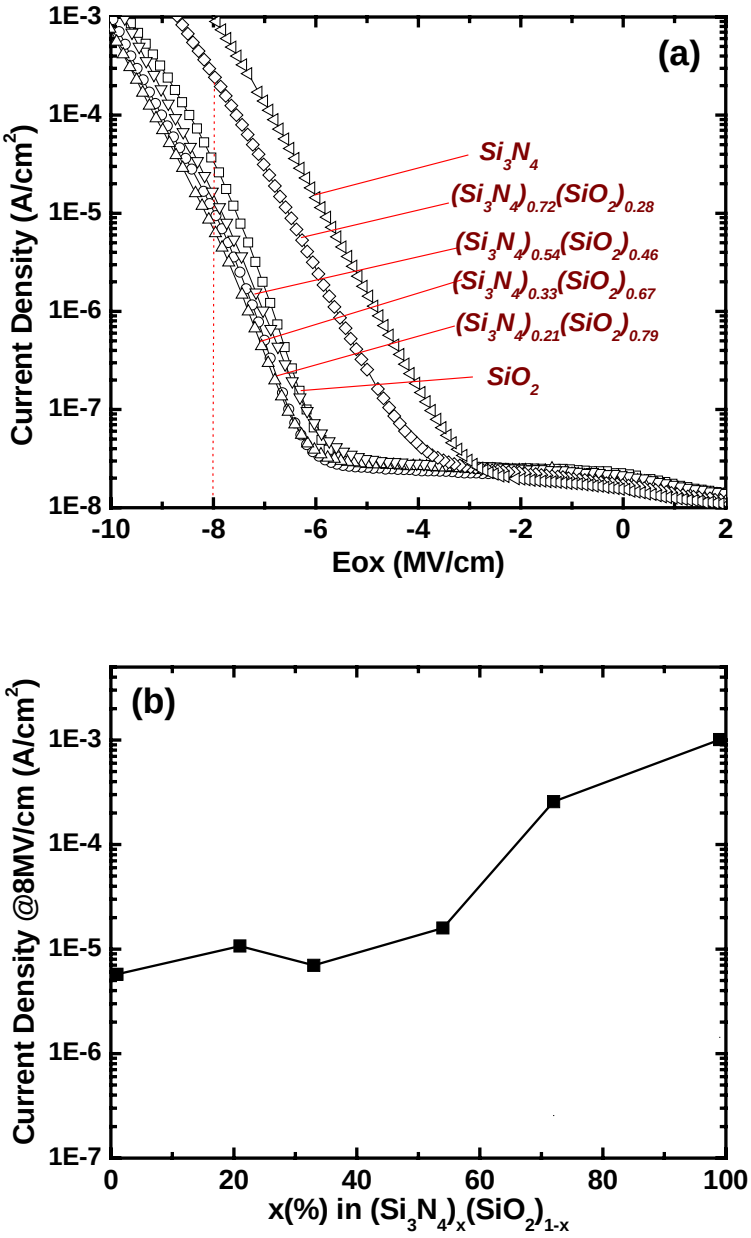

Figure 4.5. (a) Leakage current density of various Si oxynitride compositions as a function of electric field and (b) leakage current density at 8MV/cm as a function of Si oxynitride composition.

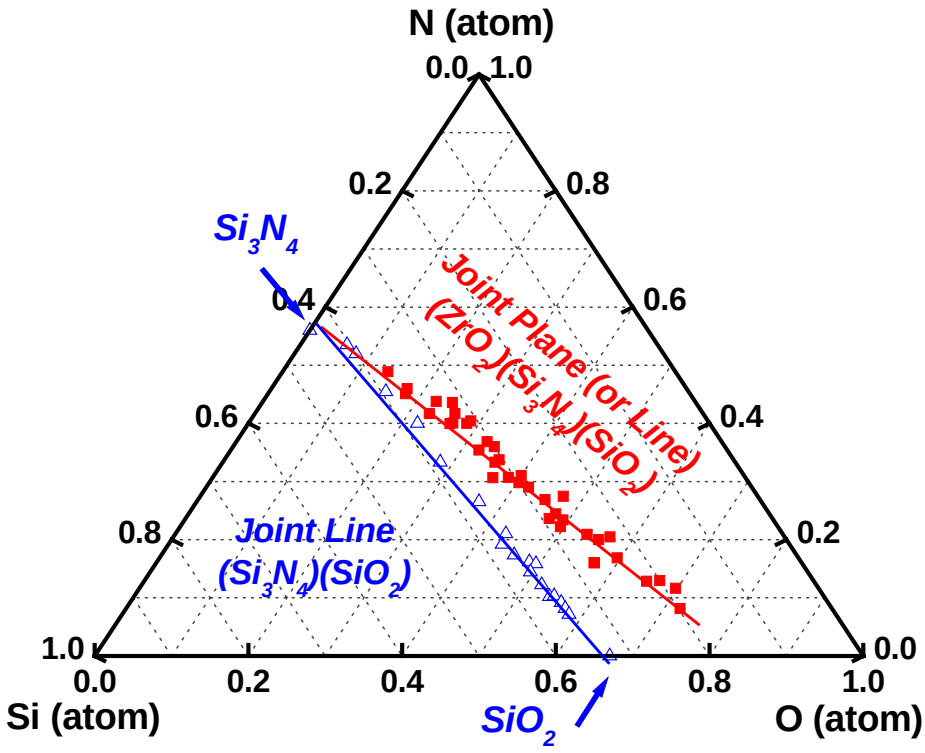

Figure 4.6. The atomic percent concentration ternary diagram of the three respective elements in as-deposited alloys of $(Si_3N_4)(SiO_2)$ and $(ZrO_2)(Si_3N_4)(SiO_2)$.

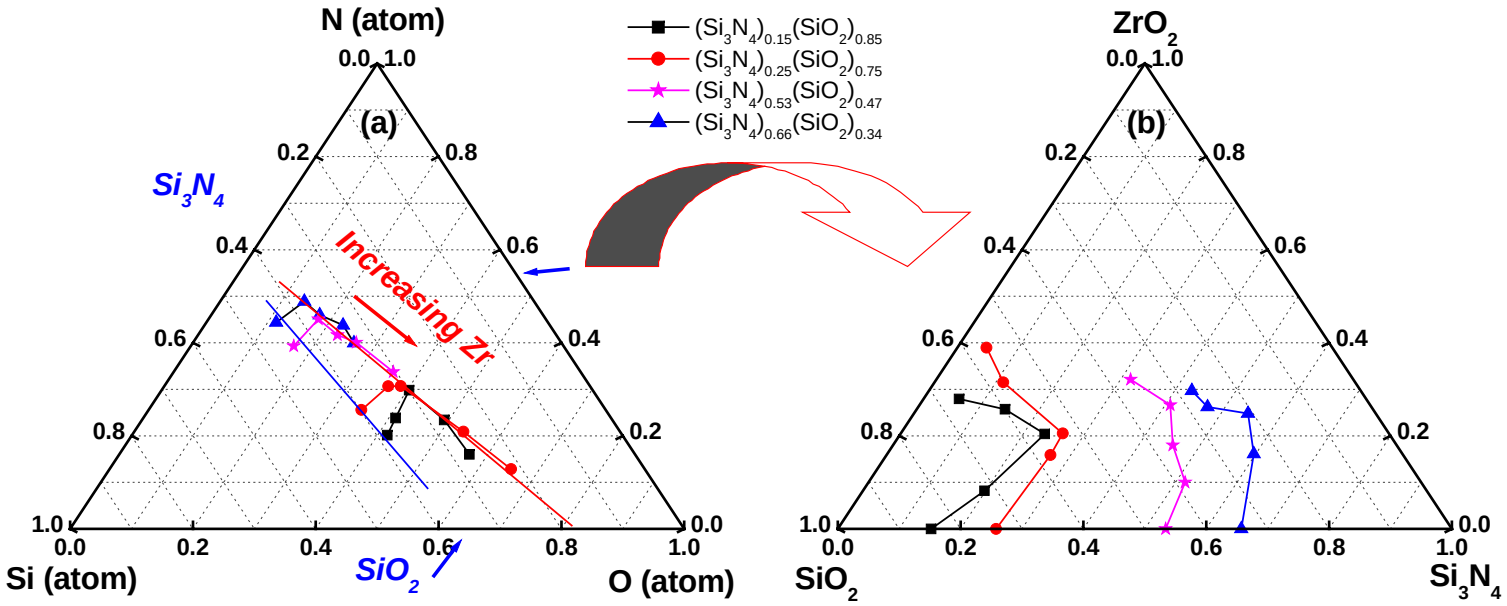

Figure 4.7. (a) The atomic percent concentration ternary diagram of as-deposited alloys of [$(Si_3N_4)(SiO_2)$] and [$(ZrO_2)(Si_3N_4)(SiO_2)$] and (b) their corresponding alloy composition.

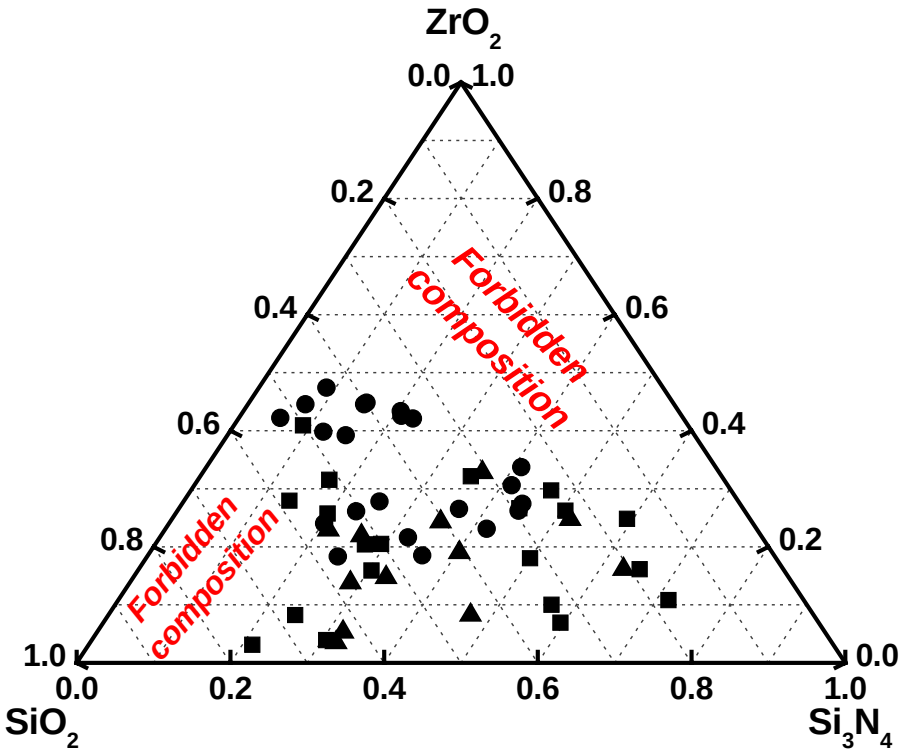

Figure 4.8. Alloy composition boundary and "*forbidden composition*" in ternary diagram of as-deposited Zr-Si oxynitride films.

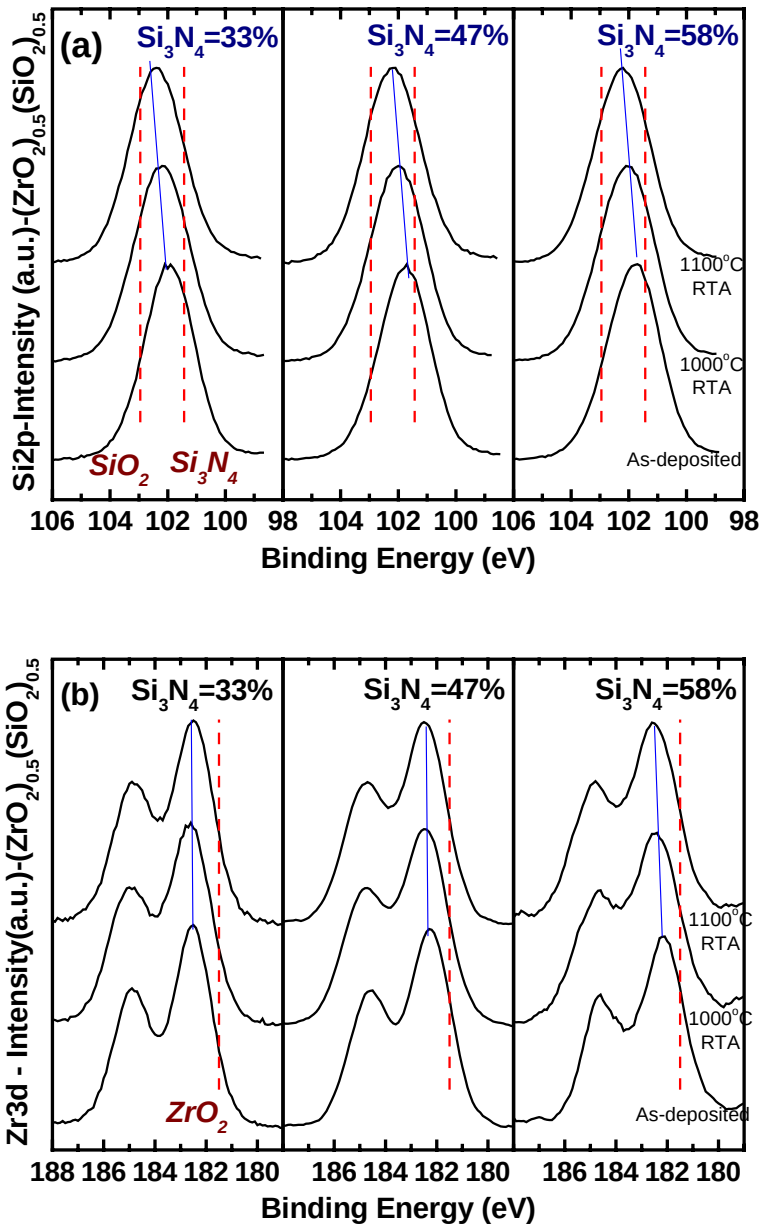

Figure 4.9. XPS core-level (a) Si2p and (b) Zr3d spectra of Zr-Si oxynitride with $(ZrO_2)_{0.5}(SiO_2)_{0.5}$ as a function of Si_3N_4 amount. Each of these spectra is for as-deposited, 1000°C, and 1100°C annealing.

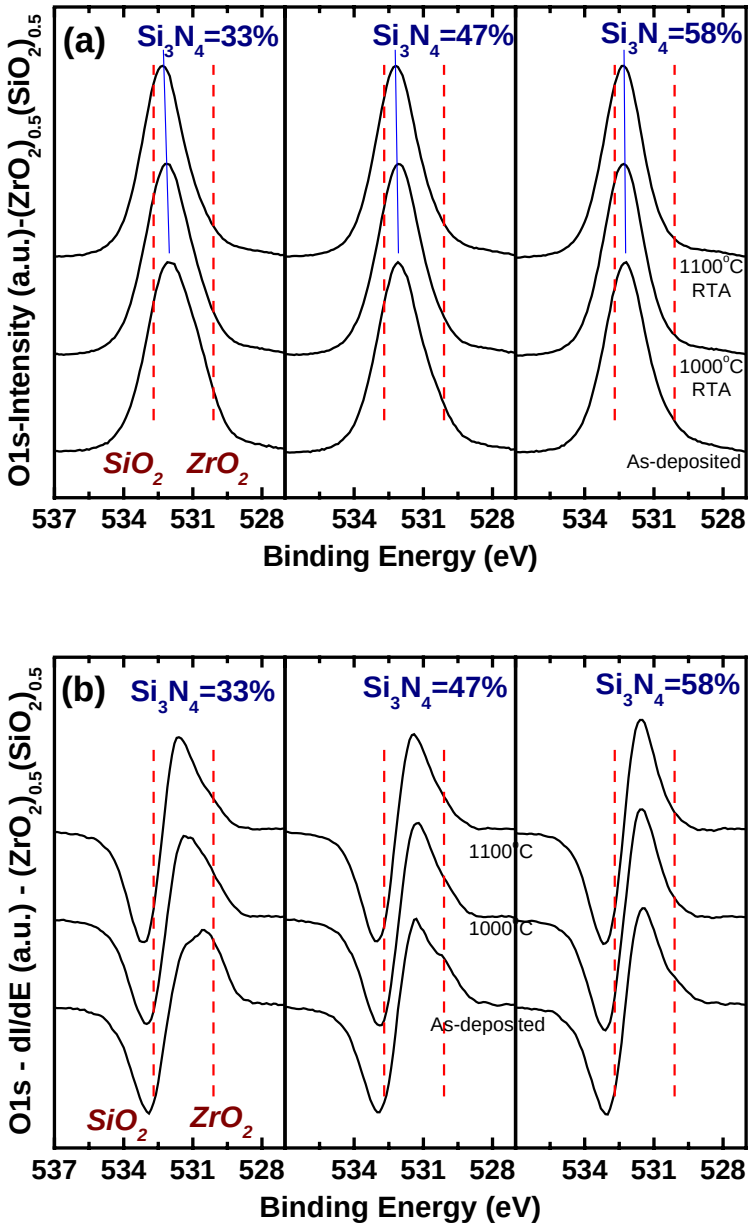

Figure 4.10. XPS core-level (a) O1s and (b) O1s derivative spectra of Zr-Si oxynitride with $(ZrO_2)_{0.5}(SiO_2)_{0.5}$ as a function of Si_3N_4 amount. Each of these spectra is for as-deposited, 1000°C, and 1100°C annealing.

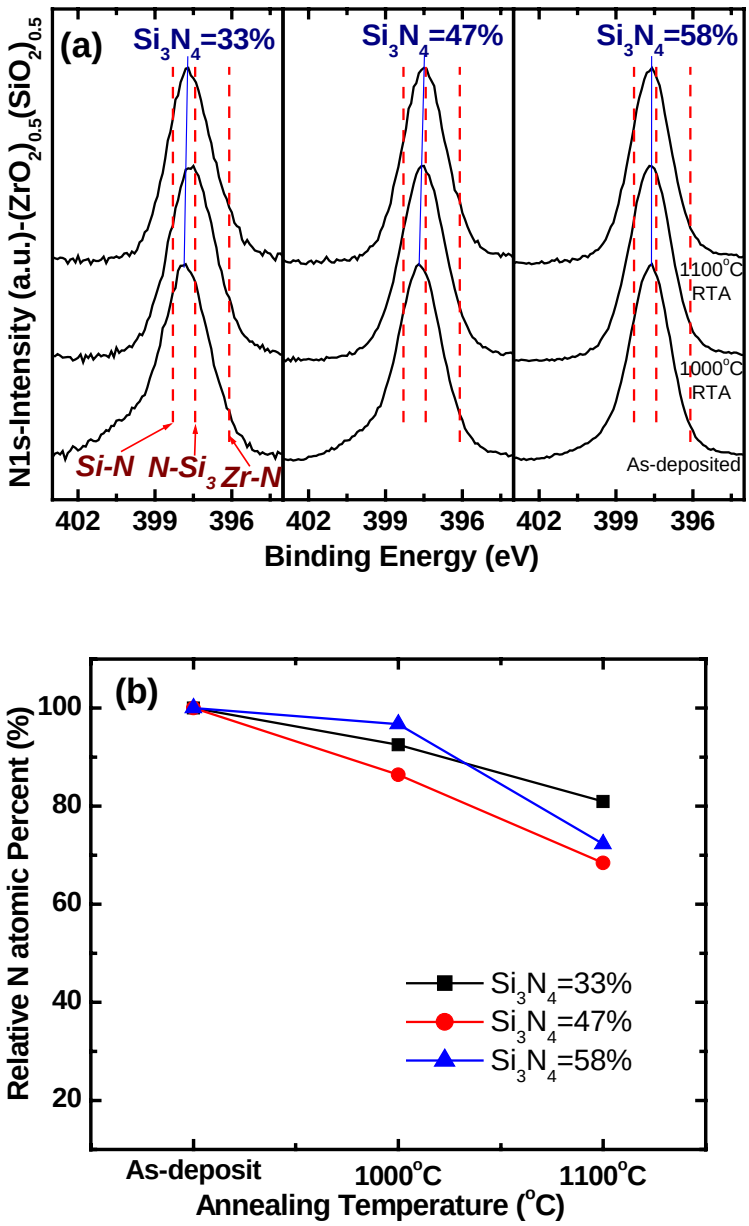

Figure 4.11. XPS core-level (a) N1s spectra of Zr-Si oxynitride with $(ZrO_2)_{0.5}(SiO_2)_{0.5}$ as a function of Si_3N_4 amount and (b) its relative atomic percent after annealing. Each of these spectra is for as-deposited, 1000°C and 1100°C annealing.

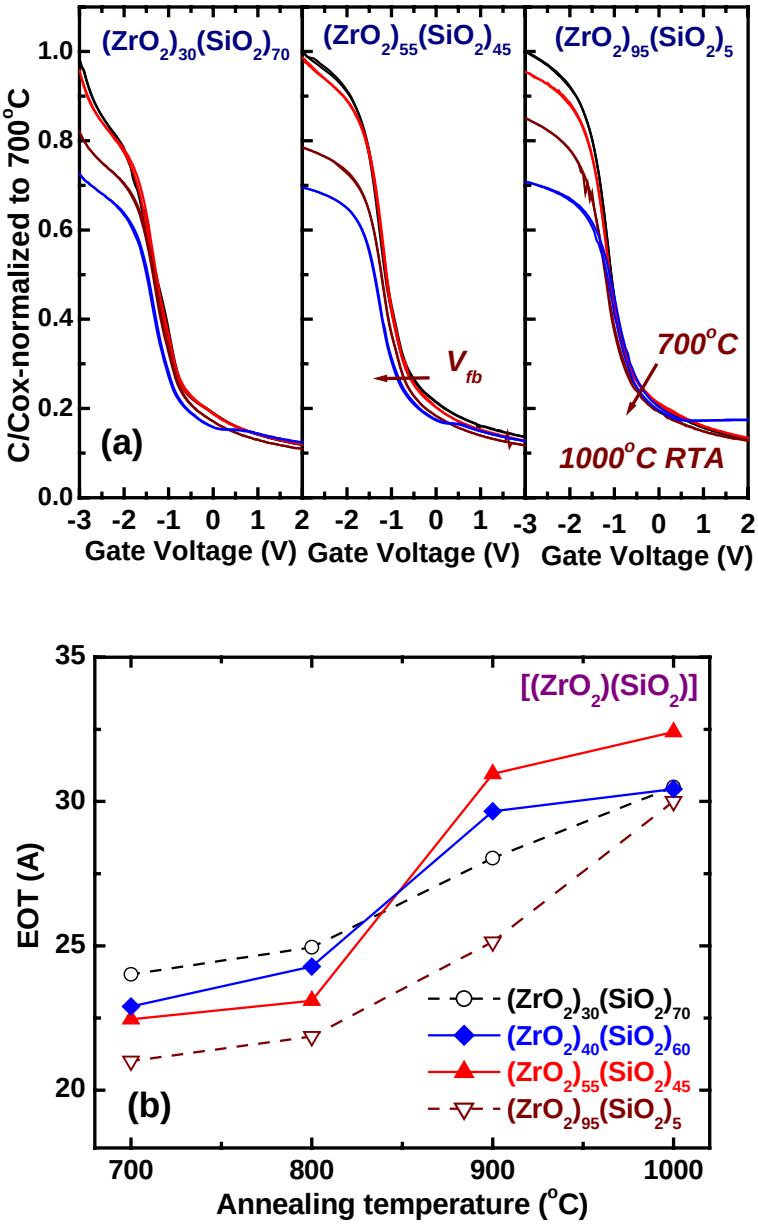

Figure 4.12. (a) C-V characteristics changes by annealing temperature for Al/Zr-silicate/Si substrate NMOS capacitor as a function of silicate composition and (b) corresponding EOT changes by annealing temperature.

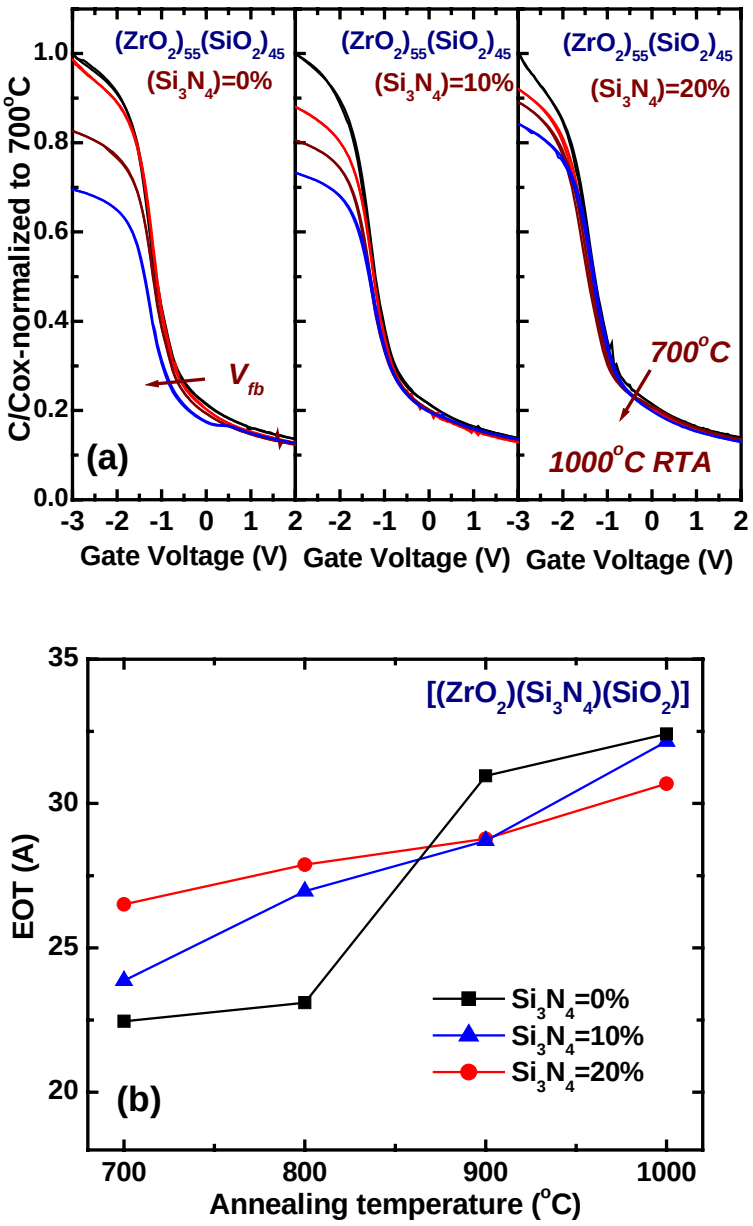

Figure 4.13. (a) C-V characteristics change by annealing temperature for Al/Zr-Si oxynitride/Si substrate NMOS capacitor as a function of Si_3N_4 amount and (b) corresponding EOT changes by annealing temperature.

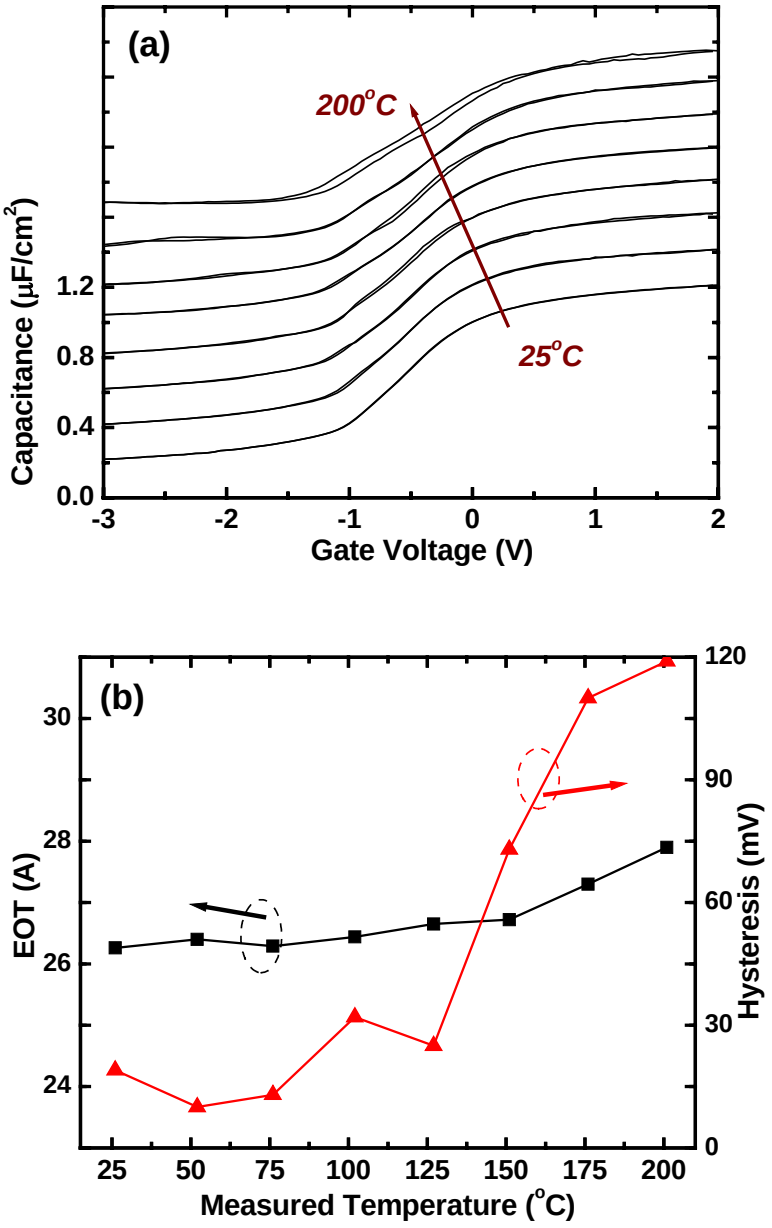

Figure 4.14. Temperature dependence of (a) C-V characteristics and (b) EOT and hysteresis for Al/Zr-Si oxynitride/Si substrate PMOS capacitor.

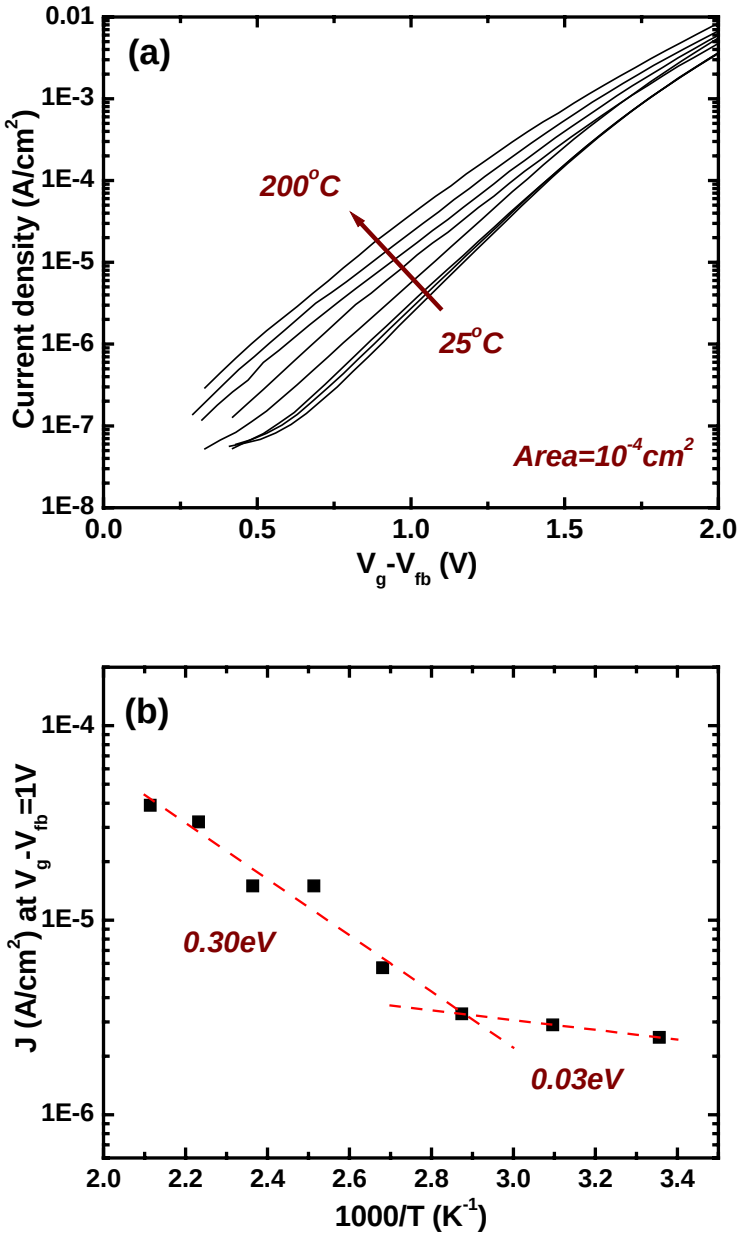

Figure 4.15. Temperature dependence of (a) J-V characteristics and (b) J vs. 1/T for Al/Zr-Si oxynitride/Si substrate PMOS capacitor.

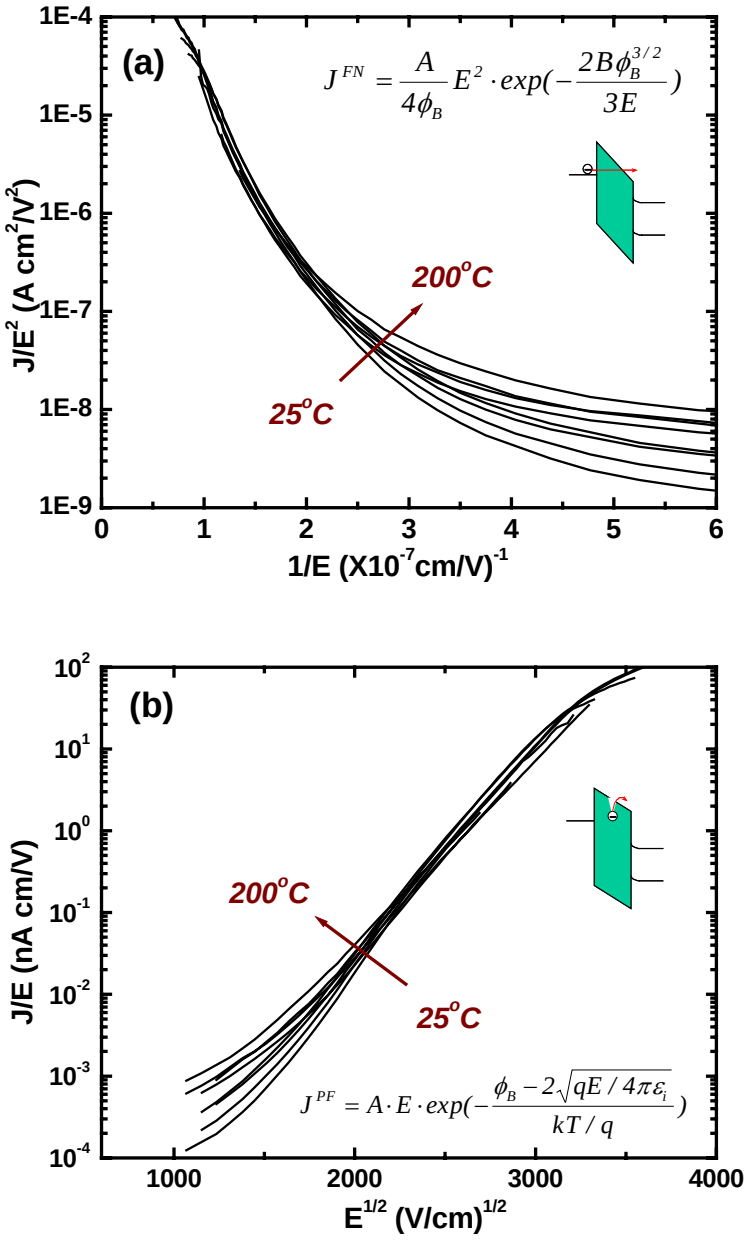

Figure 4.16. Leakage current mechanism for Zr-Si oxynitride depending on the measuring temperature, (a) Fowler-Nordheim plot and (b) Poole-Frenkel plot.

Table 4.1. XPS core level binding energy for pseudo-ternary Zr-Si oxynitride films of $(ZrO_2)_{0.5}(SiO_2)_{0.5}$ composition as a function of Si_3N_4 amount.

$(ZrO_2)_{0.5}$ $(SiO_2)_{0.5}$	Si 2p			Zr 3d5/2			O 1s			N 1s		
(Si_3N_4)	33%	47%	58%	33%	47%	58%	33%	47%	58%	33%	47%	58%
As-deposited	101.95	101.78	101.83	182.50	182.23	182.15	531.83	531.98	532.20	397.79	397.65	397.65
1000C RTA	102.21	102.03	102.08	182.60	182.42	182.41	532.04	532.02	532.31	397.57	397.54	397.67
1100C RTA	102.39	102.20	102.23	182.47	182.42	182.48	532.25	532.13	532.33	397.72	397.50	397.66

CHAPTER 5. SPECTROSCOPIC STUDY OF CHEMICAL PHASE SEPARATION IN Zr-Si OXYNITRIDE ALLOYS; FTIR and XPS ANALYSIS

5.1 INTRODUCTION

As the lateral dimension for complementary metal oxide semiconductor (CMOS) are shrunk down to increase the integration, the thickness of the gate dielectric is also reduced to meet the device performance [1]. But the direct tunneling current increases exponentially with decreasing thickness establishing an important limitation on the use of the conventional SiO_2 as a dielectric [2,3]. Recently, intense research has been focused on high dielectric constant materials such as ZrO_2 [4,5], HfO_2 [6,7] and their silicate to replace gate dielectric by increasing the physical thickness [8~10], which are thermodynamically stable with silicon and excellent electrical properties [11~13]. It was reported [14], however, that phase separation and crystallization often occurred when Hf and Zr silicate were annealed above 900°C. These problems caused the leakage current increase through the grain boundary and roughness of the film surface created by crystallization.

One of the other important problems that have to be considered when using poly Si gate electrode is dopant penetration. The boron doped p^+ poly Si gate electrode for the PMOS device improves the short channel effects, but boron diffusion from the poly Si gate electrode into the channel region through the gate dielectrics can degrade PMOS

device performance [15~17]. Therefore, for boron doped p^+ poly Si gate electrode applications, it is necessary to have a diffusion barrier in the gate oxide to prevent the boron penetration into the Si substrate and the channel region. Nitrogen atoms incorporated into the gate dielectric structure are one of candidates for blocking boron diffusion. Nitridation of the top layer of HfO_2 can effectively block boron diffusion [18] and bulk N can help prevent phase separation in Hf and Zr silicate [19,20]. N incorporation into high-k metal oxides may also provide a way to control the flat band shifts by modifying the defect structures in the bulk and at the interface. Because thermodynamics of the Si-O-N system and the kinetics of nitrogen incorporation are rather complex, the different methods of SiON preparation could produce SiON films with different N spatial distributions [21~23] and with different electrical properties, especially in the case of plasma nitridation where active nitrogen species are introduced into the oxide. But our previous results [24] revealed that the incorporated nitrogen atoms break the oxygen atom bonding and (or) be substituted for the oxygen atom site and make a bond with Zr atoms as well as Si atoms in the middle range silicates. So zirconium nitride is known as metallic conductor that act as a leakage source in the middle range of silicate [25,26].

In this letter, we report that Zr-Si oxynitride films were deposited by putting Zr source into N_2/N_2O gas mixture and, then the concentration of incorporated nitrogen was measured by on-line Auger electron spectroscopy (AES) The chemical bonding and the effects of the nitrogen atoms on the chemical phase separation in Zr-Si oxynitride films were studied using Fourier transform infrared (FTIR) spectroscopy and x-ray photoelectron spectroscopy (XPS)

5.2 FILM PREPARATION

IR absorption measurements were performed using a Nicolet Magna FTIR 750 spectrometer in the mid-IR (4000~400cm^{-1}) and far-IR (700~50cm^{-1}) range of the electromagnetic spectrum. The spectrometer was continuously purged with N_2 to minimize absorption from IR active components present in the atmosphere, such as H_2O and CO_2. The mid-IR measurements utilized a DTGS detector with a KBr window and a KBr beam splitter, while the far-IR measurements used a DTGS detector with a polyethylene window and a Si substrate beam splitter. The spectrometer utilized a He/Ne laser for optical bench alignment, which was performed prior to all data collection.

Alloys were deposited on high resistivity Si (100) substrate to minimize absorption by free charge carriers. The substrates were polished on both sides to prevent multiple internal reflections. The thinner substrates have the advantage of smaller contributions from substrate IR absorption due to oxygen and carbon impurities and 2nd order IR active vibrations. In addition, the thinner substrates were better suited for far IR measurement down to 100cm^{-1} due to interference effects observed in the far IR spectral regime. Double side polished Si wafer was used for IR measurements. Prior to the films deposition, the Si wafers were dipped in a H_2O/HF (100:1) solution to remove the native oxide and to provide a clean, hydrogen terminated, Si surface. Film thickness was deposited thicker than approximately 150nm thick to ensure good IR absorption sensitivity.

Off-line XPS measurements of Si2p, Zr3d, O1s, and N1s core levels were made using a Riber LAS-3000 spectrometer with non-monochromatic Mg Kα radiation (1253.6eV) and pass energy of 20eV. The spectral resolution was approximately 1eV. The system base pressure for XPS measurements was approximately 3×10^{-10}Torr. Data were corrected for charging effects using the C1s peak at 284.5eV from adventitious carbon contamination on the film surface. The repeatability of measuring peak spectral positions was found to be <0.2eV.

5.3 RESULTS AND DISCUSSION

Figure 5.1a shows the ternary diagram for Zr-Si oxynitride alloy. As mentioned in chapter 4, we can see two *"forbidden composition"* regions both in SiO_2 corner and ZrO_2 corner. The Zr-Si oxynitride films composition properties were discussed in section 4.4.1. To investigate the nitrogen atoms effect on the phase separation, the film internal structure with composition and post-deposition annealing temperature were characterized by increasing the Si_3N_4 amount in 50% and 30% Zr silicate as shown in Figure 5.1b.

Figure 5.2a displays off-line mid and far FTIR spectroscopy for SiO_2 and Si_3N_4 films of as-deposited, 900°C, 1000°C and 1100°C annealing in Ar ambient for 30sec. The as-deposited film of SiO_2 shows evidence of O-H stretching bonding (3750~2800cm^{-1}) and C-H stretching bonding (3025~2800cm^{-1}) [27~29]. But the bending mode vibration of O-H (~1620cm^{-1}) and C-H (1500~1400cm^{-1}) bonding are detected very weak that there are little bonding in the films. Following heat treatment at 900°C annealing no evidence of O-H stretching vibration in the films is detected. The O-H bending feature at

approximately 1620cm^{-1} is characteristic of water, H_2O. Definite N-H stretching vibration (3360cm^{-1}) is observed in Si_3N_4 alloy as shown in Figure 5.2b and this vibration still exist, though its intensity decrease, following heat annealing up to 1100°C.

Figure 5.3 shows the mid- and far-IR absorption spectra of SiO_2 [30~32] through Si_3N_4 films measured at 8cm^{-1} resolutions from 1500 to 300cm^{-1}. It is well known [31] that amorphous SiO_2 can be described as a random network of corner-connected SiO_4 tetrahedra, which can be characterized by the bond angle between two tetrahedral. The three main vibration modes in the absorption spectrum as deposited SiO_2 are described as following vibrations. 1) a stretching mode at 1061cm^{-1}, 2) a bending mode at 810cm^{-1} and 3) out-of-plane rocking mode at 455cm^{-1}. No peak shift in both bending and rocking mode vibration by annealing, while the stretching vibration peak shifts by 15cm^{-1} to higher wave number at 1076cm $^{-1}$ by subsequent annealing at 1100°C due to the relaxation of internal structure of the films. (FWHM of stretching vibration decrease proportionately) We can see the shoulder at higher wave number of the stretching vibration (~1200cm $^{-1}$) is related to the out-of-phase stretching motions of near neighbor O-atoms [33]. Figure 5.3c shows the mid- and far-IR absorption spectra of Si_3N_4 films measured at 8cm^{-1} resolutions from 1500 to 300cm^{-1}. A dominant peak in the region around 890cm^{-1} is attributed to the stretching vibrations of Si-N bond. And the bending vibration of Si-O almost overlapped to the main peak. It is also noticed that the absorption peak of Si-N bond has a shoulder around 1180cm^{-1} that is considered to originate from N-H bending vibrations. Like the films of SiO_2, the stretching vibration peak in Si_3N_4 films shift by 7cm^{-1} to higher value by annealing at 900°C, no shift thereafter. Figure 5.3b is the FTIR absorption spectra of Si oxynitride films,

$(Si_3N_4)_{0.5}(SiO_2)_{0.5}$. The main peak in as-deposited films is at 922cm^{-1}, which is between Si-N stretching vibration and Si-O stretching vibration. By increasing the annealing temperature, the main peak gradually increased to 941cm^{-1}. In addition, the main peak broadens by annealing due to the increment of Si-O^{-1} (970cm^{-1}) terminal bonds [34~36]. That is attributed to the films oxidation by annealing though no oxygen source to oxidize.

Figure 5.4 shows the mid and far FTIR absorption spectra of 30% Zr silicate and same composition films with 20% and 40% Si_3N_4 amount. The peak shape and location of as-deposited films are almost similar to the Si oxynitride films. But the peak abruptly was changed its shape by annealing in Zr silicate as shown in Figure 5.4a. The intensity of Si-O stretching vibration peak at 1061cm^{-1} remarkably increased and the intensity at 970cm^{-1} associated Si-O^{-1} [37] decreased after annealed above 1000°C. Moreover, Si-O rocking vibration peak intensity clearly increased after annealed above 1000°C. Eventually, Si-O stretching and rocking peaks were remained at 1100°C annealing. These results are interpreted as the result of a transition from Si-O-Zr bonding [38] to Si-O-Si and Zr-O-Zr bonding, i.e. *chemical phase separation*. By adding the Si_3N_4 phase (20%) into same Zr silicate composition, Si-O stretching peak also appeared but its original (~970 cm^{-1}) peak still existed after annealing as shown in Figure 5.4b. But the relative intensity of Si-O stretching peak sharply increased by annealing temperature. This is considered that SiO_2 phase is segregated in the Zr-Si oxynitride bonding. (or a small part of Zr-Si oxynitride alloys are separated by annealing) When the amount of Si_3N_4 phase is increased to 40%, Si-O stretching also appear by annealing but the intensity maintain up to 1100°C annealing as shown in Figure 5.4c. These results indicated that phase separation was suppressed by increasing the amount of Si_3N_4 in Zr-Si oxynitride alloy.

This suppression effect on phase separation is confirmed by XPS analysis. Based on core-level chemical shifts measured by XPS in pseudo-binary metal oxide alloys, an empirical rule has been developed which qualitatively describe relationships between core-level binding energy and the alloy local bonding environments [39,40]. Figure 5.5 shows the XPS binding energy of O1s core level in Zr-Si oxynitride films. O1s binding energy in Zr silicate films is composed of both ZrO_2 and SiO_2 sub-peak as shown in Figure 5.5a. By annealing at 900°C, the relative intensity of ZrO_2 sub-peak increased and the distinct doublet observed in the XPS O1s spectrum of the alloy annealed at 1000°C. The Zr-Si oxynitride (20% Si_3N_4 phase) shows same two sub-peaks as shown in Figure 5.5b but the ZrO_2 sub-peak decreases as increasing the annealing temperature. As the amount of Si_3N_4 increased up to 40% in Zr-Si oxynitride alloy, Figure 5.5c, the sub-peak in ZrO_2 side almost disappeared at the films annealed at 1100°C. Figure 5.6 displays the derivative spectrum of above XPS O1s binding energy, which is consistent with the chemical phase separation detected by FTIR analysis. So these results indicate that nitrogen atoms inhibited the Zr-Si oxynitride alloy from being separated into c-ZrO_2 and α-SiO_2. In particular, it is considered that FTIR analysis is more sensitive in detecting the phase separation than XPS analysis.

In the 50% Zr silicate with a variable amount of Si_3N_4 showed the same trend of the phase separation. Figure 5.7, 5.8, and 5.9 are the mid and far FTIR absorption spectra, XPS binding energy of O1s core level, and its derivative spectrum, respectively. Like the 30% Zr silicate alloy, 50% silicate alloys showed same results that nitrogen atoms suppress the phase separation as well as crystallization as increasing the nitrogen atoms.

The role of nitrogen atoms in suppressing chemical phase separation of Zr-Si oxynitride films can be explained as following. Nitrogen atom is 3-fold coordination, so Si_3N_4 has 3.4 bonding per atom, while SiO_2 has 2.7 bonding per atom. This means that atomic immigration for phase separation, such as Zr and/or Si atoms, need more activation energies to overcome the connected bonding as increasing the amount of Si_3N_4 phase in Zr-Si oxynitride. Figure 5.10 displays the schematic of phase separation of low and high amount of Si_3N_4 phase in Zr-Si oxynitride. In Zr-Si oxynitride films with low Si_3N_4 as shown in Figure 5.10a, nitrogen atoms replaced oxygen atoms and thereby made a scattered N-Si_2-O bonding. In this network, Si and Zr atoms can closely connected each other and easily moved if there were small activation energy. Whereas nitrogen atoms in higher percentage as in Figure 5.10b made a bonding with a silicon atom, so N-Si_3 bonding is major network in Zr-Si oxynitride films.

5.4 CONCLUSION

In summary, the Zr-Si oxynitride alloy as a candidate for conventional SiO_2 dielectric films was deposited using RPECVC system. There is a composition boundary in Zr-Si oxynitride ternary diagram that trend is well agreement with nitrogen amount incorporated by plasma nitridation. The effect of nitrogen atoms in the Zr-Si oxynitride alloy on the phase separation was investigated by FTIR and XPS analysis. Zr silicate alloys with no Si_3N_4 phase were chemically separated into the SiO_2 and ZrO_2 phase as annealed above 900°C. While chemical phase separation in Zr silicate films with Si_3N_4 phase (Zr-Si oxynitride) were suppressed as increasing the amount of Si_3N_4 phase due to

the narrow bonding network in Si_3N_4 phase. (3.4 bonds/atom for Si_3N_4 network, 2.67 bonds/atom for SiO_2 network) In particular, FTIR analysis is more sensitive in detecting of internal structure change of Zr-Si oxynitride than XPS analysis.

5.5 REFERENCES

[1] M.L.Green, E.P.Gusev, R.Degraeve, E.L.Garfunke, J. Appl. Phys. **90** 2057 (2001)

[2] International Technology Roadmap for Semiconductors, 1999, Semiconductor Industry Association, (1999)

[3] Y.Ma, Y.Non, L.Stecker, D.R.Evans, and S.T.Hsu, Tech. Dig. Int. Electron Devices Meet, 149 (1999)

[4] A.S.Kao, J. Appl. Phys. **69**, 3309 (1991)

[5] M.Copell, M.Gribelyuk, and E.Gusev, Appl. Phys. Lett. **76**, 436 (2000)

[6] J.Aarik, A.Aidla, A.A.Kiisler, T.Uustare, and V.Sammelselg, Thin Solid Films **340**, 110 (1999)

[7] B.H.Lee, L.Kang, W.-J.Qi, R.Nieh, Y.Jeon, K.Onish, and J.Lee, IEDM Tech.Dig. 166 (1999)

[8] H.S.Kim, S.A.Campbell, and D.C.Gilmer, IEEE Electron Device Lett. **18**, 465 (1997)

[9] G.B.Alerts, D.J.Werder, Y.Chabal, H.C.Lu, E.P.Gusev, E.Garfunkel, T.Gustafsson, and R.S.Urdahl, Appl. Phys. Lett. **73**, 1517 (1998)

[10] C.Basceri, S.K.Streiffer, and A.I.Kingon, J. Appl. Phys. **82**, 2497 (1997)

[11] G.D.Wilk and R.M.Wallace, Appl. Phys. Lett. **74**, 2854 (1999)

[12] G.D.Wilk, R.M.Wallace, and J.M.Anthony, J. Appl. Phys. **87**, 484 (2000)

[13] W.Qi, R.Nieh, E.Dharmarajan, B.H.Lee, Y.Jeon, L.Kang, K.Onishi and J.C.Lee, Appl. Phys. Lett. **77**, 1704 (2000)

[14] G.B.Rayner,Jr., D.Kang, Y.Zhang, and G.Lucovsky, J. Vac. Sci. Technol. B **20**, 1748 (2002)

[15] K.S.Krisch, L.Manchanda, F.H.Baumann, M.L.Green, D.Brasen, L.C.Feldman and A.Ourmazd, IEDM Tech. Dig., 325 (1994)

[16] J.Y.C.Sun, C.Wong, Y.Taur and C.H.Hsu, 1989 Symp. VLSI. VLSI Tech.Dig., 17 (1989)

[17] J.R.Pfiester, F.K.Baker, T.C.Mele, H.H.Tseng, P.J.Tobin, J.D.Hayden, J.W.Miller, C.D.Gunderson and L.C.Parrillo, IEEE Trans.Electron Devices, **ED-37**, 1842 (1990)

[18] H.J.Cho, C.S.Kang, K.Onishi, S.Gopalan, R.Nieh, R.Choi, S.Krishnan, and J.C.Lee, IEEE Electron Device Lett. **23**, 249 (2002)

[19] M.R.Visokay, J.J.Chambers, A.L.P.Rotondaro, A.Shanware, and L.Colombo, Appl. Phys. Lett. **80**, 3183 (2002)

[20] D.Niu, R.W.Ashcraft, C.Hinkle, and G.N.Parsons J. Vac. Sci. Technol, A **22**, 445 (2004)

[21] M.L.Green, E.P.Gusev, R.Degraeve, E.L.Garfunkel, J. Appl. Phys. **90**, 2057 (2001)

[22] A.Khandelwal, B.C.Smith, H.H.Lamb, J. Appl. Phys. **90**, 3100 (2001)

[23] A.Raveh, J.Brewer, E.A.Irene, J. Vac. Sci. Technol. A **17**, (2001)

[24] B.Ju and G.Lucovsky (unpublished)

[25] R.Nieh, C.S.Kang, H.J.Cho, K.Onishi, R.Choi, S.Krishnan, J.H.Han, Y.H.Kim, M.S.Akbar and J.Lee, IEEE Trans. Electron Device, **50**, 333 (2003)

[26] I.Milosev, H.H. Strehblow, B.Navinsek and P.Panjan, Surface Science Spectra, **5**, 152 (1998)

[27] R.M.Almeida, T.A.Guiton and C.G.Pantano, J.of Non-Cryst. Solids **121**, 193 (1990)

[28] C.Charles, P.Garcia, B.Grolleau and G.Turban, J. Vac. Sci. Technol. A **10** (4) 1407 (1992)

[29] V.G.Plotnichenko, V.O.Sokolov and E.M.Dianov, J. of Non-Cryst. Solids **261**, 186 (2000)

[30] R.J.Bell, N.F.Bird and P.Dean, J. Phys. **C1**, 299 (1968)

[31] R.J.Bell, P.Dean and D.C.Hibbins-Butler, J. Phys. **C3**, 2111 (1970)

[32] R.J.Bell, P.Dean and D.C.Hibbins-Butler, J. Phys. **C4**, 1214 (1971)

[33] G.Lucovsky, C.K.Wong and W.B.Ploord, J. of Non-Cryst. Solids **59&60**, 839 (1983)

[34] D.Crozier and R.W. Douglas, Phys. Chem. Glasses **6**, 240 (1965)

[35] P.P.Bihuniak and R.A.Condrate, J.of Non-Cryst. Solids **44**, 331 (1981)

[36] C.A. Worrel and T.Henshall, J.of Non-Cryst. Solids **29**, 283 (1978)

[37] G.B.Rayner, Jr., R.Therrien, and G.Lucovsky, MRS Symp. Proc. **611**, c13.1 (2001)

[38] S.W.Lee and R.A.Condrate, Sr., J.Mater. Sci. **23**, 2951 (1988)

[39] F.Liebau, Structural Chemistry of Silicates (Springer-Verlag, New York 1985)

[40] T.L.Barr, J. Vac. Sci. Technol. A **9**, 1793 (1991)

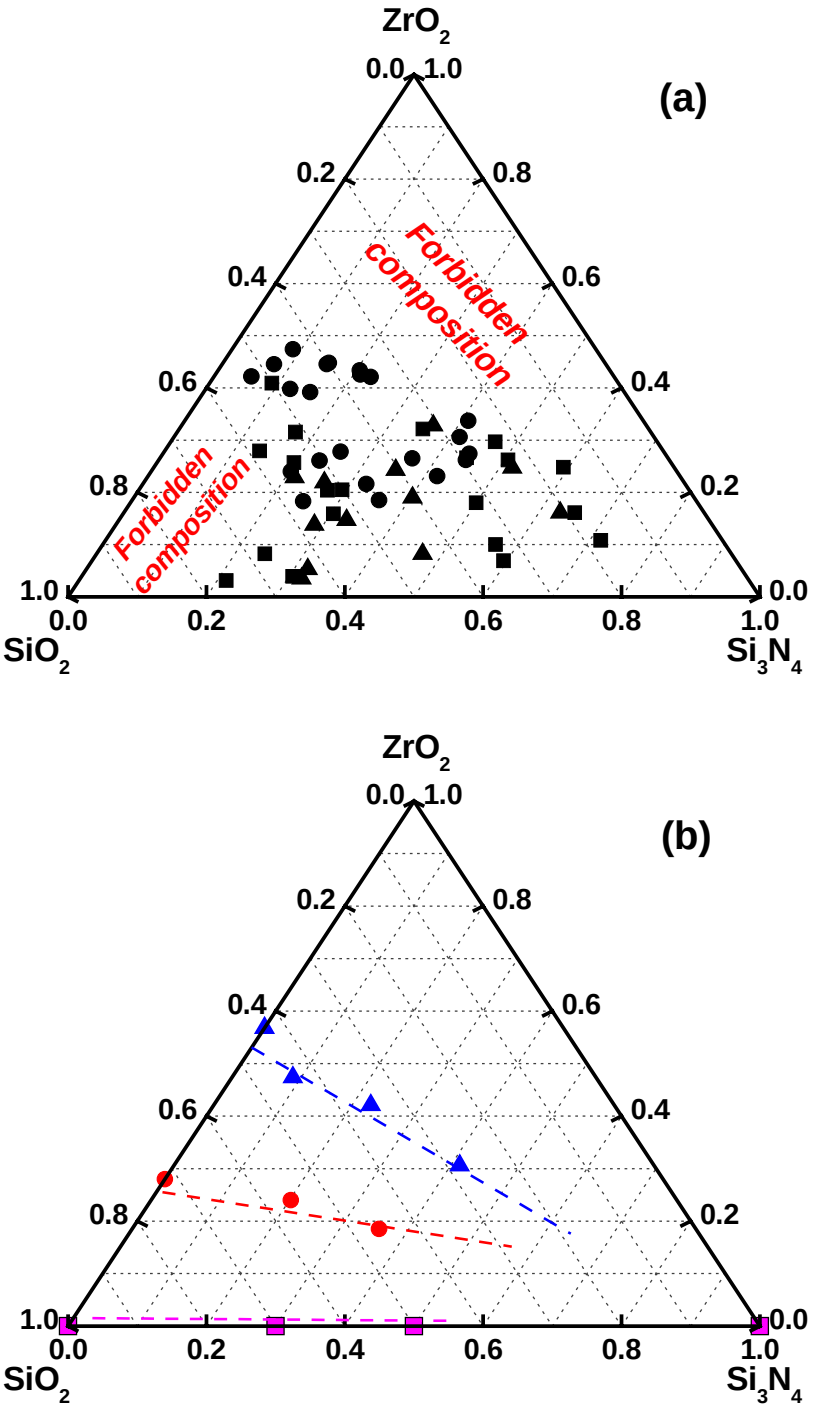

Figure 5.1. (a) The ternary diagram for Zr-Si oxynitride alloy and (b) 50% and 30% Zr silicates as a function of Si_3N_4 amount.

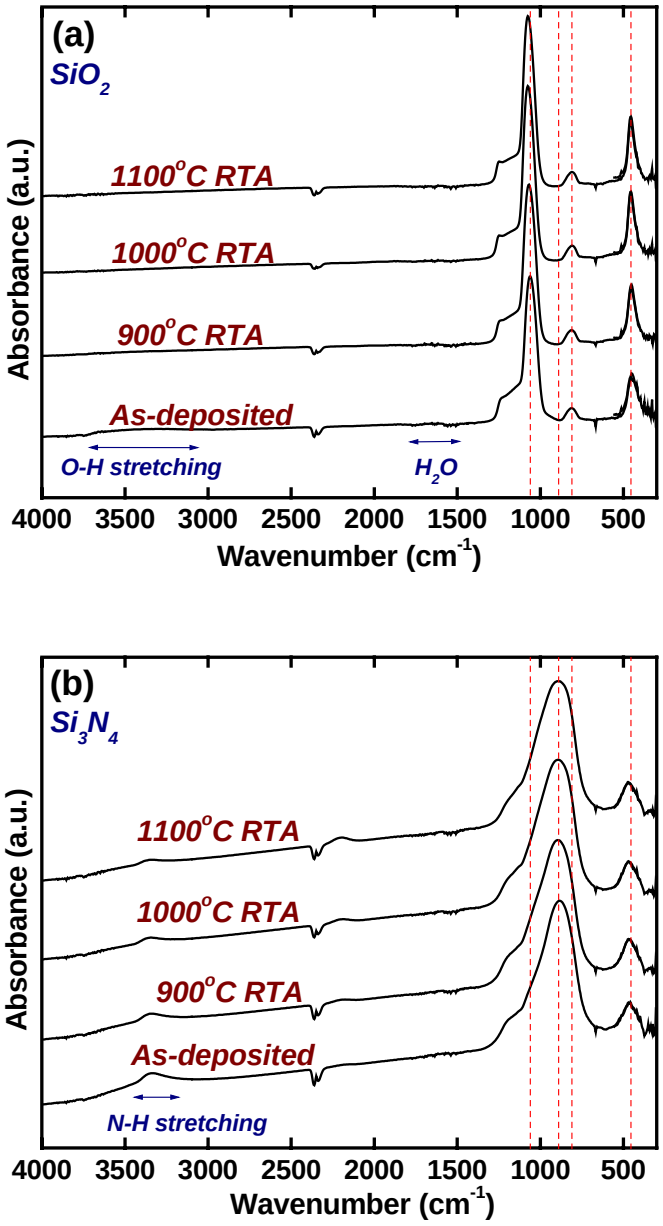

Figure 5.2. FTIR absorption spectra of (a) SiO_2 and (b) Si_3N_4 films as a function of annealing temperature.

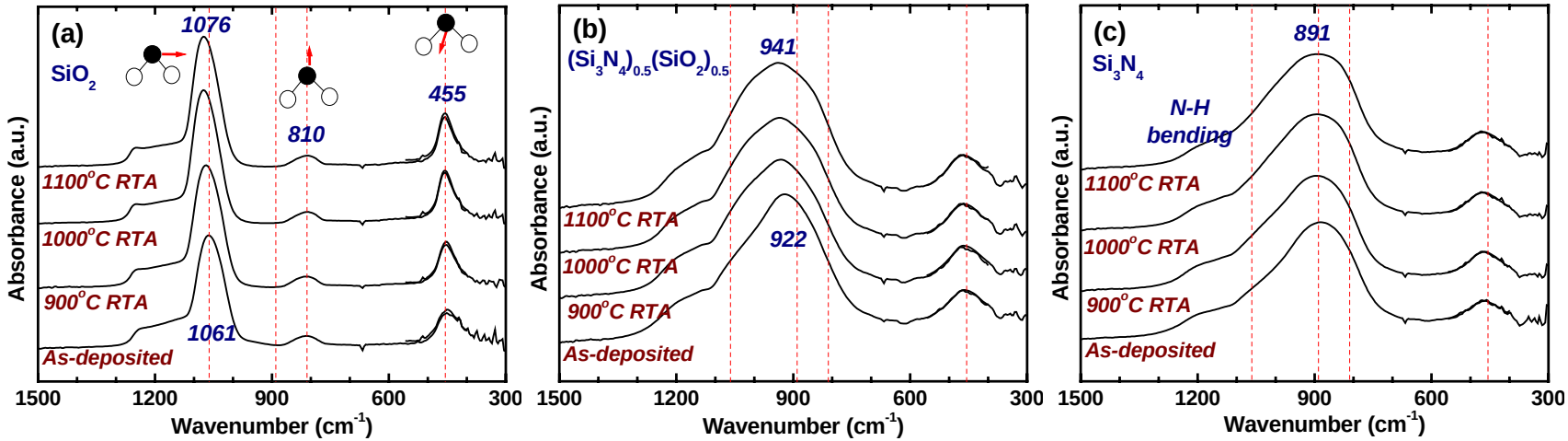

Figure 5.3. FTIR absorption spectra of (a) SiO_2, (b) $(Si_3N_4)_{0.5}(SiO_2)_{0.5}$ and (c) Si_3N_4 as a function of annealing temperature.

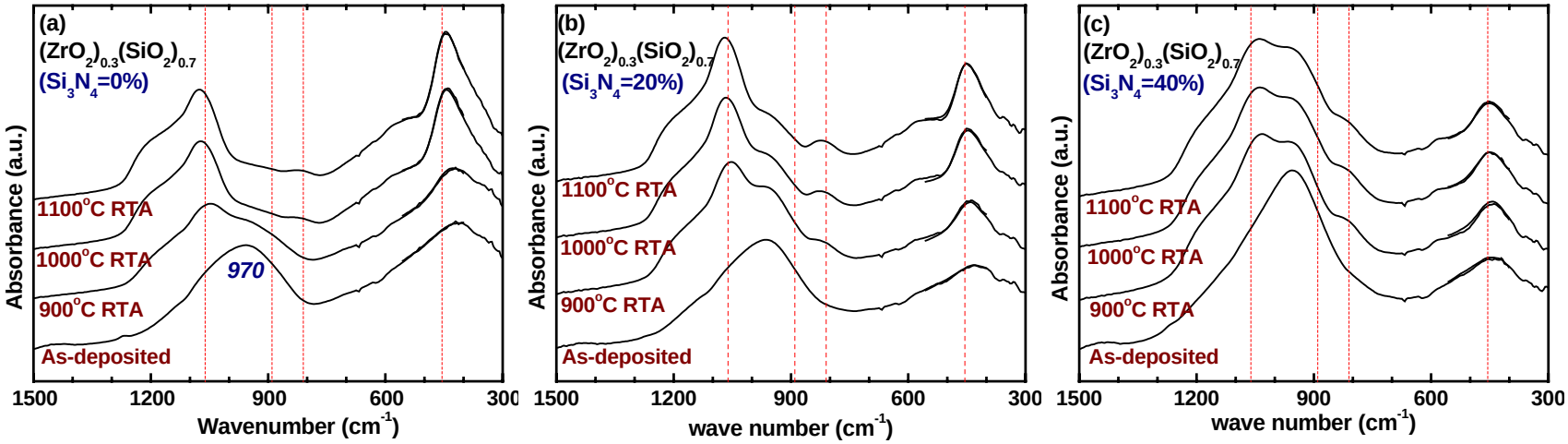

Figure 5.4. FTIR absorption spectra of (a) $(ZrO_2)_{0.30}(SiO_2)_{0.70}$, (b) $(ZrO_2)_{0.24}(SiO_2)_{0.56}(Si_3N_4)_{0.20}$ and (c) $(ZrO_2)_{0.18}(SiO_2)_{0.42}(Si_3N_4)_{0.40}$ as a function of annealing temperature.

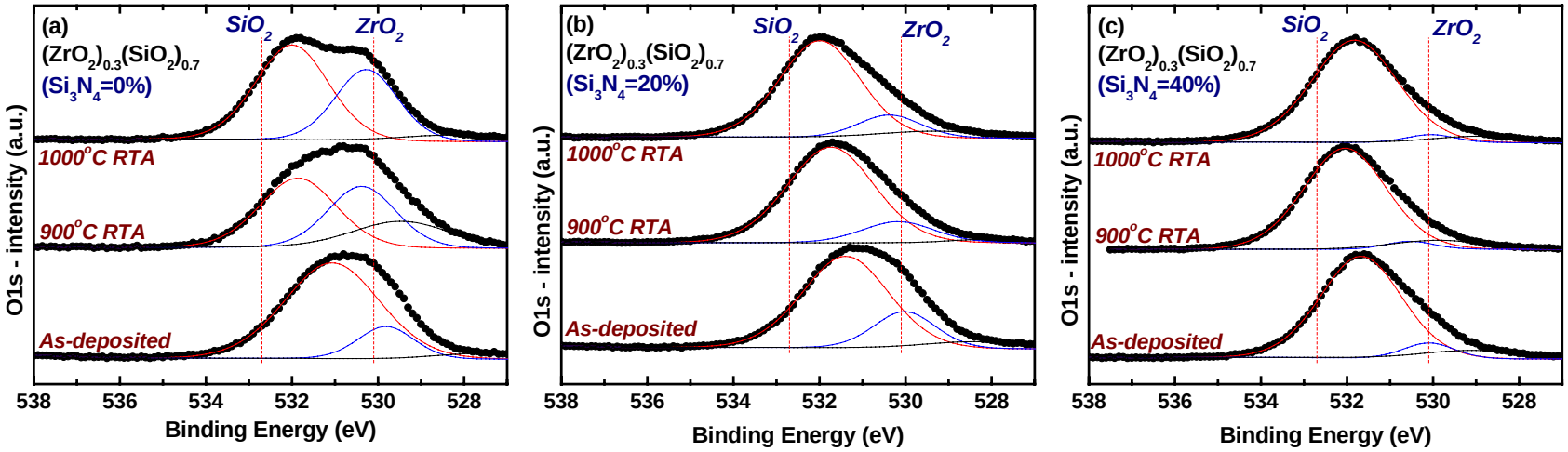

Figure 5.5. XPS core-level O1s spectra of (a) $(ZrO_2)_{0.30}(SiO_2)_{0.70}$, (b) $(ZrO_2)_{0.24}(SiO_2)_{0.56}(Si_3N_4)_{0.20}$ and (c) $(ZrO_2)_{0.18}(SiO_2)_{0.42}(Si_3N_4)_{0.40}$ as a function of annealing temperature.

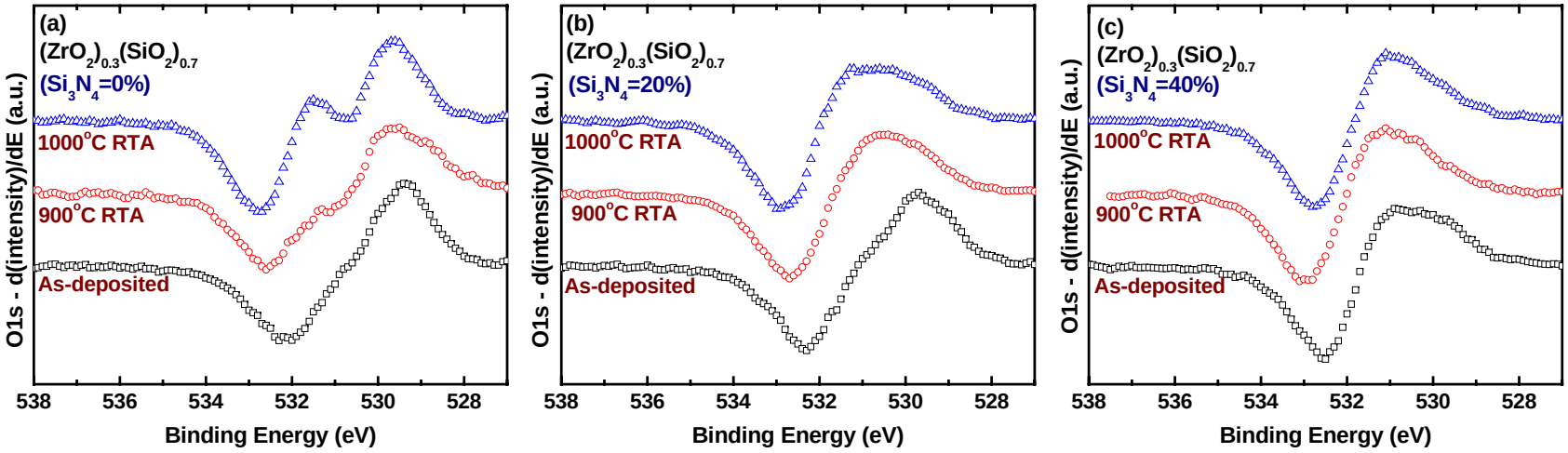

Figure 5.6. XPS core-level O1s derivative spectra of (a) $(ZrO_2)_{0.30}(SiO_2)_{0.70}$, (b) $(ZrO_2)_{0.24}(SiO_2)_{0.56}(Si_3N_4)_{0.20}$ and (c) $(ZrO_2)_{0.18}(SiO_2)_{0.42}(Si_3N_4)_{0.40}$ as a function of annealing temperature.

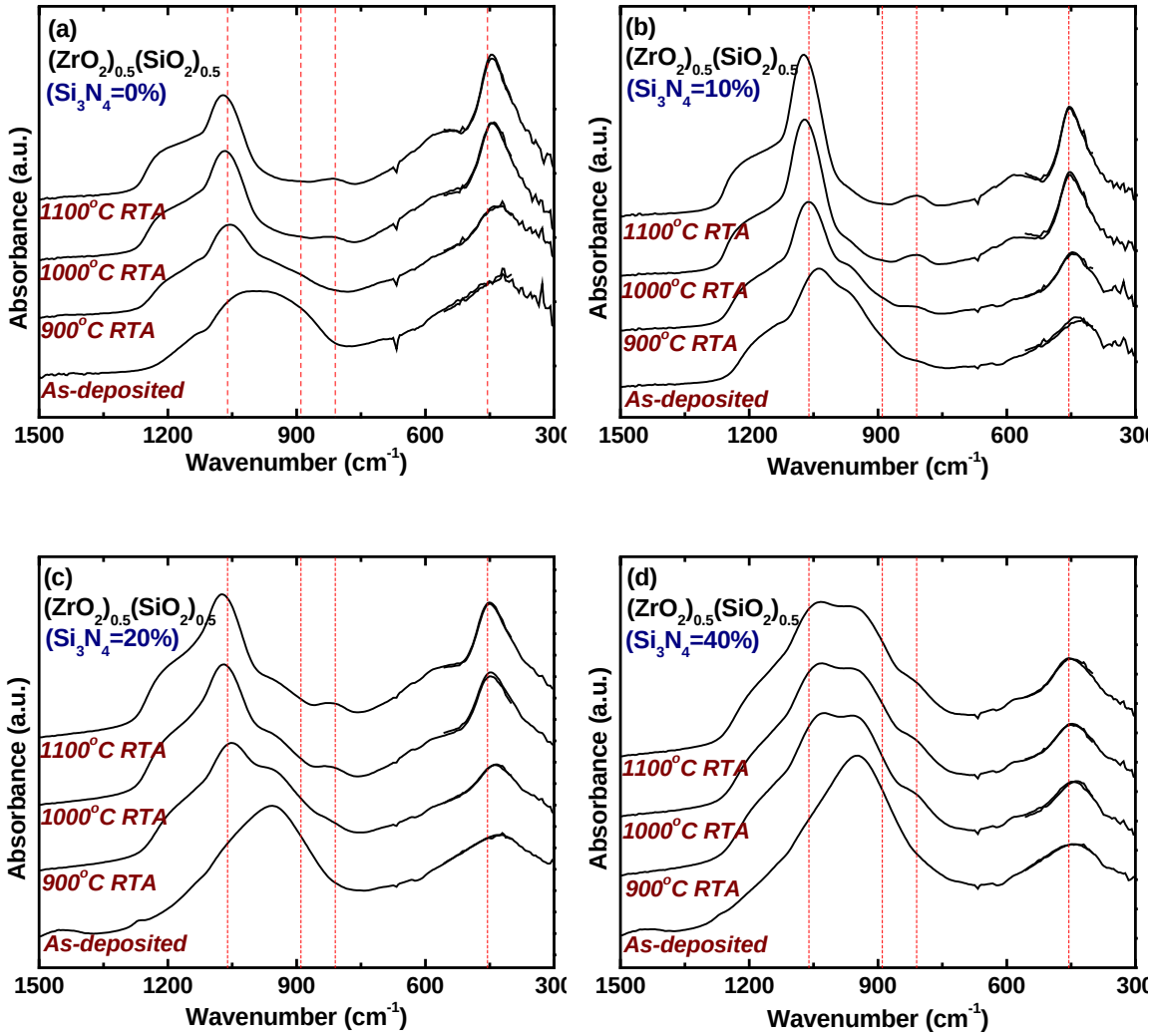

Figure 5.7. FTIR absorption spectra of (a) $(ZrO_2)_{0.50}(SiO_2)_{0.50}$, (b) $(ZrO_2)_{0.45}(SiO_2)_{0.45}(Si_3N_4)_{0.10}$, (c) $(ZrO_2)_{0.40}(SiO_2)_{0.40}(Si_3N_4)_{0.20}$ and (d) $(ZrO_2)_{0.30}(SiO_2)_{0.30}(Si_3N_4)_{0.40}$ as a function of annealing temperature.

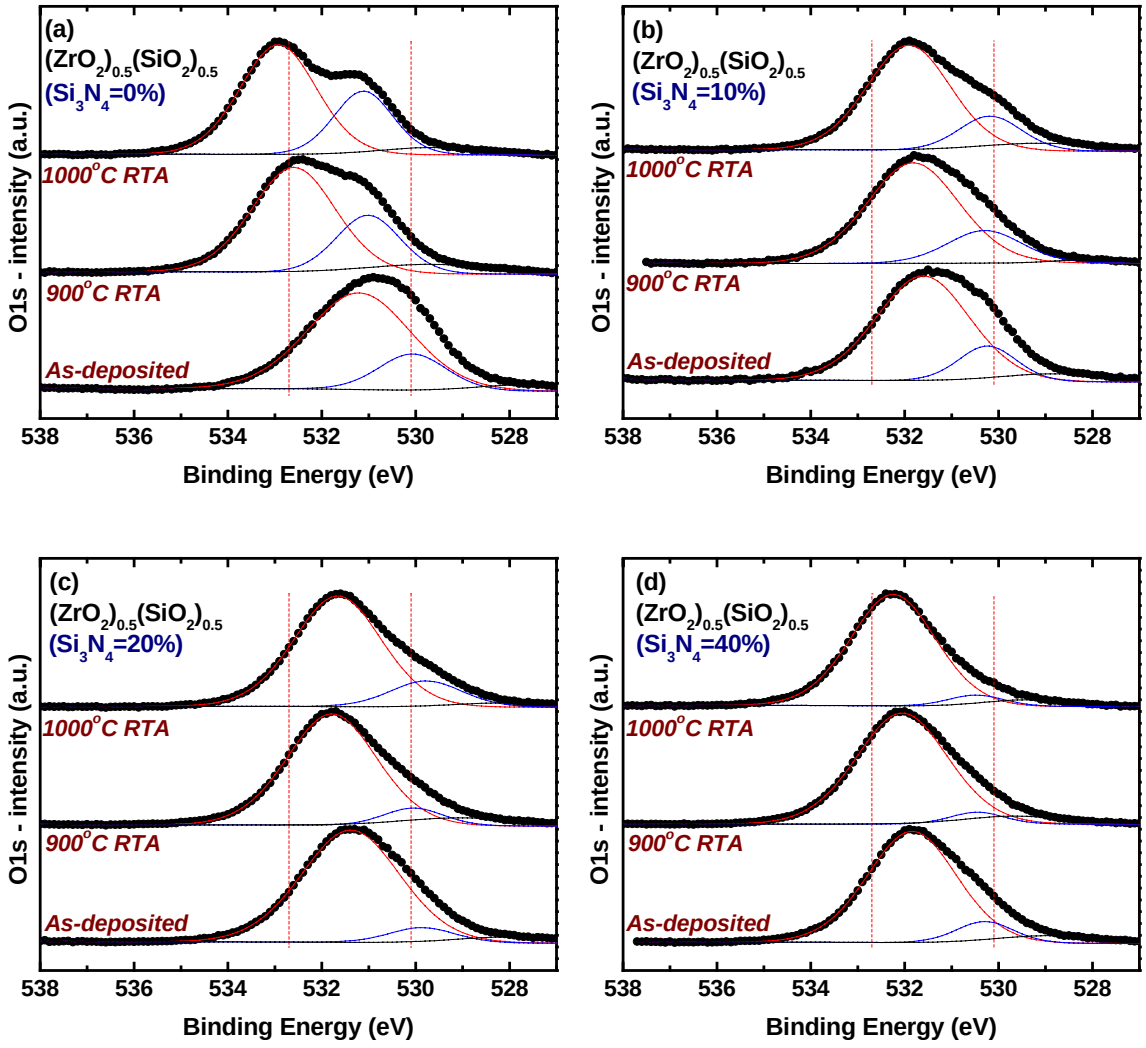

Figure 5.8. XPS core-level O1s spectra of (a) $(ZrO_2)_{0.50}(SiO_2)_{0.50}$, (b) $(ZrO_2)_{0.45}(SiO_2)_{0.45}(Si_3N_4)_{0.10}$, (c) $(ZrO_2)_{0.40}(SiO_2)_{0.40}(Si_3N_4)_{0.20}$ and (d) $(ZrO_2)_{0.30}(SiO_2)_{0.30}(Si_3N_4)_{0.40}$ as a function of annealing temperature.

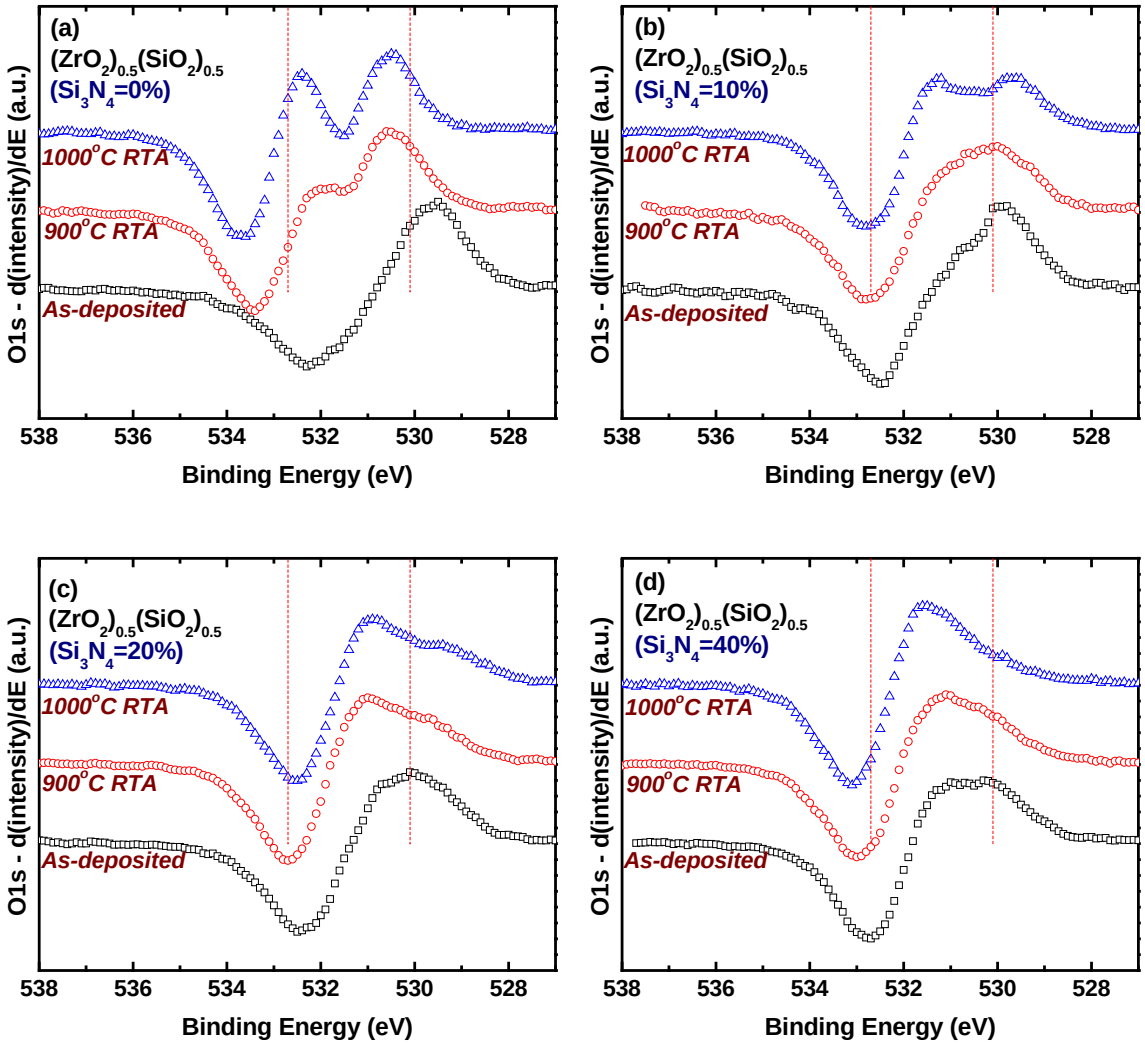

Figure 5.9. XPS core-level O1s derivative spectra of (a) $(ZrO_2)_{0.50}(SiO_2)_{0.50}$, (b) $(ZrO_2)_{0.45}(SiO_2)_{0.45}(Si_3N_4)_{0.10}$, (c) $(ZrO_2)_{0.40}(SiO_2)_{0.40}(Si_3N_4)_{0.20}$ and (d) $(ZrO_2)_{0.30}(SiO_2)_{0.30}(Si_3N_4)_{0.40}$ as a function of annealing temperature.

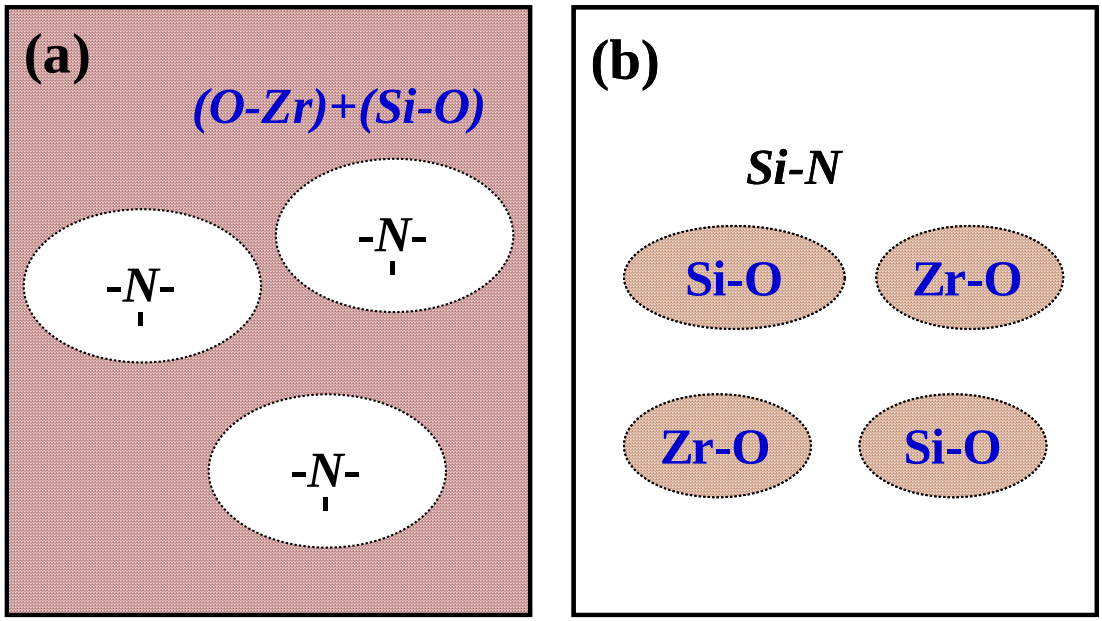

Figure 5.10. Schematic of chemical phase separation in (a) low and (b) high amount of Si_3N_4 phase of Zr-Si oxynitride.

CHAPTER 6. SUMMARY and CONCLUSION

6.1 Zr Silicate and Plasma Nitridation

Nitrogen atoms were incorporated in Zr silicate and its end member using He/N_2 plasma in RPECVD system and the amount of incorporated nitrogen atoms was linearly decrease as the silicate composition going from SiO_2 to ZrO_2, but local minimum in SiO_2 rich silicate ($x<0.3$) was shown due to the presence of H_2O bonding in SiO_2 rich silicate. And AES spectra suggested that the incorporated nitrogen atoms were substituted for the oxygen atom. Since the oxygen atoms in silicate have a two-fold coordinated network in SiO_2 rich silicate, this incorporated nitrogen atoms made a bonding with Si atoms. So the XPS core level of Si binding energy decreased after plasma nitridation. As the concentration of ZrO_2 increase, the oxygen atoms are three-fold coordinated to one Si atom of silicate and two Zr^{4+} ions. Therefore, incorporated nitrogen atoms made a bonding with both Si atom and Zr atom, eventually showed its local maximum in the middle range of silicate by AES analysis. This is also supported from XPS bonding analysis.

Only Si-N bonding (or Si-O-N) remained after annealing at 800°C in SiO_2 rich silicate. On the other hand, Si-N bonding disappeared after annealing whereas Zr-N bonding remains and became a major bonding in the middle range of silicate. The incorporated nitrogen atom into ZrO_2 became a dative bonding due to activating by plasma, eventually, disappeared after annealing. Overall we obtained the different electrical characteristics depending on the silicate composition. The EOT of all range of

silicates decreased after incorporating nitrogen into silicate surface. And no V_{fb} shift both in SiO_2 rich and in ZrO_2 films but shift to negative direction in the middle of silicate, which is attributed to local maximum of incorporated nitrogen atoms. It is also supported by the leakage current density vs. gate voltage analysis. The leakage current decreased by incorporating nitrogen into SiO_2 silicate, whereas increase in the middle range silicate due to the remaining of ZrN bonding, which is considered a leakage source in gate dielectric. No change of leakage current density was detected in ZrO_2 films. Incorporating nitrogen into silicate decreased the leakage current in SiO_2 rich silicate whereas increased in the middle range of silicate.

6.2 Zr-Si Oxynitride, $(ZrO_2)(Si_3N_4)(SiO_2)$

Zr-Si oxynitride films were deposited by using the N_2/N_2O gas mixture in RPECVD system. The composition of the Zr-Si oxynitride alloy fell its own joint line (or plane), one of its sides overlapped with pseudo binary joint line at Si_3N_4 compound. So the Zr-Si oxynitride films can be considered pseudo-ternary alloys that no Zr-N, Zr-Si, and Si-Si, bond are existed. There are forbidden composition in ZrO_2 rich alloy and SiO_2 rich alloy in ternary alloy diagram that is calibrated with RBS. These forbidden composition are in good agreement with the nitrogen amount incorporated by plasma nitridation of $(ZrO_2)_x(SiO_2)_{1-x}$ alloy. Zr-Si oxynitride film is stable up to 1100°C annealing and no chemical phase separations or crystallization are detected by the analysis of the core level BE of oxygen atom. Nitrogen atoms in Zr-Si oxynitride films show no bonding with Zr atoms (zirconium nitride bonding) and the relative amounts of

nitrogen calculated from XPS area are maintained even after annealing. The EOT increases linearly in SiO_2 rich and ZrO_2 rich silicate by increasing annealing temperature up to 1100°C, those increments almost result from the formation of SiO_2 layer between dielectric and silicon substrate. Whereas the EOT of the middle range of silicate increase remarkably as annealed at 900°C, it is attributed to the phase separation as well as the formation interface. However, Zr-Si oxynitride films show no dramatic EOT increase by annealing and the increment is reduced as increasing Si_3N_4 amount. The leakage current of Zr-Si oxynitride film shows two different activation energies depending on the measure temperature, 0.05eV at low temperature and 0.3eV at high temperature. In addition, Poole-Frenkel emission is the dominant leakage mechanism in Zr-Si oxynitride films.

The effect of nitrogen atoms in the Zr-Si oxynitride alloy on the phase separation was investigated by FTIR and XPS analysis. FTIR analysis is more sensitive in detecting of internal structure change of Zr-Si oxynitride than XPS analysis. Zr silicate alloys with no Si_3N_4 phase were chemically separated into the SiO_2 and ZrO_2 phase as annealed above 900°C. While chemical phase separation in Zr silicate films with Si_3N_4 phase (Zr-Si oxynitride) were suppressed as increasing the amount of Si_3N_4 phase due to the narrow bonding network (higher bonding number per atom) in Si_3N_4 phase.

6.3 Recommendations for Future Work

The main focus of this research is on the deposition reproducible pseudo-ternary alloys and suppression phase separation in those alloys by subsequent annealing. This

investigation found that Zr-Si oxynitride was a reliable candidate for high-k dielectric film and the nitrogen atoms played an important role (inhibitor) in atomic scale immigration. Therefore, the results from this study can be used to further investigate the electrical films properties for MOSFET and MOSCAP device application, such as trap level, band offset with respect to the Si, and the charge carrier mobility.